Skoltech
Skolkovo Institute of Science and Technology

Thesis Changes Log

Name of Candidate: Georgy A. Peshkov

PhD Program: Petroleum Engineering

Title of Thesis: Improving the accuracy of thermal history in basin modelling: the reduction of uncertainties in petroleum system analysis

Supervisor: Dr Dimitry Pissarenko

Co-Advisor: Dr Evgeniy Chekhonin

Dear Reviewers,

I would like to say many thanks to you. I appreciate your time and efforts to provide very positive and in-depth comments on the PhD thesis draft.

I have revised the PhD thesis to address all issues raised by the Reviewers. Below I respond to the Reviewers' comments and questions in detail. The reviewers' comments and questions are in italic. The quoted text is a partial copy of the reviewers' reports. According to the specified and generalised reviewers ' comments, all changes are highlighted in yellow. The revised PhD Thesis doc with the changes in yellow highlights follows after the answers.

Reviewer Prof. Stefan Markus Schmalholz:

Comment 1:
"…In the PhD manuscript, there are only a few typos and in one place the same figure is displayed accidentally more than once. These are minor issues that can be corrected within an hour. I can send to Georgy Peshkov a PDF of his PhD manuscript in which I have highlighted these very minor issues so that he can correct them. …"

Replay 1:
Thank you for your comments and sent PhD manuscript document with the highlighted issues. The text of the dissertation has been proofread, and I hope that all the typos are fixed. The repetition of the figure from pages 30 to 32 has occurred after the automatic thesis file conversion by the Canvas system from docx to pdf. I will upload the final thesis version in the Canvas system already converted in pdf format to avoid similar issues.

Reviewer Prof. Bertrand Maillot:

Comment 1:
"… The major weakness of the manuscript is the poor quality of the English language, and second, the writing style. The style is often exhausting to read, with unnecessarily long phrases that do not go to the point. There are also many grammatical errors and a rather awkward english language, with a few

incomprehensible phrases (this is not the case for the publications). This makes the reading cumbersome and the understanding of the work more difficult. …"

Replay 1:

Thank you for your careful reading of the text of the PhD Thesis. The last version of PhD thesis was attentively worked out. And all reviewers' suggestions on improvements were accounted for. I have significantly improved the writing style of the text and improved the readability of the not clearly expressed things. The long exhausting sentences were broken up into several. In addition, numerous grammatical errors have been fixed. Please, see changes in the revised version of the PhD thesis for details.

Comment 2:

"…The methods and workflows presented at the beginning of each chapter are difficult to grasp and the figures (1, 8, 18) do not help much. See below a few examples that certainly do not form an exhaustive list. …"

Replay 2:

I believe that the significantly improved text now could better help to make sense of the mentioned above figures.

Comment 3:

"…This is only a few examples that illustrate the main weakness of the thesis: writing style and english language.

p. 108 top : incomprehensible phrase : "Since modelled stratigraphy, this approach is a function of a multi-coupled solution, it should be fitted with present-day input. …"

Replay 3:

Thank you for the comment. I have rephrased the thing. In the revised PhD Thesis, it looks like:

In forward modelling, the stratigraphy section results from a forward run. The most advantageous tool in the forward-modelling approach uses the iterative search's inversion procedure for the optimal set of stretching factors, sedimentation rates and PWD values. The iterative search's inversion procedure minimises the chosen goal function to fit the modelled stratigraphy section to the observed (input).

Comment 4:

"… p. 5 top : "Chapter 1 analyses the impact of different methods of entering thermal conductivity and its thermobaric corrections on petroleum systems modelling. Besides, this is determined to be the most reliable method for the geothermic characterisation of the model. ..." The 2nd phrase makes no sense after the first one. …"

Replay 4:

Thank you for the comment. I have rephrased the thing. In the revised PhD Thesis, it looks like:

Chapter 2 analyses the impact of different methods of entering thermal conductivity and thermobaric corrections of the thermal conductivities onto petroleum systems models. This chapter determines the most reliable method of capturing the geothermic characteristics of the model. This one is recommended for use when building the reference 1D thermal model to reduce any uncertainties in 2D and 3D models.

Comment 5:

"…p. 5 first parag. of sec. 1.1.2 : could be shortened by half ! …"

Replay 5:

Thank you for the suggestion. It has been done. Please, see details in the revised PhD Thesis.

Comment 6:

"… p. 25 bottom : "If the basement has the heterogeneity in its geological structure, ...": you mean "if the basement is heterogeneous"? …"

Replay 6:
Thank you for the comment. I have decided to delete this incomplete thing at all. This thing is fully discussed in Section 4.2.

Comment 7:
"… p. 33 : incomprehensible phrase : "The digging of the best solution is raised with pursuing software developers' different goals for creating their BPSM software."…"
Replay 7:
Thank you for the comment. I have rephrased the sentence:
It is necessary to dig for the best solution, as software developers' have different goals when creating their BPSM software. However, they all, in one way or another, strive to make their solutions as perfect as they can be.

Comment 8:
"… p. 79, F. 35 : lines in box are too pale and in fact, invisible. …"
Replay 8:
Thank you for the comment. In fact, the information in the box is not important for the present work. I have decided to fill this box with the grid lines. Please, see the updated figure in the revised PhD Thesis.

Comment 9:
"… p. 80, Sec. 4.3.2 : very awkward english expression : "The bulk rock density calibration interchanges the calibration of porosity because of porosity data lack". …"
Replay 9:
Thank you for the comment. This sentence has been deleted at all.

Comment 10:
"…p. 5, top : "Chapter 1..." you mean Chapter 2 ! …"
"…p. 30-32 : Fig 12 is reproduced three times : remove those in p. 30 and 31. …
… p. 56 : legend of Fig. 25 : "Fig. 5" to be replaced by "Fig. 22"…
p. 101 Sec. 6.2 : Second and third mentioned workflows are unnecessarily inverted with respect to the order of presentation in the manuscript. …"
Replay 10:
Thank you very much, these issues have been fixed.

Reviewer Prof. Sergey Stanchits:

Comment 1:
"… Could you please provide the thermal model calibration of your basin model presented in section 3.3.3 of the thesis for both the present-day temperature and vitrinite reflectance? …"
Replay 1:
Thank you for the valuable remark. I have provided a new figure (Figure 17) with thermal model calibration in Section 3.3.3. You can find the figure in the revised version of the PhD Thesis.

Comment 2:
"… I think it would be interesting to see the calibration results of both your work and the work of earlier researchers one the same graph. My guess is that such a comparison can improve the visibility of your research findings and make your results more meaningful. …"
Replay 2:

Thank you for the recommendation. I have compared my well thermal data calibration with another work data, see Figure 17, Section 3.3.3. In addition, the corresponding discussion has been added in Section 3.3.4. Please, see changes in the revised version of the PhD Thesis.

Comment 3:
"… In section 4.2.2, sub-section Model1 vs. Model 2, Densities of the basement (p.63) the following is written: "We also estimated that variations in the radiogenic heat production may change the corresponding heat flow values by less than 2% due to the difference in the crust thickness." Are you sure that 20km column height of mafic vs granite in "heterogeneous crust" causes only a 2% difference in the heat flow? Could you please explain? …"
Replay 3:
Thank you for the valuable remark. Sorry, I have expressed not clear this thing that misled you to the logical but not a proper conclusion. In fact, I meant another point. I have rephrased several sentences around the above mentioned to deliver the thing more clearly. In the revised PhD Thesis, it looks like:

The granites in the upper crust of Model 1 were less dense than mafic or ultramafic rocks formed during mega-rifting. The difference in the basement density distribution between Model 1 and Model 2 resulted in an insignificant change to the Moho boundary position of up to 450 m. Thus, the weight of the vertical columns of the crust and the lithospheric mantle had a negligible effect on the isostatic compensation (Figure 22). We estimated, using the Model 1 dataset, that heat flow values are changed by less than 2% when the Moho boundary moves up to 450 m in the same 110 km total lithospheric thickness. The 450 m difference in the Moho depth between Model 1 and Model 2 was negligible, since the variations in Moho boundaries defined in Braitenberg and Ebbing (2009) and Cherepanova et al. (2013) were more than 5 km.

Comment 4:
"… In Table 2, you referenced to the results of the thermal properties of the core samples measured in ambient laboratory conditions, mentioning the need to apply experimentally obtained thermobaric corrections. How accurately these corrections can be estimated, and how significant could the effect of the uncertainties of these corrections be to the final thermal basin modelling results? …"
Replay 4:
Thank you for the interesting question. The mentioned experimental tool provides the measurements of rock thermal conductivity at temperature up to 300 °C, pore pressure and two components of lithostatic pressure up to 170 MPa. According to the metrological testing of the experimental tool, the precision of measurements is 3.5%, and the accuracy does not exceed 5% for a 95 % confidence level. Thus, the accuracy of the corrections is low and has neglecting impact on thermal modelling results.

Reviewer Associate Prof. Dmitriy Potapenko:

Comment 1:
"… Page 15, 7th row from the bottom "All other material properties (density, specific heat, radiogenic heat and initial porosity) are taken from the simulator database being equal in all dataset by the method presented in Figure 1." Recommending to rephrase it as following to avoid misinterpretation "All other material propert es (density, specific heat, radigenic heat and initial porosity) were taken from the simulator database and were the same in all computations described in Figure 1". …"
Replay 1:

Thank you for the refinement. The clearance of this sentence has been improved. In the revised PhD Thesis, it looks like:
All other material properties (density, specific heat, radiogenic heat and initial porosity) are taken from the simulator database according to Method 1 presented in Figure 1; these properties are equal in all datasets.

Comment 2:
"… Page 21,6th row from the bottom. "Dashed curves on the right panel are the results of modelling without the thermal event (see text for details) (Chekhonin et al., 2020)". Recommending to provide the description of the thermal event in the text and to make the corresponding reference to it. …"
Replay 2:
Thank you for the vital remark. This crucial thing was missed. I have added a short discussion regarding your recommendation in the revised PhD Thesis:
Additional heating at the end of the Triassic or at the beginning of the Jurassic was also taken into account; according to Galushkin et al. (1996), the hydrothermal activity took place at that time. This thermal event is simulated by intrusion and has a negligible impact on the maturation of organic matter in the Bazhenov and Tyumen Fms.

Comment 3:
"… Page 52. 19th row from the top. "The gravity anomaly (Figure 22, red line) was not fitted since the modelled om = 10.5 mGal was greater than the desired accuracy of o = c". Recommending to explain how the desired accuracy level was defined. …"
Replay 3:
Thank you for the question. The explanation of how the desired accuracy level was obtained is presented in Section 4.2.1, before subsection "Construction of a homogeneous basement: Model 1":
The desired accuracy required to fit the model and the measured results of the Bouguer anomaly (see Section 4.1), σ = 6.5 mGal, was defined as the sum of the counter step (ε_c) and the uncertain-ty value of measurements (ε_t).

Comment 4:
"… Page 53, Figure captions for Figure 22 and Figure 23. Recommending to explain the origin of the used accuracy margins of ±1.5 mGal for the gravity anomaly data, ±7% for temperature, and ±0.05% for vitrinite reflectance. …"
Replay 4:
Thank you for the recommendation. Indeed, the explanation of the used accuracy margins for gravity anomaly data, temperature and vitrinite reflectance is not discussed in the main text of the PhD Thesis. I believe it helps to focus the reader on the main subject. However, a detailed explanation is presented in Appendix A, Section A.3.2. I have provided additional links to Appendix A, Section A.3.2 in the main text, where it was needed.

Comment 5:
"… Page 67, Figure 30. Does this figure provide any additional information compared to figure 29? If yes, it would be good to emphasise it in the text. …"
Replay 5:
Thank you for the question. I agree that the presence of Figure 30 may require additional explanation. Figure 29 e and f provides the basal heat flow histories for Model 1 and Model 2, respectively. Figure 30a provides the difference between these models' basal heat flows histories, while Figure 30b provides the mean value of the basal heat flow difference over time. Hence, Figure 30 helps us estimate the absolute difference in basal heat flow values over time to analyse the HB's blocks' most significant impact on the basal heat flow over time. The value of Figure 30 is additionally emphasised in the revised PhD Thesis.

Reviewer Prof. Alexei Buchachenko:

Comment 1:
"… I have little to comment on the thesis text, except noting some formatting inaccuracies like broken figures and tables. Layout of the Fig. 12 is especially bad preventing one to understand the meaning. …"
Replay 1:
Thank you for the comments. I have improved the visibility of some tables and figures by formatting and redrawing, respectively. In addition, the layout of Figure 12 was fixed. Please, see changes in the revised version of the PhD Thesis.

Reviewer Associate Prof. Dmitriy Koroteev:

Comment 1:
"… The only issue I would like Georgy to address is a more pronounced description of the research outcomes' influence on actual reservoir modeling. I.e., I would like to see an estimate of how the workflows developed by Georgy are influencing the overall production forecasts computed with modern reservoir simulators. …"

Replay 1:
Basin modelling and reservoir production modelling refer to different stages of the oil and gas upstream. Basin modelling results help determine the location of a future production reservoir in the early stages of exploration. In addition, the results of basin modelling help to determine the hydrocarbon reservoir volume, but with significant uncertainties. The greater the distance from a well, the higher the uncertainty is. Only the drilling and seismic data can be robust for the detailed production reservoir models. Basin modelling data is not usually used as input to reservoir models. This is due in part to different scales modelling for basin and reservoir in time and space, with different input data requirements and with different reproducible geological processes.
As for the specific developments of this PhD work, I can say that only the developments of Chapter 2 can be used to improve the accuracy of reservoir production modelling. Namely, a method of integrating the measured thermal properties with corrections for thermobaric conditions can be used. The use of this method could make, first of all, the results of gas reservoir exploitation modelling more accurately. The use of this method allows the model geothermic state of the reservoir to be more robust. The robust geothermic model can increase the accuracy of modelled temperatures and pressures to model the PVT state of the gases.
The three proposed workflows cannot be adapted to reservoir simulations due to the different time scales used in reservoir and basin simulations.
Once again want to thank you for this question, as its discourse expanded my understanding of my PhD thesis work significance. Aside from the application of the PhD Thesis results in oil and gas exploration and production, the results can also be useful for estimating geothermal resources. The developed method and three workflows open up a number of new opportunities to improve the accuracy of resource estimates for geothermal energy. That forms additional relevance for this PhD thesis through the application of these developments in geothermal energy exploration.
Based on the aforementioned, I have added two additional recommendations in Section 6.2. Please, see changes in the revised PhD Thesis.

Skoltech

Skolkovo Institute of Science and Technology

IMPROVING THE ACCURACY OF THERMAL HISTORY IN BASIN MODELLING:

THE REDUCTION OF UNCERTAINTIES IN PETROLEUM SYSTEM ANALYSIS

Doctoral thesis
by

GEORGY A PESHKOV

DOCTORAL PROGRAM IN PETROLEUM ENGINEERING

Supervisor

Dr Dimitry Pissarenko

Co-advisor

Dr Evgeny Chekhonin

Moscow 2021

I hereby declare that the work presented in this thesis was carried out by myself at the Skolkovo Institute of Science and Technology, Moscow, except where due acknowledgement is made, and that it has not been submitted for any other degree.

Georgy Peshkov
Dr Dimitry Pissarenko

Abstract

Spatial and temporal temperature variations in a sedimentary basin play a crucial role in petroleum system modelling. The higher the uncertainties in initial geothermal data and thermal history reconstruction methods, the greater the errors obtained in any analysis of petroleum systems. Modern advances in thermal petrophysical and coupled thermal and structural solutions, which are the most consistent approach to thermal history reconstruction, are usually ignored, as is the basin model fitting using measured gravity data.

This work describes the challenges experienced when setting the thermal conductivity and heat flow density (HFD) in basin models and assesses the impact of using unreliable geothermal data on the quality of basin thermal and petroleum system modelling. It also demonstrates the integration method of measured thermal properties through the optical scanning of core samples into the basin model and considers the advantages to be gained from using a coupled thermal and structural solution. The role of gravity data in the basement reconstruction is considered by taking into account the impact on the basin's thermal regime.

To the above-mentioned challenges, three workflows are suggested that aim to avoid the present-day drawbacks inherent in thermal history reconstructions. The first workflow is devoted to reducing the uncertainty of 2D thermal modelling in the most popular backstripping-based simulators for petroleum system modelling by coupling together thermal and structural solutions. Such an approach makes it possible to more accurately revise hydrocarbon generation estimates. The second workflow has been developed to model the basin's 3D thermal history, improving the accuracy of customary approaches. This modelling is achieved by combining the coupled thermal and structural solutions with the backstripping-based structural solution, making it possible to estimate the basal HFD more consistently. The third workflow accounts for the heterogeneous basement (HB) in the model, using gravity data and maps of the basement. This approach gives the most accurate and reliable representation of the structural and geothermic properties of the basement, reconstructing the basal HFD.

A model's ability to accurately describe a phenomenon depends on how well the model incorporates all the relevant geological aspects. That

is, how robust the model depends on its mathematical form and the numerical values of its input parameters. Using all of these workflows can significantly reduce thermal modelling uncertainties, improve petroleum system modelling and lessen exploration risks.

The applications of these workflows and the integration method of measured thermal properties in the models are demonstrated in case studies on the West Siberian, south-western Barents Sea, South Kara Sea, and Okhotsk Sea basins.

Publications

While this thesis was being written, several scientific papers were published. These are listed below.

1. Chekhonin, E., **Peshkov, G.**, Myasnikov, A., Rüpke, L., Podladchikov, Y., Musikhin, K., Shuvaev, A., Bogdanov, O., Kostenko, O., Maglevannaya, P., 2017. Automated Thermal History Reconstruction of Basin in West Siberia Using 2D Inverse Modeling, in: Geomodel 2017. https://doi.org/10.3997/2214-4609.201702248
2. Chekhonin, E., Popov, Y., **Peshkov, G.**, Spasennykh, M., Popov, E., Romushkevich, R., 2019. On the importance of rock thermal conductivity and heat flow density in basin and petroleum system modelling. Basin Research. https://doi.org/10.1111/bre.12427
3. **Peshkov, G.**, Chekhonin, E., Pissarenko, D., 2019. Thermal History Reconstruction of the Sedimentary Basin by Inverse Modeling on the Example of CDP 1632 of the Okhotsk Sea, in: Far East Hydrocarbons 2019. European Association of Geoscientists & Engineers, pp. 1–4. https://doi.org/10.3997/2214-4609.201951020
4. **Peshkov, G.**, Ibragimov, I., Yarushina, V., Myasnikov, A., 2020. Basin modelling as a predictive tool for potential zones of chimney presence, in: EGU General Assembly Conference Abstracts. p. 18689. https://doi.org/10.5194/egusphere-egu2020-18689
5. **Peshkov G.**, Chekhonin E., Rüpke L., Musikhin K., Bogdanov O., Myasnikov A., 2020. Impact of differing heat flow solutions on hydrocarbon generation predictions: a case study from West Siberian Basin. Marin and Petroleum Geology. https://doi.org/10.1016/j.marpetgeo.2020.104807
6. **Peshkov G.**, Khakimova L., Grishkov E., Wangen M., Yarushina V., 2021. Coupled basin and hydro-mechanical modeling of gas chimney formation: the SW Barents Sea. Energies, MDPI. https://doi.org/10.3390/en14196345

Acknowledgements

First and foremost, I would like to express my sincerest gratitude to my supervisors, professors Dr Dimitry Pissarenko, DSc Yuri Popov, and the late DSc Artem Myasnikov, for sharing their inexhaustible scientific experience, offering unceasing support and unreserved encouragement and providing me with patient guidance throughout my PhD program.

I would also like to express my heartfelt gratitude and offer special recognition to two doctoral committee members, Dr Mikhail Spasennykh and Dr Evgeny Chekhonin, for their valuable discussions, thorough comments and extensive communications.

Next, I wish to acknowledge my colleagues at the Centre for Petroleum Science and Engineering. I have greatly valued the multiple consultations with and support from Dr Sergey Stanchits, Dr Evgeny Popov, Raisa Romushkevich, Egor Savelev, Dr Denis Sabitov, Dr Elena Kozlova, Dr Evgenia Leushina, Dr Aysyly Askarova, Dr Lydmila Khakimova, Anastasia Gabova, Arsenii Vladimirov and Iskander Ibragimov.

I am very grateful to the team at Geomodeling Solutions, who provided the academic licence and support for the necessary software; special mention goes to Dr Lars Rüpke and Dr Daniel Schmid, as well as to Dr Yury Podladchikov from Lausanne University, who founded the company.

My thanks also go to Dr Victoria Yarushina and Dr Magnus Wangen from the Institute for Energy Technology (IFE; Oslo, Norway) for their contributions to my understanding of the physics of focused fluid flow formation in all scales.

I would also like to thank Professor DSc Yuri Galushkin from Moscow State University, Dr Sergey Tikhotskiy from the Schmidt Institute of Physics of the Earth, and an expert from Beicip–Franlab (Moscow), Ekaterina Markina, for the multiple spirited discussions we had on basin modelling challenges.

I am very grateful to the members of the LLC LUKOIL Engineering team for their collaboration with non-standard problems and joint publications; I would like to express my gratitude to Dr Oleg Bogdanov, Dr Konstantin Musikhin, Dr Artem Shuvaev and Olga Kostenko.

I would like to express my appreciation of Rosneft and its joint venture with ExxonMobil for the opportunity to collaborate and to create new

solutions. Special thanks go to Dr Yurii Petrichenko, Yulia Maslennikova, Dmitriy Komissarov, Dr Vladimir Verzhbitskii and Natalia Tkacheva.

My thanks also go to my former teachers from Moscow State University: professors DSc Antonina Stoupakova, DSc Georgy Kalmykov, DSc Anatoly Nikishin and professors of practice Dr Enver Ablya, Dr Sergey Frolov, Dr Elena Soboleva and Dr Elena Poludetkina.

Finally, I wish to express my profound and most sincere thanks to my family and friends for their continued moral support.

Georgy Peshkov

Table of contents

List of symbols and abbreviations

1D – one dimensional
2D – two dimensional
3D – three dimensional
A – radiogenic heat production (μWm^3)
A_0 – heat production of the crust at a surface (μWm^3)
B – scale factor (km)
BC1 – first boundary condition
BC2 – second boundary condition
BFTM – backstripping-based with forward temperature modelling
BPSM – basin and petroleum system modelling
CDP – common depth point
CSTM – coupled structural and thermal modelling
C_ρ – specific heat capacity (J/kg/K)
Fm – formation
GC – gravity calibration
HB – heterogeneous basement
HFD – heat flow density (mW/m^2)
MLC – Moho-level calibration
NL – necking level (km)
P – pressure (Pa)
PWD – Paleo-water depth (m)
Ro% – vitrinite reflectance (%)
SWI – sediment-water interface
T – temperature (°C)
TC – thermal calibration
T_e – elastic thickness (km)
TR – transformation ratio (%)
α – thermal expansion (K^{-1})
ε_B – error in introducing the Bouguer correction (mGal)
ε_F – error in introducing corrections for free-air (mGal)
ε_r – error of accounting for terrain correction (mGal)
ε_{rn} – error of reference network observation of gravity (mGal)
ε_t – total error of the Bouguer anomaly (mGal)
ε_γ – error in calculating the normal gravity field (mGal)

λ – thermal conductivity (W/m/K)
ρ – density (kg/m^3)
φ – porosity
φ_0 – surface porosity

List of figures

List of tables

Introduction

General overview

Basin and petroleum system modelling (BPSM) allows us to reduce the economic risks of hydrocarbon exploration through numerical simulations. Such work uses present-day geological and geophysical basin data to reconstruct the basin structure, thermal fields, pressures, and petroleum system processes of the past. One-dimensional (1D) modelling gives a rough appraisal of generation and expulsion timing; two-dimensional (2D) modelling predicts pressure fields and migration pathways and gives qualitative fluid densities and gas–oil ratio estimations; and three-dimensional (3D) modelling provides a complete representation of the drainage area and delineation of flow lines, as well as showing the kitchen processes, quantitative prospect evaluation and prospect rankings. Petroleum system modelling is primarily controlled by two vital physical variables: temperature and pressure. Temperature (along with time) controls the level of organic matter maturity, while pressure defines the paths for hydrocarbon migration. Thus, the reliability of petroleum systems modelling results depends entirely on how accurately thermal and pressure basin regimes are predicted.

Temperature modelling contains several weak points. Without reliable thermal properties (thermal conductivities and radiogenic heat production), a model can contain a multi-variety of thermal scenarios that satisfy the thermal calibration data. At the same time, simplifying assumptions in numerical basin modelling can result in oversimplification, resulting in an inconsistent solution. Both weaknesses lead to incorrect petroleum system analysis results.

Some modern technological solutions partially address such weak points, but they require methodological reinforcement if they are to connect with each other. One of the essential modern achievements in this field is the advancement in thermal petrophysics – the optical scanning of rocks. This technology allows us to measure the full profile of the samples' thermal conductivity (as well as their thermal diffusivity, volumetric thermal capacities, thermal inhomogeneity, etc.) and, following the implementation of specific processes, to use the measurement results in thermal

modelling. State-of-the-art numerical simulation assumes that a simultaneously resolving lithosphere and basin-scale thermal and structural processes will be forward modelled to an inverse scheme, allowing for the automated update of the model parameters. The proper combination of the best technologies can significantly improve thermal modelling by addressing the current drawbacks, potentially reducing economic risks. When implementing such a combination, it is necessary to create special workflows with suitable methodological guidelines.

Problem statement

To develop a group of workflows that will improve the power of models to predict the thermal evolution of sedimentary rift basins, while reducing any exploration risks.

Goal and objectives

Goal: To develop a group of workflows that will improve the predictive power of BPSM through the precise reconstruction of a thermal history.

Objectives:

1. To analyse commercial simulators' capabilities in terms of their ability to calculate thermal properties and their approach to the reconstruction of a thermal history.
2. To assess the uncertainties impact in thermal properties of the simulators databases on basin modelling results.
3. To evaluate the importance of applying the measured thermal properties to basin models.
4. To evaluate the significance of calibrating models using gravity data when modelling the thermal regime.
5. To develop a group of workflows that assists to reconstruct the thermal history of rift basins using known advanced methods.

Outline of the thesis

Chapter 1 presents an analysis of the current drawbacks and challenges present in current approaches to the thermal modelling of basins. Chapter 2 discusses the significance of the joint use of reliable thermal properties, using measured heat flow to construct a consistent 1D thermal model as a reference and comparing the impact of such an approach to

petroleum system modelling with the current approach. Chapter 3 describes the decoupled thermal and structural modelling challenges and suggests a workflow that can integrate coupled and decoupled solutions, to combine their respective technical advantages. Chapter 4 considers the role of gravity data analysis in basin history reconstruction and suggests a workflow for thermal history reconstruction in basins with a heterogeneous basement (HB) based on gravity data analysis. Chapter 5 describes the workflow for the high-accuracy thermal history reconstruction for 3D basin models, and Chapter 6 summarises all the conclusions and offers this thesis' final recommendations for basin-modelling specialists.

Chapter 1. Literature review

1.1 The current challenges presented by thermal modelling within a basin history reconstruction

Hydrocarbon exploration challenges are becoming more complicated due to the depletion of giant and large oil and gas fields. Such a circumstance makes exploration both more capital intensive and riskier. As a result, basin modelling has become an efficient tool that the industry can use to reduce the risks of regional exploration planning. The purpose of BPSM is to quantify hydrocarbons in the petroleum system and estimate their change in balance over time. Models are obtained by the basin evolution simulation in the lithospheric domain through a structural, thermal, and hydrodynamic historical reconstruction.

Industry demand, the scientific community's activity and new technological advances have combined to actively develop state-of-the-art basin modelling simulators. Thus, approaches to reconstructing a basin's thermal history have experienced a marked evolution over the past decades. Basic basin modelling principles can be found in Appendix A and in well-known fundamental books on the subject (Galushkin, 2016, 2007; Hantschel and Kauerauf, 2009; and Wangen, 2010). However, modern approaches still have drawbacks that create significant uncertainties in thermal modelling and, therefore, in petroleum system modelling.

This thesis discusses the following challenges in the thermal modelling of a basin, suggesting potential solutions: (1) the pitfalls of setting customary geothermal characteristics in the basin model; (2) the underestimated role and benefit of introducing gravity analysis into thermal history reconstruction for basins with HBs; and (3) thermal and structural coupling in 2D and 3D modelling for basin history reconstruction. The first and third problems were highlighted 20 years before by Waples (1998) and still remain valid today. Chapter 1 presents the main problems surrounding thermal regime reconstruction, and solutions to these problems are suggested in Chapters 2–5.

1.1.1 The pitfalls of setting customary geothermal characteristics in the basin model

Midttømme and Roaldset (1999) formulated that 'thermal conductivity is a key factor in basin modelling'. This fact was confirmed in fundamental works by Hantschel and Kauerauf (2009) and Peters et al. (2017), which confirm that the uncertainties influence of the volumetric heat capacity and radioactive heat production of rocks affects the results of basin modelling significantly less than uncertainties in the thermal conductivity values do. Thus, this thesis focuses on the properties of rock's thermal conductivity.

Thermal conductivity

Deposited sediments in the basin history change their textural and structural characteristics with the thermobaric conditions in the environment. Various mixing rules for rocks and fluids, which adjust their properties, are embedded in simulators in an attempt to account for these historical alterations. The customary approach assumes the automatic determination of the rock matrix's thermal conductivity values and pore fluid based on a simulator's lithological description and petrophysical database. In addition, the user can enter properties into the model manually, but doing so requires additional analysis. The mixing rules used in simulators do not consider the components' textural or structural features, only their volumetric proportions. Currently, there is no unique and perfect theoretical model that considers all the natural physicochemical processes occurring in rock.

The most commonly used 'geometric mean' model (Lichteneker, 1926) can lead to inaccuracies when assigning thermal conductivity. Calculated thermal conductivity values can be 10–40% higher than measured, assuming a porosity range of 10–35% (Popov et al., 2012). In addition, the higher the contrast in the accounting components of thermal conductivities, the greater the observed discrepancies in measured vs calculated values of bulk thermal conductivities. Asaad's (1955) correction improves Lichtenecker's formula; however, it is usually ignored in modern simulators. Most simulators' databases contain only narrow ranges of matrix values for thermal conductivity without, as a rule, providing information about the texture and structure of rock and its cement characterisation. Moreover, data about thermal conductivities often fail to provide actual

information. The primary reason for this is that, in previous decades, measurements of sedimentary rocks were carried out inappropriately, encountering the problem of contact resistance, which led to underestimation (in some cases, by up to 50%) (Popov et al., 2014). This means that, today, there are not enough reliable measurements to create comprehensive thermal conductivity libraries for all basins and lithology types. Even the most popular simulators (Baur et al., 2018) provide different thermal conductivities for the same lithologies within their databases. Several thermal conductivity temperature dependencies have been suggested by Funnell et al. (1996), Lee and Deming (1998), Sass et al. (1992), Sekiguchi (1984) and Somerton (1992), among others. Lee and Deming (1998) highlighted how the dependencies (corrections) differ in their accuracy and how systematic errors increases with temperature rise. Sekiguchi's correction model is the most popular one used for sedimentary rock basin modelling (Baur et al., 2018; Hantschel and Kauerauf, 2009); it shows that the correction of thermal conductivities decreases for values at atmospheric conditions higher than the reference of 1.84 W/m/K and increases for values lower than this reference. Such a model does not fit all rocks and minerals, however. For example, the measured thermal conductivity of Bazhenov organic-rich shales (the typical range of which is 0.8–3.0 W/m/K at the atmospheric condition) decreases by about 15% in response to a temperature increase of 25°C to 300°C, which contradicts the Sekiguchi model.

Despite the unresolved problems presented by the vast range of thermal conductivities for the same lithologies and inconsistent temperature corrections, most BPSM specialists use the above-described settings for thermal conductivity values and unreliable default temperature corrections. The use of a thermal model of rock obtained from logging data (Fuchs et al., 2015; Vogt et al., 2010) and measurements on a core is always preferable to the use of thermal models that are based on petrophysical databases, since the former approach demonstrates a significantly lower degree of uncertainty in model calculation results (Correia and Jones, 1996; Fuchs and Balling, 2016).

Present-day heat flow density

Paleo-heat flow is another significant uncertainty in thermal modelling; it also strongly influences the proper assessment of petroleum system parameters (Duran et al., 2013a; Gallagher and Morrow, 1998;

Hantschel and Kauerauf, 2009; Thomsen, 1998). In thermal history reconstruction, common practice is for specialists to calibrate their models on present-day heat flow maps, which often contain significant errors. One source of these errors is the inaccuracy of the measured thermal conductivity values (Chekhonin et al., 2020). A geological history must correspond at once to the main geological events and present-day heat flow values (Matava et al., 2019) and to thermal conductivity values.

According to Popov et al. (2019), it is fundamentally necessary to understand that vertical variation of heat flow must be recorded in instances where radiogenic heat production has little effect compared to paleoclimate impact (tens of percents), where fluid migration within a wellbore produces an averaging of the thermal gradient and where systemic errors of thermal conductivities are found (as mentioned above). Neglecting these factors means that significant local fluctuations and the actual heat flow along the wellbore will not be recorded.

Analyses of previously published heat flow data and a comparison of such data with reliable estimates for the same tectonic units based on results from superdeep and deep scientific wells (Clauser et al., 1997; Emmermann and Lauterjung, 1997; Fuchs and Balling, 2016; Kukkonen et al., 2011; Y. A. Popov et al., 2019) suggest that early published heat flow data often contained systematic errors of 40–130%. This is for two reasons: the low quality of thermal conductivity measurements (Pasquale et al., 2012; Popov et al., 2016), and the drawbacks in the earliest approaches to estimating heat flow density (HFD). For example, in Popov et al. (2014) measurements of the thermal regime are conducted in shallow depths (sub-surface, less than 500–800 m, where the effects of paleoclimate and wellbore fluid transportation significantly affect the heat flow), with data showing non-equilibrium temperature measurements and with the averaging of thermal gradient and thermal conductivity data given along with the studying interval. Due to the more precise methods of rock thermal conductivity and wellbore temperature measurements suggested by Duchkov et al. (2013) and Pasquale et al. (2012), these researchers have estimated HFD values as being higher than those found in previous published reports. Thus, it is necessary to verify the reliability of any heat flow data before proceeding with the thermal calibration.

Chapter 2 analyses the impact of different methods of entering thermal conductivity and thermobaric corrections of the thermal conductivities onto petroleum systems models. This chapter determines the most reliable method of capturing the geothermic characteristics of the model. This one is recommended for use when building the reference 1D thermal model to reduce any uncertainties in 2D and 3D models. The case study in this thesis is carried out on the 1D basin model of the Tyumen SG-6 superdeep well (Chekhonin et al., 2020).

1.1.2 The underestimated role and benefit of gravity analysis in thermal history reconstruction in basins with heterogeneous basements

One common assumption in most academic and commercial basin models is connected to the quality of any investigation into the domain of the bottom of the basin and/or of the crustal basement when the basement properties are assumed to be laterally homogeneous. The reason for this is that the degree of detail in surveys decreases with depth; this is due both to economic constraints and geophysical tools' limited capability, leading to the introduction of an 'economic' or an 'acoustic' basement ("Oilfield Glossary, Schlumberger," 2021) in the model that serves as an artificial boundary in the bottom domain of the sedimentary cover.

Hence, because of a lack of data, basin modellers are often forced to assume (in models) the presence of a laterally homogeneous crystalline basement, instead of including the poorly explored bottom sedimentary part or lithospheric strata, even though general geophysical studies have proved that basement rocks have variable densities and thermal properties. Hence, basin modellers deliberately set incorrect thermophysical properties for the basement, expecting that the effect of this rough assumption on the thermal history will be neutralised by the calibration of a thermal model that uses wellbore data. However, successful calibration does not guarantee that a thermal history reconstruction, especially an inter-well thermal history reconstruction, will be free from errors (Chekhonin et al., 2020).

The heterogeneity of the basement in basin models is poorly covered in the literature (Clark et al., 2014; Fattah et al., 2013; Fjeldskaar et al., 2009; Hansford, 2014; Klitzke et al., 2016, 2015; Scheck-Wenderoth et al., 2007; Scheck-Wenderoth and Maystrenko, 2008). Only a few works have considered basement heterogeneity, which affects the basin's thermal

evolution. Klitzke et al. (2015, 2016), Fjeldskaar et al. (2009), Scheck-Wenderoth et al. (2007) and Scheck-Wenderoth and Maystrenko (2008) have all used seismic imaging to determine the geometry of a basement's heterogeneous blocks, although the time–depth conversion for such depths may involve significant uncertainties. They then used gravity data analysis to determine the density values of rocks, following which the determined density values were further interpreted in terms of rock types, using the corresponding thermal properties in the database. Fattah et al. (2013) varied the crust's thickness and composition in order to calibrate their model on gravity data. However, they did not include any quantification of the impact of basement heterogeneity on heat flow and on the maturity of source rocks. All the above works (Fattah et al., 2013; Fjeldskaar et al., 2009; Klitzke et al., 2015, 2016; Scheck-Wenderoth et al., 2007; Scheck-Wenderoth and Maystrenko, 2008) use the decoupled thermal solution (an analysis of the difference between coupled and decoupled solutions can be found in Clark et al. (2014) and Theissen & Rüpke (2010)). To the best of our knowledge, only Hansford (2014) and Clark et al. (2014) used a coupled structural and thermal solution to determine the presence of magmatic bodies in the basement and these bodies' impact on thermal history. Researchers have used the fixed magmatic bodies' typical density to determine their geometry and location in the basement's fitting gravity anomaly; however, the lateral heterogeneity of the crustal layers has been neglected. None of the above works includes a sensitivity study of the reconstructed thermal properties, despite the strong variability in the thermal properties and densities of basement rocks (Haines, 1982; Robertson, 1988).

Based on the extant literature, we may conclude that:

(1) the basement heterogeneity of density and the geometry of the basement are rarely calibrated on gravity data;

(2) there is usually no consideration of the basements' heterogeneity coupled with the basin's thermal and petroleum system models;

(3) the impact of basement heterogeneity on a basin's thermal history is only scantly covered in the literature.

The critical reasons behind all of these conclusions lie in the sophisticated inversion procedure used to reconstruct basement properties and geometry. The customary inversion procedure used in reconstructions

is time consuming, requiring input from various geophysical subjects and from specialists with expertise in different fields. For example, the procedure assumes the use of seismic refraction and reflection tomography experiments, the inversion of travel times by forward elastic-wave propagation modelling and the integration of these results with onshore geology and multichannel seismic, magnetic and gravity data (Minakov et al., 2012). However, in terms of basin modelling, the procedure has a weak point: the lack of a direct possibility of reconstructing thermal properties, which reconstruction is crucial to thermal history reconstruction. Only further non-unique and highly uncertain interpretations of a rock's density can provide thermal properties (as seen, for example, in Scheck-Wenderoth et al. (2007) and Scheck-Wenderoth and Maystrenko (2008)). Thus, it is evident that even the availability of high-quality seismic data and of potential geophysical fields cannot help to reconstruct the thermal properties of a basement, nor can it increase the reliability of the thermal model. The preferred method for obtaining thermal properties is based on using drilling data. However, such data are not always available, especially for the non-explored or poorly explored basins.

Chapter 4 discusses two different cases for rift basins, where gravity calibration plays minor (Peshkov et al., 2019, Section 4.3) and significant roles (Section 4.2) in a basin's thermal history reconstruction. These conclusions are made by evaluating the impact of basement structures and thermal regimes on basin evolution and petroleum system modelling. The so-called express estimation method is presented in Section 4.1 (relating to the latter case in Section 4.2), explaining the need to consider the HB in terms of thermal history reconstruction and by using full-rank 3D basin models that are based on 2D analysis.

1.1.3 Thermal and structural coupling in basin history reconstruction

Investigations of continental rifts over the past decade have greatly enhanced our understanding of the internal geologic processes that form continental margins and rift basins (Brune et al., 2016, 2014; Franke, 2013; Larsen et al., 2018; Peron-Pinvidic et al., 2013; Ranero and Pérez-Gussinyé, 2010). This thesis is focused on the extensional type of basin, since these make up the vast majority of basins worldwide and are associated with the most significant accumulation of hydrocarbons (Newman

and White, 1997; Ziegler, 1994a, 1994b). Strain partitioning during continental rifting and the structures involved are now better understood; modern rift models can explain the highly complex and diverse structures that have been discovered on Earth.

The rift basin is a subject of research interest for both the academic community and industry. However, the application of new knowledge and technologies by the industry lags several years behind scientific achievements. Also, in industrial projects affected by time constraints, the practised basin modelling methods often assume significant simplification of the geological processes (see Cunha, 2015), which impacts the reliability of the modelling results. At the same time, reconstructed thermal and structural history models need to be reliable and robust, since they are an essential means of assessing petroleum systems. Thus, a good balance between the model reliability and the model simplicity is required.

2D thermal history reconstruction

Basin modellers often use simplified approaches to reconstructing thermal history, either by using a backstripping-based approach (to obtain basal heat flow maps over variations of the classic McKenzie (1978) model) or by fixing the thermal gradient directly to stacks of present-day wellbore temperatures (see details in Peshkov et al., 2021a). However, if the simulation does not simplify the thermal history reconstruction approach, as in most cases, the solution remains inconsistent, since the most popular simulators used in the industry are founded on the backstripping-based approach (Baur et al., 2018). The root of this inconsistency is discussed in Clark et al. (2014), Myasnikov et al. (2015), Theissen and Rüpke (2010), Chekhonin et al. (2017), Peshkov et al. (2021a) and Peshkov et al. (2020).

Clark (2014) compares the procedure in and results of two modelling approaches to 2D basin history reconstruction. These are achieved using two types of software, which take two different approaches: BMT, which uses a backstripping-based approach (Fjeldskaar et al., 2004); and TecMod, which uses a forward-modelling thermo-tectono-stratigraphic approach (Rüpke et al., 2008). Table 1 summarises the main distinguishing features of these two modelling approaches.

According to Clark et al. (2014), these approaches give different depth-dependent thinning methods for robust uncertainty estimation. It is

impossible to give an unambiguous estimation as to which approach gives the most accurate result, since both make significant assumptions. However, forward modelling does not require additional input data on paleowater depth (PWD), plus it considers the stretching of sediments. In addition, the thermal solution used in the forward approach is more physically consistent, since it is solved simultaneously with the structural solution (Galushkin, 2007; Myasnikov et al., 2015; Peshkov et al., 2021a; Theissen and Rüpke, 2010). According to Theissen and Rüpke (2010), the backstripping-based approach may systematically underestimate sedimentation rates and total subsidence. It happens because this method does not account for sediments stretching, in contrast to the forward basin modelling approach.

Table 1. The distinctive features of the forward and backstripping-based approaches to modelling, edited after Clark et al. (2014).

Backstripping-based approach	**Forward modelling approach**
Backstripped layers of sediments are restored to given PWD	Sequential time-forward deposition during subsidence that is driven by lithospheric extension
Time backwards, top down, hybrid of simple and pure share, observationally driven	Time forward, bottom up, pure share, causally driven
PWD fixed as input data, fitting the inversed tectonic subsidence by stretching	Numerical inversion of stretching factors and PWD to fit stratigraphy section
Decoupled thermal solution; isostasy assumed	Temperature and isostasy coupled with subsidence

Chapter 3 demonstrates the difference in thermal modelling results from coupled and decoupled thermal and structural solutions and their impact on petroleum system modelling using the West Siberian Basin (Peshkov et al., 2021a) and south-western Barents Sea Basin (Peshkov et al., 2021b) as examples. It also suggests a workflow that will avoid the common pitfalls resulting from simplifications and assumptions made during the basin's thermal modelling in 2D. The workflow integrates reliable thermal modelling approaches with the conventional petroleum system modelling used with the most popular simulators (Baur et al., 2018). The workflow's effectiveness is demonstrated in the West Siberian Basin example (Peshkov et al., 2021a).

3D thermal history reconstruction

Reliable thermal history reconstruction becomes more critical to 3D petroleum systems modelling, since the modeller's task is more challenging in 3D than it is in 2D. For example, the tasks not only include determining the timing and quality assessment of petroleum systems; modellers are also required to predict the hydrocarbon's drainage, flows, accumulation areas and masses. Hence, the spatial material balance of oil and gas–generated masses becomes more striking, taking the leading role in predicting the prospecting deposits. Thus, petroleum system analysis requires a very reliable thermal solution in 3D. At this point, it is possible to face the difficulties of applying both the 3D backstripping-based and 2D coupled structural and thermal modelling (CSTM)–based approaches to reconstructing the 3D thermal history of the basin.

Decoupled 3D thermal and structural backstripping-based solutions can be run in two ways (see details in Appendix A, Section A.2.1). The first method is used when the thermal problem implies the need for a 3D solution. Here, the lower boundary condition must be fed only on the basin bottom, as a basal heat flow. The second method is used when the thermal problem implies a multi-1D solution. Here, the lower boundary condition must be set on the lithosphere/asthenosphere boundary. Even though such an approach is able to consider the blanketing effect, the drawbacks of the decoupled solution still harm the quality of the reconstructed thermal history. These drawbacks primarily include underestimating sedimentation rates, ignoring the extension of sediments and experiencing lateral heat transition effects. However, a few months ago, a software developer (Beicip–Franlab) produced a tool for the 3D basin modelling of a backstripping-based approach, offering a 3D thermal solution in the lithosphere scale. This solution excludes the lateral effects of solving the thermal problem from the drawbacks mentioned above.

Although the CSTM-based approach is devoid of all the drawbacks found in the decoupled solution, the basin reconstruction is still only performed for the 2D case. Here a question is raised as to how to reliably reconstruct the thermal history of the basin in 3D in integration with 3D petroleum system analysis, using the advantages of the 2D coupled solution.

Chapter 5 presents an extension of the workflow developed in Chapter 3 for the thermal history reconstruction in 3D. The workflow combines the 3D backstripping-based structural solution with a coupled 2D thermo-tectono-stratigraphic approach, bringing their advantages together through geostatistical data mining. The workflow is then successfully applied to the thermal history reconstruction of the South Kara Sea Basin (see Chapter 5).

Chapter 2. Evaluating the impact of reducing the uncertainty of the geothermal characteristic on petroleum systems modelling

Common practice in present-day BPSM geothermal characterisation assumes the use of thermal properties from a database, a lithological description and an a priori specified HFD as a present-day boundary condition (see details in Appendix A, Section A.3.1).

However, specialists frequently overlook the need for consistency between rocks' thermal properties and the present-day measured HFD. The latest advances in thermal petrophysics can solve this problem for three reasons. First, superdeep continental scientific drilling results have given us a new understanding of the thermal regime at substantial depths (Emmermann and Lauterjung, 1997; Popov et al., 2012). Second, it is well understood that the most advanced modelling techniques used to analyse thermal histories and source rocks' maturation may fail when non-reliable predicted thermal conductivity is applied to basin characterisation (Blackwell and Steele, 1989). Third, the rapid development of the new technologies used to measure the thermal properties of rocks makes it possible to conduct a vast number of measurements and to register the spatial variations of any thermal properties, taking into account a formation's in-situ thermal and pressure conditions.

This chapter discusses one common and two advanced methods of the present-day model's geothermic characterisation and their application, before estimating the impact on petroleum system modelling had by different geothermic characterisation methods.

2.1 A methodology for present-day geothermal characterisation

The most common method of geothermal characterisation uses the geothermic properties setting procedure presented in Al-Hajeri et al. (2009) and Hantschel and Kauerauf (2009). Its application requires a lithological description of the defined formation according to the percentage of each rock/mineral component present and to the present-day HFD from depth. The lithological description allows us to define all the material properties required by the modelling using a petrophysical database and mixing rules (Hantschel and Kauerauf, 2009). It is recommended that, when calculating the temperature and thermobaric corrections on thermal conductivities, the Sekiguchi (1984) or Norden et al. (2020) dependencies, respectively, be used.

The detailed scheme used by the common method – Method 1 – is shown in Figure 1, and the corresponding detailed description is provided in Vladimirov (2020). First, the pressure and porosity data should be calibrated by tuning the initial porosity (φ_0) and depth-dependent factor (B) according to Athy's law (Athy, 1930) or by using alternative parameters for analogue laws to constrain the uncertainties coming from porosity-dependant properties. The calibration of the present-day thermal regime should be performed, accounting for the equilibrium temperatures, the vitrinite reflectance and the values of heat flow densities corresponding to the thermal conductivities used in the model. The thermal properties of a rock matrix can be tuned if the calculated thermal gradient is not in accordance with the expected one.

Method 2 improves upon the first method. Here, we are assuming that the second method uses the same input data to define all the material properties of a formation. The thermal conductivity values at atmospheric conditions defined by the database are changed according to measured thermal conductivity data. When using this method, it is strongly recommended that the most advanced thermal profiling equipment be used to determine the thermal conductivities at atmospheric conditions (Popov et al., 2016, Section 1.1.1). Since this method takes into account the effective thermal conductivity measured for core/rock samples that are saturated by fluid, it is necessary to recalculate for rock-matrix values, as shown in Popov et al. (2017). The calibration procedure and thermal conductivity correction should be performed as they are in the first method.

Method 3 improves upon the second method by adding the thermal conductivities of rocks measured in thermobaric (in-situ) conditions (Popov et al., 2013). A generalised workflow for a present-day thermal characterisation is proposed in Vladimirov's (2020) Master's thesis. The author of the present work also took part in the development of the workflow, the results of which are presented in Chekhonin et al. (2020). Both the second and third methods were made possible thanks to techniques developed by Skoltech and continuous advancements of the techniques used for measuring rock thermal properties and defining heat flow (Popov et al., 2016, 2018, 2019). It is recommended that the third method be applied to the construction of a 1D reference thermal model, before any more complicated 2D and 3D models are created.

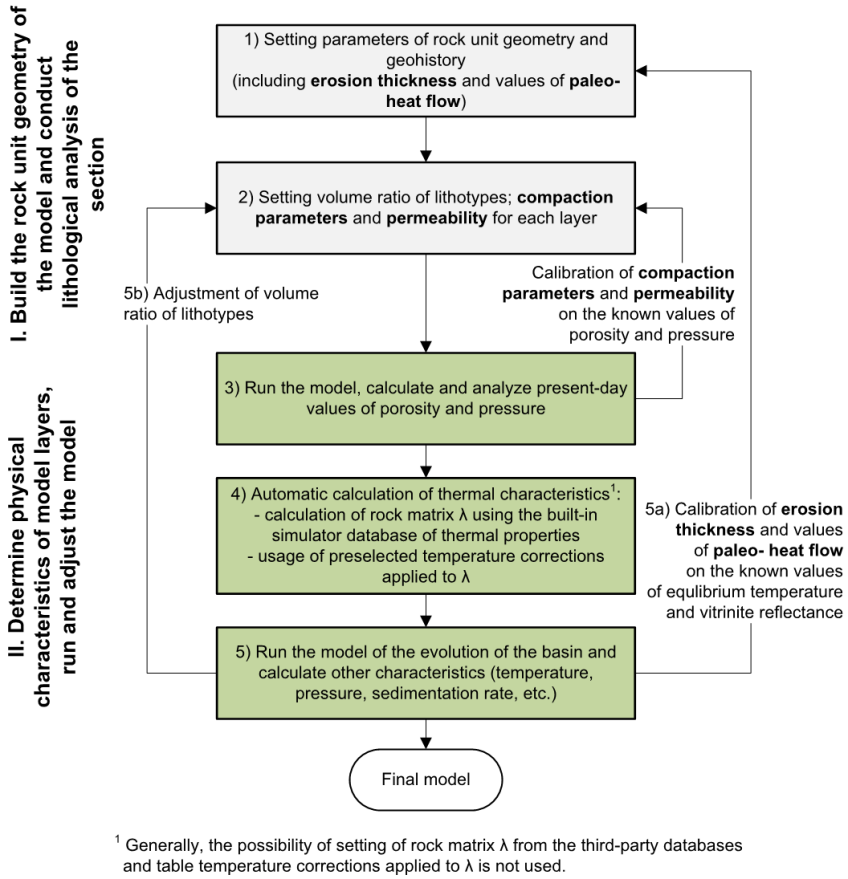

Figure 1. A common method (Method 1) used to set parameters (Vladimirov, 2020).

2.2 A case study of the Tyumen SG-6 superdeep well

The modelling procedure and its results, discussions and conclusions are described in detail in Chekhonin et al. (2020).

The modelled object is related to the Tyumen SG-6 superdeep well in the Urengoy rift graben in the West Siberian Basin (Figure 2). The stratigraphy and tectonic events observed in the Tyumen SG-6 well area used in the basin model's construction are shown in Figure 3. A multi-scenario 1D model, which benefits from a large quantity of reliable input and calibration data, was built to show the consequences of uncertainty in present-day geothermal characteristics, which are related to the pitfalls mentioned in Section 1.1.1 on petroleum system modelling.

The models were performed to simulate the burial history of sediments, temperature and source-rock maturation. A non-steady-state thermal modelling was applied.

2.2.1 Initial data

Simulated present-day effective thermal conductivity profiles, along the wellbore for geothermal datasets (1.x, 2.x, 3.x, 4.x) are shown in Figure 4.

Eight different geothermal datasets were prepared for the case study. This was achieved by combining four different methods of deriving thermal conductivity and two different approaches to defining time-dependant basal HFD. For those datasets that have different thermal conductivity information entered, the names 1.x, 2.x, 3.x and 4.x were used, where x is the method used to enter basal HFD into the model. For datasets with different boundary conditions (i.e., different HFDs) the names x.1, x.2 are used, where x is the method used to enter thermal conductivity data into the model. In total, 8 datasets were performed. All other material properties (density, specific heat, radiogenic heat and initial porosity) are taken from the simulator database according to Method 1 presented in Figure 1; these properties are equal in all datasets. The kerogen's geochemical characteristics for the Bazhenov (a) and Tyumen (b) Formations (Fms) used for petroleum systems modelling are summarised from various papers. The description of these datasets is provided in the work of Chekhonin et al. (2020).

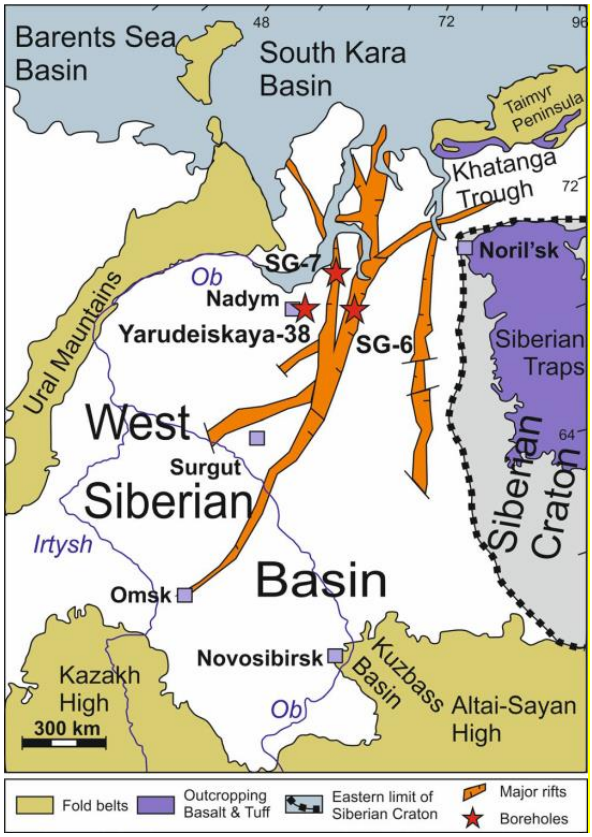

Figure 2. Map of the West Siberian Basin and adjacent regions, showing major geological features (modified from Saunders et al., 2005). The map shows the locations of superdeep Tyumen SG-6 and En-Yakhinskaya SG-7 wells and the Yarudeiskaya-38 deep well (Chekhonin et al., 2020).

Thermal conductivities for Datasets 1.1 and 1.2 are obtained using the Method 1 described in Section 2.1, using the lithological column shown in Figure 3. Thermal conductivities for Datasets 2.1 and 2.2 are defined as matrix conductivities in Datasets 1.1 and 1.2 increased by 30 %. Thermal conductivities for Datasets 3.1 and 3.2 are obtained using the Method 2 described in Section 2.1. Thermal conductivities for Datasets 4.1 and 4.2 are prepared using the measurements as described in Section 2.1 (Method 2 and Method 3). These measurements are performed using the core samples from Tyumen SG-6 well collected from the depth interval 3,800–7,502 m. Data from measurements in adjacent wells (Figure 2) are used to reconstruct the thermal conductivity profile in the 0–3800 m interval.

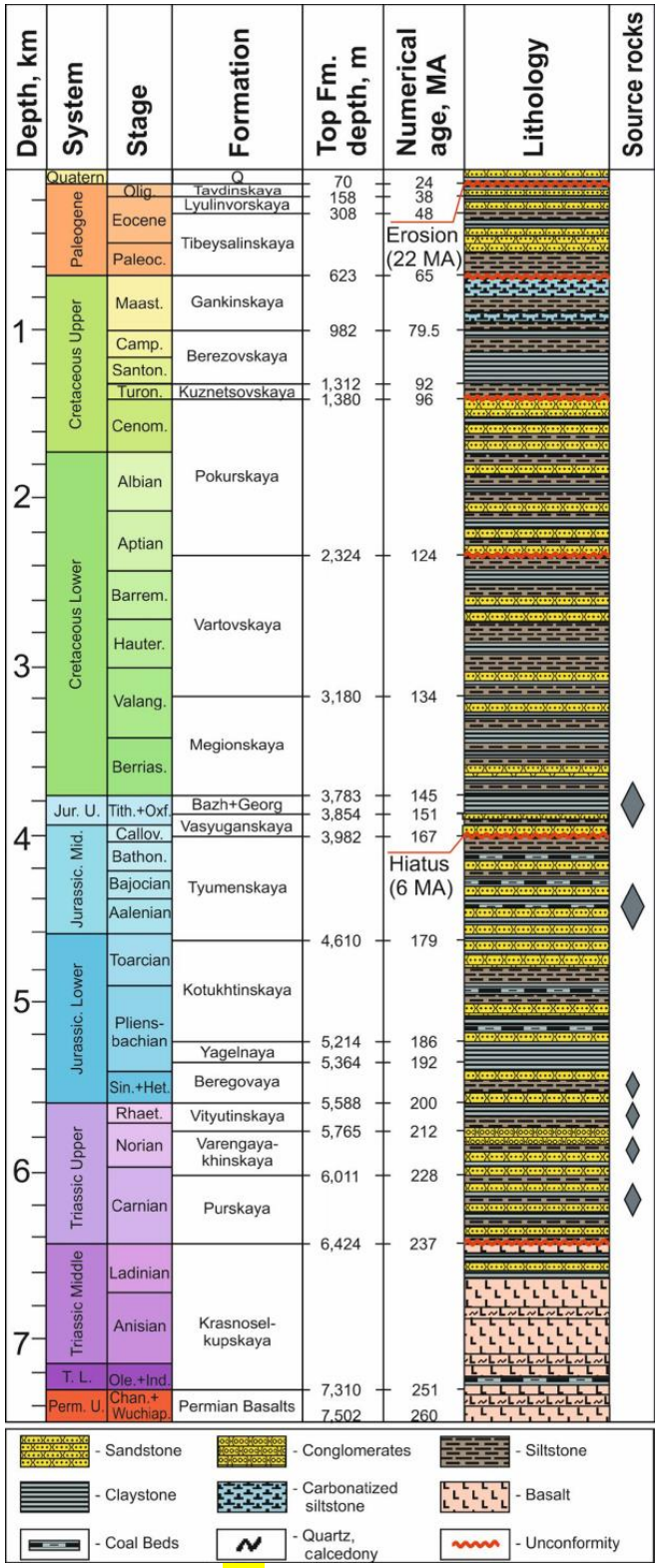

Figure 3. Stratigraphic chart for the Tyumen SG-6 well area (Chekhonin et al., 2020).

The thermal conductivity corrections by temperature (Table 2) described by Sekiguchi (1984) are applied to the entire depth range for Datasets 1.1–3.1 and 1.2–3.2 and to the 0–3,800 m depth interval for Datasets 4.1 and 4.2. In the 3,800–7,502 m interval, the thermal conductivity corrections by temperature are obtained experimentally, using special equipment, by Popov et al. (2014) (see details on the Method 3 in Section 2.1).

Simulated present-day effective thermal conductivity profiles, along the wellbore for geothermal datasets (1.x, 2.x, 3.x, 4.x) are shown in Figure 4.

Table 2. Four different methods used to enter thermal conductivity information into the model (Chekhonin et al., 2020).

Geothermal dataset[a]	Depth interval (m)	Rock matrix thermal conductivity (at atmospheric conditions)	Temperature dependence of thermal conductivity
1.x	0–7502	Data according to formation lithology (simulator database)	Sekiguchi (1984)
2.x	0–7502	Data according to formation lithology (simulator database), manually increased by 30%	Sekiguchi (1984)
3.x	0–3800	Data according to in-house database[b]	Sekiguchi (1984)
	3800–7502	Results of measurements on core[c]	Sekiguchi (1984)
4.x	0–3800	Data according to in-house database[b]	Sekiguchi (1984)
	3800–7502	Results of measurements on core[c]	Table dependence[b, c]

[a] Geothermal datasets x.1 and x.2 are the same in terms of thermal conductivities, but their HFDs differ.

[b] A database, continuously updated since 1988, containing the results of experimental studies (using optical scanning) of the thermal properties of more than 35,000 samples of sedimentary rocks from different regions of Russia and the world. The database also includes the pressure and temperature dependencies of thermal properties, which were experimentally obtained using special equipment (Popov et al., 2014).

[c] Data obtained from the instrumental evaluation of core samples from SG-6 well (Popov et al., 1996).

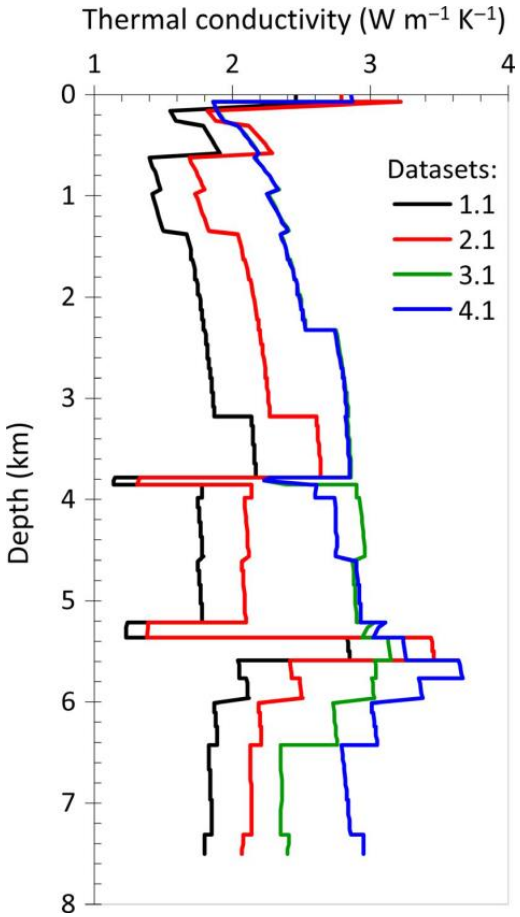

Figure 4. Present-day variations of effective (bulk) thermal conductivity with depth for the datasets used (Chekhonin et al., 2020).

PWDs are taken from Babushkin et al. (1995), Galushkin et al. (1999) and Kontorovich et al. (2013). The top (Figure 5a) and bottom (Figure 5b) thermal boundary conditions are used for the non-steady-state thermal modelling. The paleotemperatures on the sediment surface are taken from Galushkin (1997) and Galushkin et al. (1999).

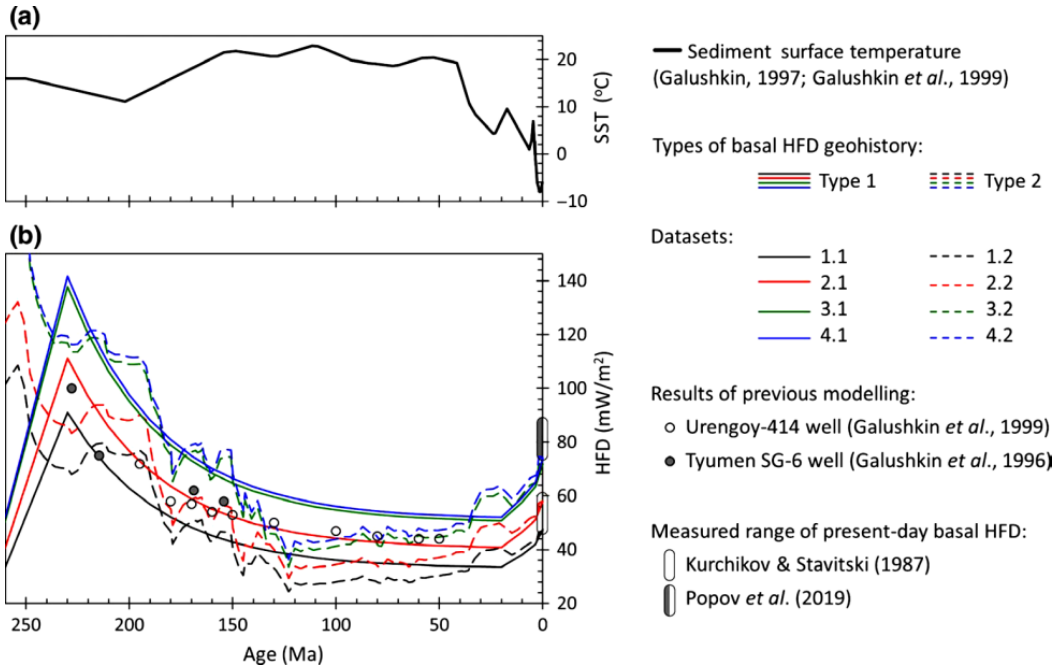

Figure 5. Upper (a) and lower (b) boundary conditions for thermal history modelling. Geothermal datasets are prepared by combining two types of basal HFD history and four different methods used to enter thermal conductivity values (Chekhonin et al., 2020).

Two considered typos of basal HFD evolution were defined by the bottom boundary conditions. Type 1 is based on a McKenzie (1978) model; the curve is derived using reference data from Galushkin et al. (1999, 1996). Corresponding geothermal datasets are indicated as x.1, where x is the method used to enter thermal conductivity data into the model.

The Type 2 curve is derived using a thermo-tectono-stratigraphic approach (see details in Appendix A, Section A.2.2). Here, the upper boundary condition mentioned above and a constant temperature of 1300°C at the lithosphere base (Fischer et al., 2010) are used for the non-steady-state thermal modelling. The HFD obtained reflects the blanketing effect (Theissen and Rüpke, 2010), the impact of a paleoclimate, and the Neogen erosion. Corresponding geothermal datasets are indicated as x.2, where x is the method used to enter thermal conductivity data into the model.

Experimental geothermal studies at Tyumen SG-6 and at nearby wells (Figure 2) give us an estimate of the present-day basal HFD of 75–

90 mW/m^2 (Popov et al., 2019), which is consistent with thermal conductivity datasets based on core measurements (Datasets 3.x and 4.x). The new heat flow estimate is more than 60% higher than the previous 46–61 mW/m^2 (Kurchikov and Stavitsky, 1987), which corresponds to the thermal conductivity datasets 1.x and 2.x.

2.2.2 Calibration procedure

The model for each geothermal dataset is calibrated using porosity (Fonkin, 1996; Popov et al., 1996), pressure and temperature (Batalin and Vafina, 2017; Karaseva et al., 1996) and vitrinite reflectance data (Bogoyavlenskiy and Polyakova, 2012; Dolzhenko et al., 2017; Fomin et al., 2001; Galushkin et al., 1996). The results of the modelling using different datasets are then compared with each other and analysed.

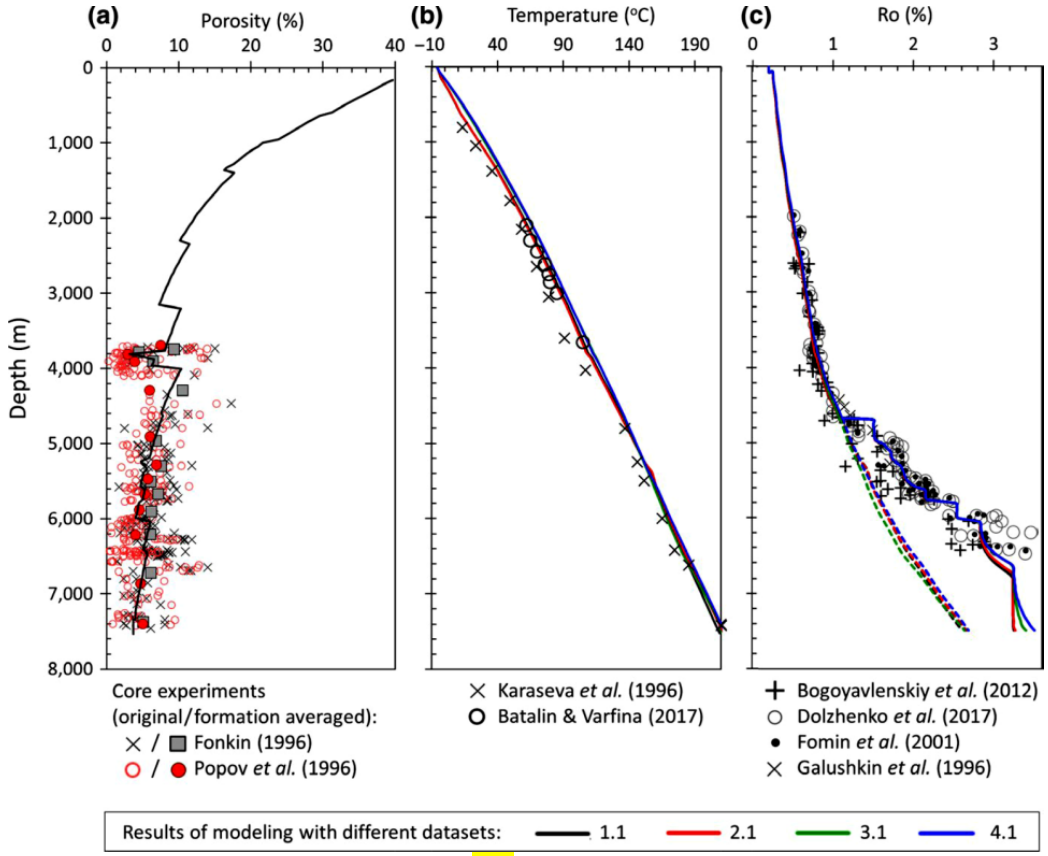

Figure 6. Results of calibrations for porosity (a), temperature (b) and vitrinite reflectance (c) for Datasets 1.1–4.1. The dashed curves in the right panel are the results of modelling without the thermal event (see text for details) (Chekhonin et al., 2020).

Additional heating at the end of the Triassic or at the beginning of the Jurassic was also taken into account; according to Galushkin et al. (1996), the hydrothermal activity took place at that time. This thermal event is simulated by intrusion and has a negligible impact on the maturation of organic matter in the Bazhenov and Tyumen Fms.

2.2.3 Results and discussion

The results of modelling for source rocks are shown in Figure 7.

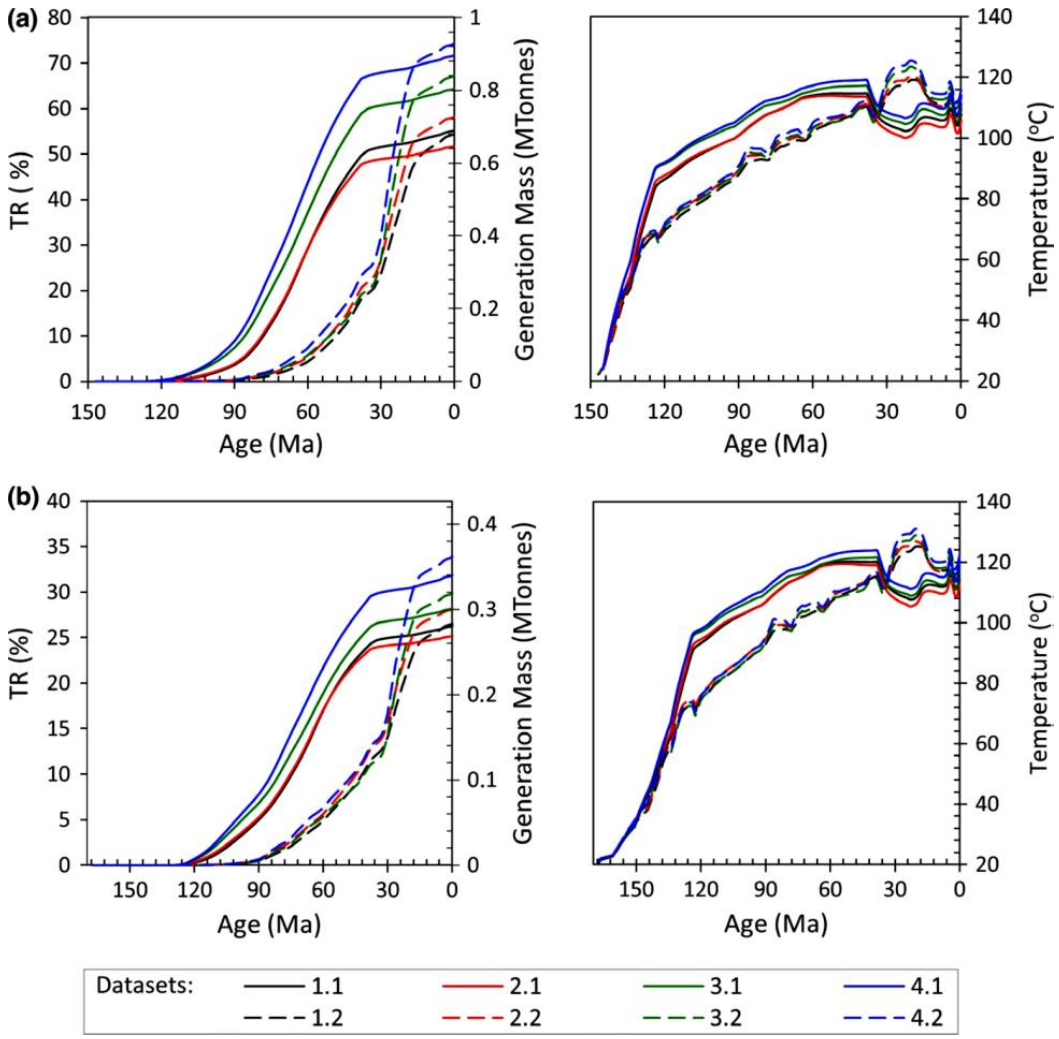

Figure 7. The results of modelling with different geothermal datasets (transformation ratio (TR), generation mass of hydrocarbons and temperature) in the bottom part of the Bazhenov (a) and Tyumen (b) Fms (Chekhonin et al., 2020).

A comparison of Datasets 1.1 and 2.1 shows that the systematic increase in the matrix thermal conductivity by 30% (Figure 4) corresponds

to the almost systematic increase in basal heat flow (Figure 5b). As a result, the maturity of the source rocks remains almost the same. A comparison of Datasets 1.1 and 3.1 demonstrates that the use of experimental thermal conductivity data with the Sekiguchi temperature correction leads to an increase in the transformation ratio (TR) of 10%, which is equivalent to a 0.1 Mtonne increase in the mass of hydrocarbon generation. A comparison of Datasets 1.1 and 4.1 shows that the used experimentally measured thermal conductivity data in atmospheric conditions with thermobaric corrections significantly changes the maturation pattern of source rocks: TR increases by 18%, and the generation mass increases by 0.2 Mtonnes. A significant discrepancy in the critical moment of the source rocks' maturity (approximately 25–50 Ma) is also found. A comparison of Datasets 3.1 and 4.1 shows that the Sekiguchi (1984) temperature correction for the thermal conductivity instead of the experimentally determined thermobaric correction in the lower depth interval (3,800–7,500 m) results in TR underestimation by 10%, which is equivalent to a loss of 0.1 Mtonnes of hydrocarbons.

Accounting for the blanketing effect on basal HFD evolution (Dataset x.1 vs Dataset x.2) changes the source-rock maturation picture. The critical moment is displaced by approximately 40 Ma, which highlights the importance of ensuring the consistency between the basal heat flow history and the thermal conductivity values used to decrease uncertainty in the modelling results.

Similar effects are also observed in the Tyumen Fm (Figure 7b). The minor difference in hydrocarbon generation trend in the Tyumen Fm compared to Bazhenov is explained by different kinetics, initial total organic carbon and hydrogen index values for source-rock characterisation.

The results indicate that model calibration using present-day temperature and vitrinite reflectance values does not mean that the reconstructed thermal history is correct. However, the use of reliable data for the thermal conductivity of rock and present-day basal heat flow values significantly reduces any uncertainties in the simulated time dependence of the hydrocarbons' generated volume.

2.2.4 Conclusions

There are many pitfalls in the customary approach to the present-day geothermal characterisation of a basin: the neglect of the coupled application of thermal conductivity and the measured basal heat flow (as a boundary condition); significant uncertainties in the thermal conductivity data for rocks and minerals from petrophysical databases; the use of the Sekiguchi correction; the application of the widely used geometric-mean mixing rule to determine bulk thermal conductivity; and the insufficient reliability of the old HFD maps.

The performed analyses demonstrate that uncertainties relating to rock thermal conductivity and HFD are often underestimated and significantly impact both the reconstructed thermal regime and the simulated source-rock results. This conclusion has been proven by a case study of the superdeep Tyumen SG-6 well, using a unique and reliable dataset of input and calibration data. The results indicate that a lack of reliable experimental geothermal data produces many different combinations of thermal conductivities and HFD, which may result in different scenarios for the maturation of source rocks even after model calibration has been performed for porosity, temperatures and vitrinite reflectance.

Usually, the amount of reliable input and calibration data is much more limited than in the case study presented here, and as this study has shown, the absence of data may increase the size of errors in the modelling results. The quality of BPSM can be significantly improved upon by making the best use of advances in thermal petrophysics (Popov et al., 2012, 2016). It is necessary to develop new or modify existing mixing rules and update thermal conductivity databases and thermobaric corrections used for defining thermal conductivities. It is also essential to take proper account of present-day HFD measurements, which serve as a vital reference for the reliable reconstruction of a thermal history.

Carrying out such fundamental investigative research on a large number of wells for any basin is costly. Nevertheless, as has been illustrated in this chapter, creating at least one reference 1D thermal model is strongly recommended, as such a model can serve as a basis for building reliable 2D and 3D thermal models. Solving problems in this way and following the above recommendations can significantly reduce uncertainties

in any quantitative estimations of the generation, migration and accumulation of hydrocarbons.

Chapter 3. Thermal and structural coupling in a 2D basin history reconstruction

3.1 The methodology of basal heat flow reconstruction and its integration with petroleum system modelling

Appendix A (see Section A.2) discusses the two principal basin thermal history reconstruction approaches: backstripping-based with forward temperature modelling (BFTM) and coupled structural and thermal modelling (CSTM). Section 1.1.3 of this thesis discussed the key advantages and disadvantages of approaches to thermal history reconstruction for BPSM. Since the BFTM-based simulators are usually the most popular, they possess more advanced petroleum system modelling modules. The analysis in Section 1.1.3 shows that the thermo-tectono-stratigraphic (CSTM) approach (Rüpke et al., 2008) possesses the most consistent thermal history reconstruction solution; however, it cannot be used for proper evaluation of the petroleum systems. This situation raises a reasonable question: how do we combine the advantages of thermal modelling using the CSTM-based approach with the advantages of petroleum system modelling using BFTM-based simulators into a single BPSM workflow?

This section develops a suggested workflow (Figure 8) for a 2D BPSM. Following the workflow in Figure 8, the first step (Step 1) is to build a 2D model in BFTM-based software according to the most commonly used workflow described in Al-Hajeri et al. (2009), Hantschel and Kauerauf (2009) and Peters et al. (2017). Combining the consistent thermal and structural solution with the advanced approach seen in present-day geothermal regime characterisation (see Chapter 2) allows us to improve the thermal regime's reliability.

When the model is built, and porosity (φ) and pressure (P) regimes are calibrated against measured data, the model exporting (consisting of material properties, lithostratigraphic information, sediment–water interface (SWI) temperature and lithospheric parameters) is carried out in the CSTM-based simulator (Step 2). The sensitivity studies of the thermal properties can be useful when fitting the modelled temperatures and vitrinite reflectance against their measured data.

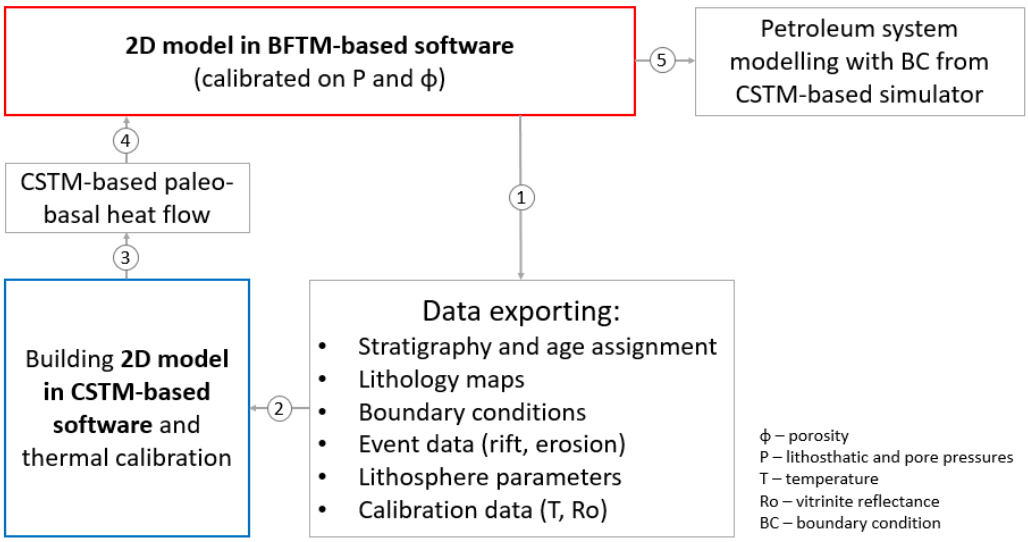

Figure 8. The developed workflow, combining the thermal model from the CSTM-based approach with the petroleum system modelling abilities of the BFTM-based software. The numbers in circles show the sequence of events.

In Step 3, the reliable temporal basal heat flow variations are obtained and can be used as a lower boundary condition in a BFTM-based simulator (Step 4). The boundary condition accounts for the impact of basin structural evolution coupled with thermal modelling and can be used to conduct a consistent petroleum system assessment in Step 5.

3.2 A case study from the West Siberian Basin

The modelling procedure and its results, discussions, and conclusions are presented in detail in Chekhonin et al. (2017) and Peshkov et al. (2021a).

In this section, which focuses on the West Siberian Basin (Figure 9 and Figure 10), we propose to demonstrate the workflow's effectiveness (Figure 8), thereby improving the accuracy of the thermal evolution modelling. We will realise the workflow, step by step, and discuss the results.

The model presented here has two different boundary conditions at the basin bottom, which are derived through the use of two different approaches. The first boundary condition (BC1) is obtained using the CSTM-based approach, while the second boundary condition (BC2) is obtained using the BFTM-based approach (for more detail, see Appendix A, Section A.2.1). The petroleum system modelling is carried out in a simulator that is based on the BFTM-based approach. There is a dearth of measured thermal properties in this area however; hence, the properties used here are taken from the simulator's petrophysical database. This methodology allows performing relative comparison (not the absolute comparison) of both modelling approaches used for defining the heat flow without using reliable input data. Practising this comparison methodology requires using similar input data for all evaluated models.

The study was performed by following the workflow given in Figure 11. The first step is to build a 2D model in the BFTM-based software, as described in Al-Hajeri et al. (2009), Hantschel and Kauerauf (2009) and Peters et al. (2017). The prescribed standard approach to entering input data is used (see Appendix A, Section A.3.1). The dataset is described in detail in Peshkov et al. (2021a). Here, the model is calibrated, as required, for porosity, pressure and the Moho boundary. The model is computed under the assumption of the Airy isostasy. The search stretching factors through the inversion by fitting the tectonic and theoretical subsidence curves to each other is done in order to simulate the basement's thermal evolution with these factors. The outcome of the modelled basement thermal evolution is the basal HFD, denoted as BC2.

In Step 2, all the required data are exported in order to build a similar model in the CSTM-based simulator. The optimal set of stretching fac-

tors, sedimentation rates and paleowater depth values, are inverted automatically by the goal function minimization of the misfit between observed and modelled stratigraphic data. Since, after the inversions, the stretching factors in the BFTM- and CSTM-based approaches are obtained using different values, the thermal calibration (which is achieved by varying the value of radiogenic heat production) is undertaken in order to fit the thermal calibration (for more detail, see Section 1.1.3), as was done for the BFTM-based solution.

In Step 3, basal heat flow in time is obtained in the CSTM-based solution, and in Step 4, it is extracted and integrated into the BFTM-based simulator as a boundary condition at the basin bottom. Thus, two modelling scenarios comprising the same model and two different lower boundary conditions (BC1 and BC2) are defined. In Step 5, the model containing BC1 and BC2 is computed, and the results (the predicted times and volumes of generated hydrocarbons) are compared within one modelling system.

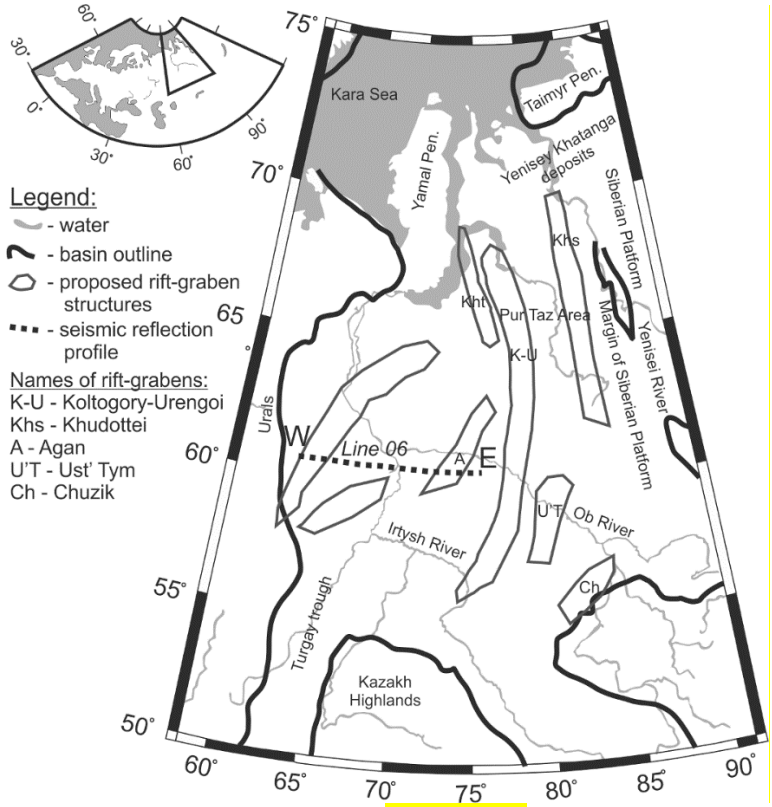

Figure 9. The position of the studied Profile #6 of the West Siberian Basin (Peshkov et al., 2021a).

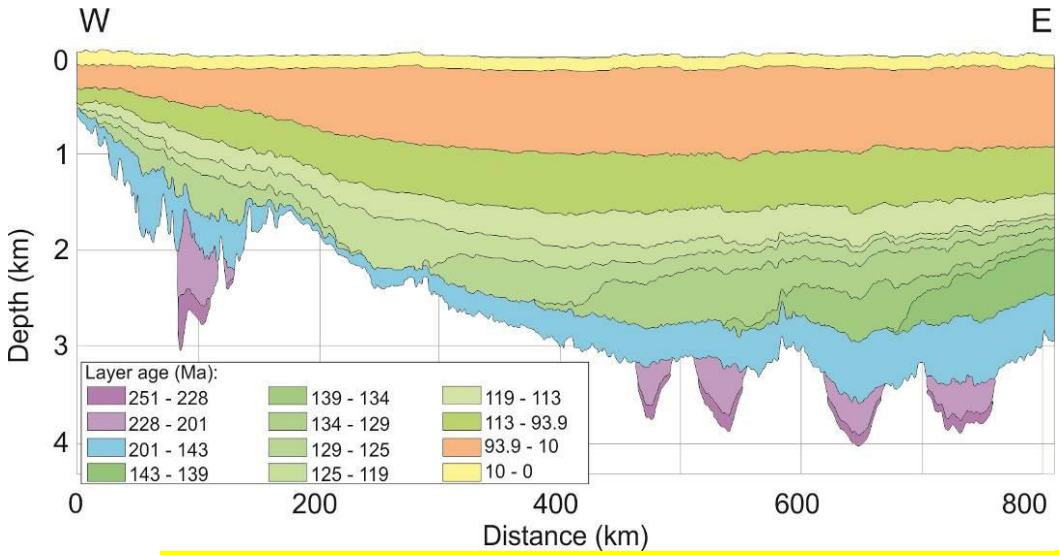

Figure 10. The input stratigraphy of the transect along the sub-meridional regional Profile #6, which crosses the West Siberia basin from West (W) to East (E) (Peshkov et al., 2021a).

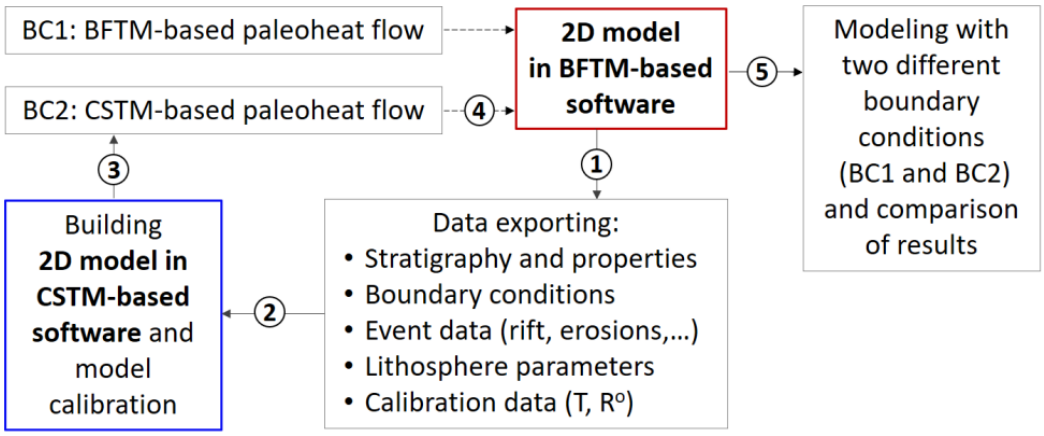

Figure 11. The suggested workflow, which is used to compare results in petroleum system modelling for both CSTM- and BFTM-based approaches. The numbers in circles show the sequence of events (Peshkov et al., 2021a).

3.2.1 Results and discussion

The BFTM-based approach systematically underestimates total subsidence during the thermal subsidence period (~60 Ma post the riftogenesis period) according to Theissen and Rüpke's (2010) observations. However, the discrepancy does not exceed several hundreds of meters.

Both basal heat flows – the boundary conditions – are presented in Figure 12.

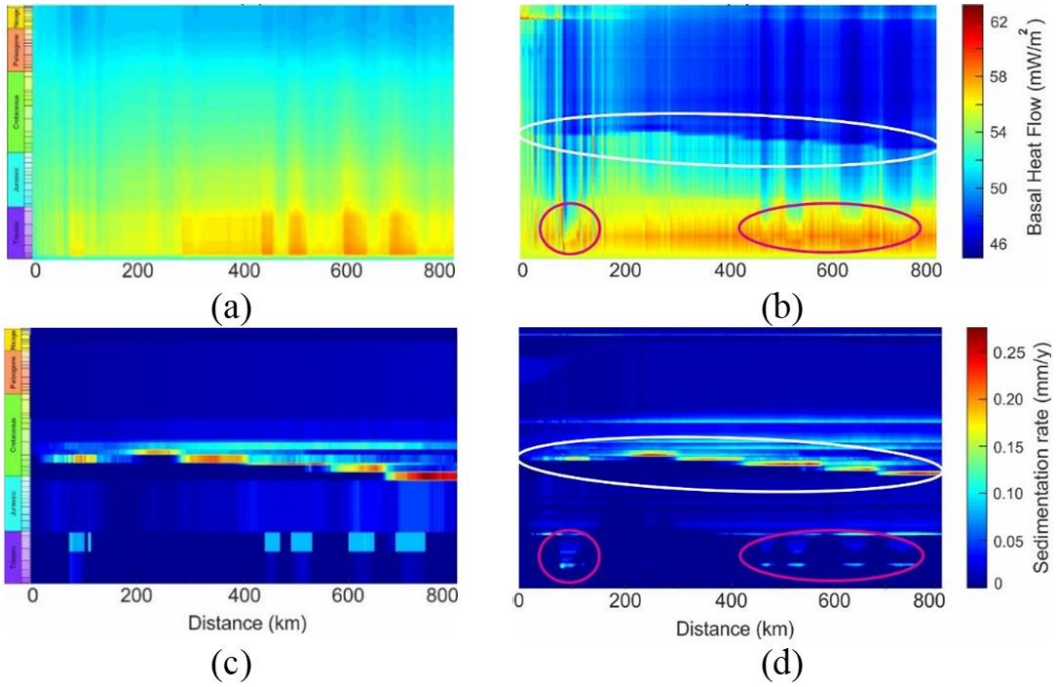

Figure 12. Spatiotemporal variations of the basal heat flow and sedimentation rate derived in BFTM- (a, c) and CSTM-based simulators (b, d). The legend on the right corresponds to both pictures in each line (Peshkov et al., 2021a).

We can see that the sedimentation rate (b) controls the basal heat flow values (Figure 12d) for the CSTM-based solution; that is, the higher the sedimentation rate, the lower the heat flow values. As a result, the blanketing effect (De Bremaecker, 1983; Lucazeau and Le Douaran, 1985; Theissen and Rüpke, 2010; Wangen, 1995) reduces the values of basal HFD by ~4 mW/m^2 within a 5 Ma period (the white ovals in Figure 12b) and by ~2.5 mW/m^2 within a 3 Ma period in the rift graben areas (the violet ovals in Figure 12b). An increase in heat flow is observed over the last 25 Ma (Figure 12b), which is explained by two geological events: a Paleogenic erosion event and a decrease in paleotemperatures on the surface. The blanketing effect is not observed for the BFTM-based basal heat flow (Figure 12a). This fact can be explained by not accounting for the coupling of the structural and thermal evolutions. In addition, the BFTM-based approach underestimates the sedimentation rates, which are reported in Theissen and Rüpke (2010). A comparison of basal heat flow has shown that the blanketing effect and sediment-stretching processes are critical to

an assessment of the West Siberian Basin's thermal regime. The BFTM-based approach overestimates basal heat flow in the most buried parts during the Neocomian period.

This marked difference in the paleo-heat flows leads to a striking discrepancy in the modelling of critical moments and hydrocarbon generation (Figure 13). The study observes that the total volume of hydrocarbons predicted by the BFTM-based thermal solution is ~86% higher than that predicted by the CSTM-based thermal solution (1410 Mtonnes vs 756 Mtonnes, respectively). The Bazhenov Fm makes the most significant contribution to the misfitting of petroleum system modelling results. In addition, we observe an average discrepancy in the critical moment of up to 12 Ma, while the values of the TR at the exact moment can differ by up to ~86%. These consequences are directly related to the blanketing effect in the Cretaceous period.

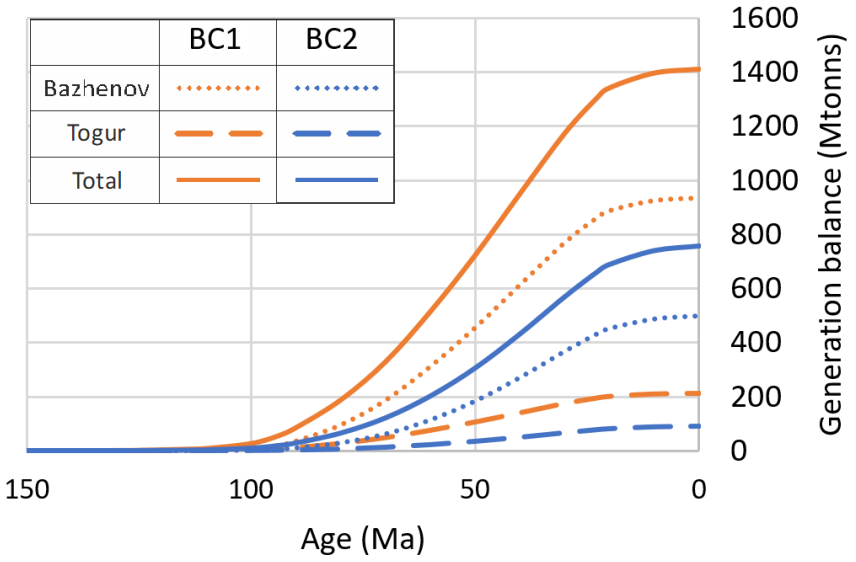

Figure 13. Estimation of source-rock generation mass calculated using a BFTM-based simulator with different boundary conditions: BC1 (BFTM-based) and BC2 (CSTM-based) (Peshkov et al., 2021a).

3.2.2 Conclusions

The study demonstrates that incorrect assumptions in the basal heat flow history reconstruction may lead to significant errors in the results of the petroleum system modelling. Quantitative estimations have been ob-

tained for the West Siberian Basin. The CSTM-based approach's accounting for the blanketing effect of Neocomian sedimentation, which peaks at ~0.25 mm/year, allowed us to re-estimate the masses and timing of hydrocarbon generation. Thus, the BFTM-based approach overestimated the mass of hydrocarbons by up to 86 wt% and was ahead of the critical moment by up to 12 Ma. These results indicate the advantages of using the CSTM-based approach instead of the BFTM-based approach for BPSM.

The provided case study also demonstrated the benefits of combining the best routines of different software packages to create comprehensive and reliable workflow solutions. It is necessary to dig for the best solution, as software developers' have different goals when creating their BPSM software. However, they all, in one way or another, strive to make their solutions as perfect as they can be. The workflow given in this chapter is an example of a procedure whereby the most consistent thermal solution is combined with the most advanced petroleum system simulator in order to reduce thermal and petroleum system modelling uncertainties.

3.3 A case study from the south-western Barents Sea

This section demonstrates a case whereby the BFTM-based approach used in Duran et al. (2013a) leads to overestimation in the basin historical temperatures compared to the CSTM-based approach. This overestimation can lead to the possible overestimations in pore pressure regimes that are considered in Duran et al. (2013a) as the main mechanism of gas leakage from the reservoir in the Hammerfest Basin. A detailed discussion of this subject is given in Peshkov et al. (2021b).

3.3.1 Geological setting

The geological setting of the epicontinental south-western Barents Sea is well studied and described in a number of works (e.g. Faleide et al., 2008; Gac et al., 2018; Ohm et al., 2008), and a brief overview of the geological evolution of the Hammerfest Basin (Figure 14 and Figure 15) is given in Peshkov et al. (2021b). This section only briefly outlines the key petroleum system elements, fields, and gas chimneys.

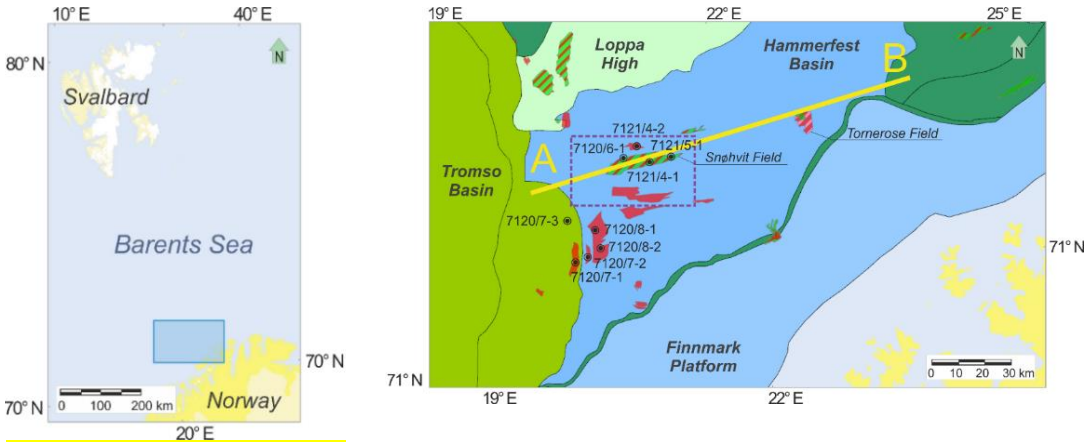

(a) (b)

Figure 14. (a) Location of the study area in the south-west Barents Sea; (b) The Hammerfest Basin with hydrocarbon fields (shown in red and green) and wells locations (according to ('Norwegian Petroleum Directorate')). The purple-dashed box delineates the 3D seismic area surveyed by Mohammed et al. (2016).

According to a petroleum system analysis by Duran et al. (2013a, b), the Triassic Snadd and Kobbe Fms and the Jurassic Hekkingen Fm are the primary source rocks, while the Jurassic Stø and Tubåen Fms are the

primary reservoirs (Figure 15a) in the Hammerfest Basin. The Stø Fm reservoir in the Snøhvit field area consists of natural gas with an oil leg, while the Tornerose field accumulates pure gas (Duran et al., 2013a, b).

Several gas chimneys traced from the primary Stø Fm reservoir in the Snøhvit field have been observed by various researchers (Duran et al., 2013a; Mohammedyasin et al., 2016; Ostanin et al., 2017; Vadakkepuliyambatta et al., 2013) (Figure 15b). Mohammedyasin et al. (2016) applied high-quality pre-stack time-migrated (PSTM) 3D seismic data interpretations (Figure 15b) to analyse the gas leakage's source and pathways. Geometrically, the chimneys are determined to be tubular-shaped (Chimney 1), cone-shaped (Chimney 2), and Christmas tree–structured (Chimney 3) (Figure 15b). The lateral extension of the chimneys varies from ~1 km to ~10 km, with decreasing depth. The effective diameters of Chimney 1 and 2 decrease in the downward direction, while Chimney 3 has a Christmas-tree geometry.

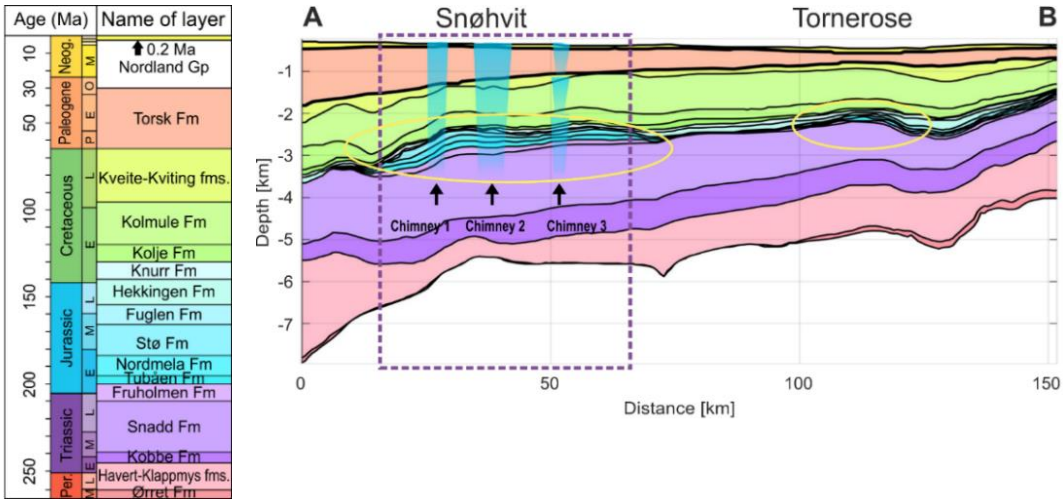

(a) (b)

Figure 15. (a) The chrono-stratigraphic column of the profile under study. The column colours and layer names correspond to the colours given to the section's layers in (b), which shows the chrono-stratigraphy along the line A–B in Figure 14. The violet-dashed box delineates the study area surveyed by Mohammedyasin et al. (2016), while the hydrocarbon discoveries Snøhvit and Tornerose are represented by the yellow ovals. The chimneys are shown in blue.

3.3.2 *Initial data*

The history of the basin begins with the deposition of the Ørret Fm in Permian, a little over 250 Ma ago. Sixteen layers represent the stratigraphic section from the Late Permian to the present-day seabed (Figure 16).

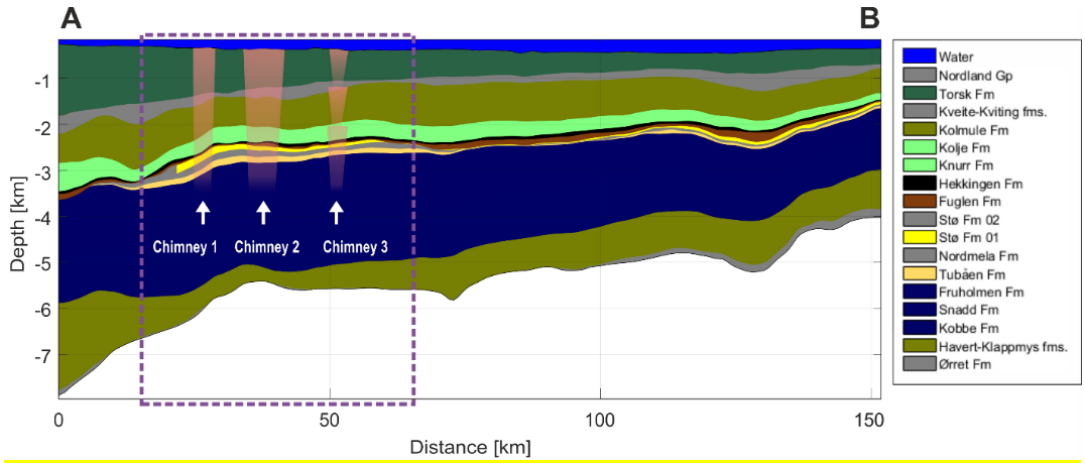

(a)

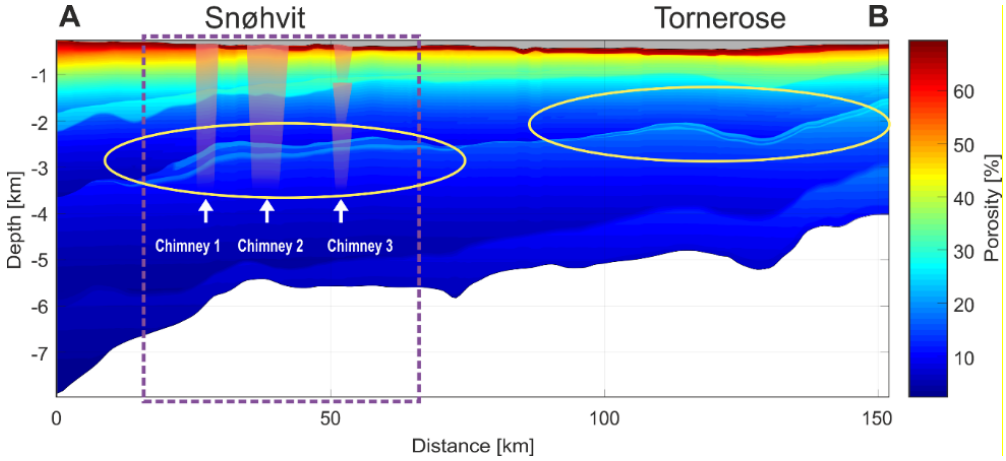

(b)

Figure 16. Present-day modelled (a) lithology infill and (b) porosity, with chimneys, schematically highlighted in pink according to Mohammedyasin et al. (2016); the violet-dashed boxes delineate the area surveyed by Mohammedyasin et al. (2016); in (b), the yellow ovals show the areas of maximum porosity of the primary reservoirs according to Duran et al. (2013a).

In the model, each layer is defined by the lithology infill. The corresponding lithology description for each layer and the corresponding petrophysical properties are presented in Table 3 (based on Duran et al.,

2013a). There are no changes to lithology for each layer, except for the main reservoir in the Stø Fm, which changes laterally from sandstone (Stø Fm 01) to siltstone (Stø Fm 02) in the east-west direction at a lateral position of 28 km (Figure 16a).

The Oligocene–Miocene erosional event occurred between 29 and 15 Ma (Duran et al., 2013a). The eroded thicknesses range from 140 to 840 m, with the thicknesses increasing from southwest to northeast. The glacial activity during the Pliocene–Pleistocene period is not introduced in the model.

Table 3. Material properties and lithological characteristics of modelled stratigraphic units (based on Duran et al., 2013a).

Layer	Colour[B]	Lithology	Physical properties[A]					
			φ_0	B	ρ	λ	C_ρ	Q
			(%)	(km)	(kg/m^3)	(W/m/K)	(J/kg/K)	(μW/m^3)
Nordland Gp		Siltstone (organic lean)	55	1.96	2720	2.05	921	1
Torsk Fm		Shale (organic lean, typical)	70	1.20	2700	1.70	879	2
Kveite-Kviting fms.		Siltstone (organic lean)	55	1.96	2720	2.05	921	1
Kolmule Fm		Shale (organic lean, silty)	67	1.20	2700	1.77	879	2
Kolje Fm		Shale (typical)	70	1.20	2700	1.64	879	2
Knurr Fm		Shale (typical)	70	1.20	2700	1.64	879	2
Hekkingen Fm		Shale (organic rich, 8% TOC[C])	70	1.20	2500	1.20	879	3
Fuglen Fm		Shale (organic lean, siliceous, typical)	70	1.20	2710	1.90	879	1
Stø Fm 01		Sandstone (typical)	41	3.23	2720	3.95	837	1
Stø Fm 02		Siltstone (organic lean)	55	1.96	2720	2.05	921	1
Nordmela Fm		Siltstone (organic lean)	55	1.96	2720	2.05	921	1
Tubåen Fm		Sandstone (clay poor)	42	3.33	2700	5.95	837	0
Fruholmen Fm		Siltstone (organic rich, 2–3% TOC)	55	1.96	2700	2.00	921	1
Snadd Fm		Siltstone (organic rich, 2–3% TOC)	55	1.96	2700	2.00	921	1
Kobbe Fm		Siltstone (organic rich, 2–3% TOC)	55	1.96	2700	2.00	921	1
Havert-Klappmys fms.		Shale (organic lean, silty)	67	2.33	2700	1.77	879	2
Ørret Fm		Siltstone (organic lean)	55	2.44	2720	2.05	921	1

[A] Properties of rock matrix: ρ – density, A – radiogenic heat production, C_ρ – specific heat capacity, λ – thermal conductivity. Parameters of rock by Athy's low: φ_0 – surface porosity; B – scale factor.

[B] Colour codes correspond to the lithology units from Figure 16a.

[C] Total organic carbon.

We used the CSTM-based approach to reconstruct the basin's structural and thermal evolution; for this reason, the lithosphere was included in the simulations. The initial thickness of the upper crust, lower crust and mantle are 20 km, 20 km and 100 km, respectively. The modelling of the rifting processes assumes that there is a differential thinning of the crust and the mantle. According to Reemst et al. (1994) and Skogseid et al. (2000), the Hammerfest Basin has experienced four rift phases; however, the model includes only three of these (Triassic, Jurassic–Cretaceous, Palaeocene–Early Eocene), since the first rift phase (Devonian–Carboniferous) occurred earlier than the model's first horizon.

The boundary condition is defined at the lithosphere base as a constant temperature of 1300 °C (McKenzie, 1967; Parsons and Sclater, 1977). The SWI temperature varies between 10 and 25 °C throughout the Paleozoic–Pleistocene period (Wygrala, 1989). The temperature does not go above 3 °C in the interglacial Pleistocene periods (Archer et al., 2004; Siegert and Marsiat, 2001). At present, the surface temperature is assumed to be 6 °C (Mienert et al., 2005).

The case study uses TecMod's automatically reconstructed (Rüpke et al., 2008) PWD values.

3.3.3 Calibration

The simulator automatically calibrated the stratigraphy section (Poplavskii et al., 2001; Rüpke et al., 2008); less than ten forward simulations were needed to match the present-day layers' thicknesses. The relative difference between the simulated and observed formation thicknesses is less than 1%.

The calculated thermal parameters were then calibrated against temperature and vitrinite reflectance data from a series of wells. The plots in Figure 17 cumulate the data from the following wells: 7120/6-1; 7121/4-1; 7121/4-2; 7121/5-1; 7120/7-1; 7120/7-2; 7120/7-3; and 7120/8-1. 7120/8-2 located close to studying profile (Duran et al., 2013a and links therein) (Figure 15b). The vitrinite reflectance is computed using the EASYRo model (Sweeney and Burnham, 1990), and the thermal calibration is presented for two pseudo-wellbores at 35 km and 129 km of the studying profile.

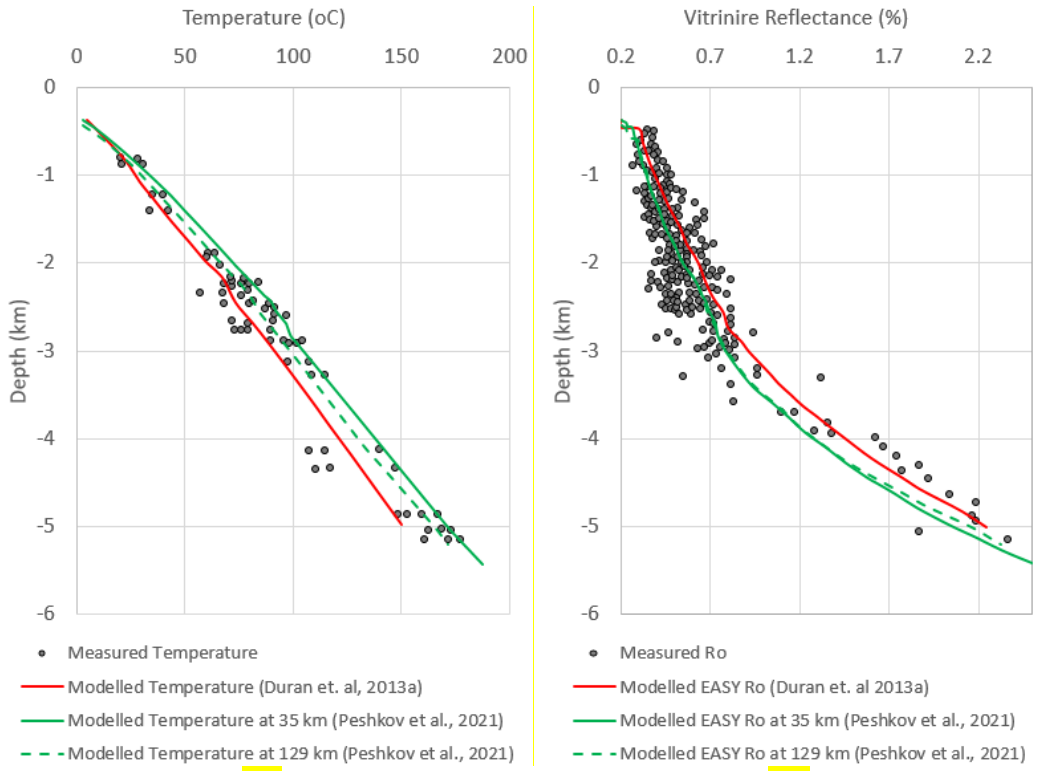

(a) (b)

Figure 17. Comparison of the calibration results for (a) temperature and (b) vitrinite reflectance for datasets from Peshkov et al. (2021b) and Duran et al. (2013a).

3.3.4 Results and discussion

The results of our basin modelling differ from the results presented in Duran et al. (2013a) and Ostanin et al. (2017). These previous works use the same basal heat flow trend derived from the modified McKenzie (1978) model, which served as the lower boundary condition for a basin bottom during the thermal history reconstruction. Thus, the thermal solution was computed only for a basin domain, using the BFTM-based approach. The heat flow accounted only for a response from the lithosphere deformation, ignoring the blanketing effect (Lucazeau and Le Douaran, 1985; Wangen, 1995).

Duran et al. (2013) perform thermal calibration for the entire 3D model using only one modelled well; methodically speaking, this is a rough assumption. However, we can still compare the results of our calibration. For a more transparent assessment and comparison, we present

data from two locations corresponding to the maximum drawdown of the temperature profile in the Tornerous field area (129 km) and the maximum value increases in the Snøhvit field area (35 km). Figure 17 shows that, at a depth of 3 km, the underestimation of the present-day temperature in the work of Duran et al. (2013) (relative to our results) varies from 11 to 16 ^{o}C, with an overestimation of the vitrinite reflectance for both temperature values of 0.11 Ro%. It is important to note that, with such a spread in the calibration data values used, we can assert that both the Duran et al. (2013a) model and our model are calibrated satisfactorily. In addition, it is essential to mention that both models use the same stratigraphy section, erosion thickness and material properties of sedimentary rocks.

The temperature overestimation over time by BFTM based model performed by Ostanin et al. (2017) is presented in Figure 18. In the Snøhvit area, the surface of Kobbe Fm, as calculated by Ostanin et al. (2017), has higher temperature values of up to 45 °C due to not ac-counting the blan-keting effect, while the present-day values match.

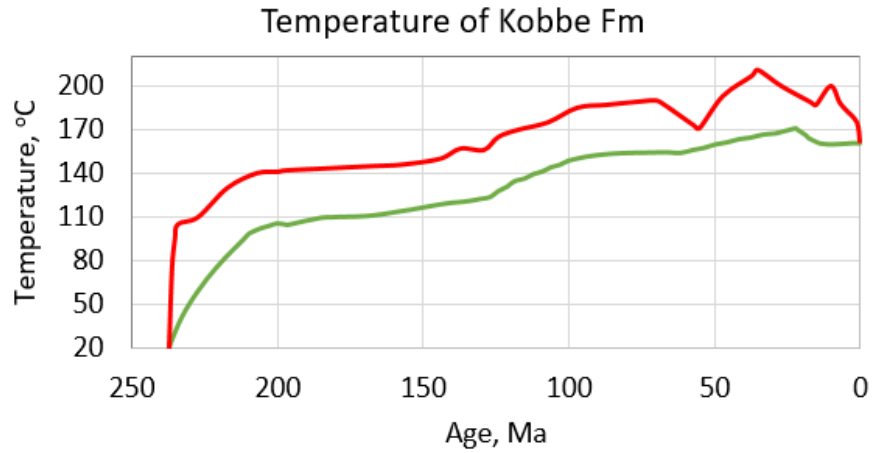

Figure 18. Comparison of the temperature evolution over time for the Kobbe Fm surface in the Snøhvit field area: the red line shows figures by Ostanin et al. (2017), while the green line shows figures from the present study.

The overestimation of temperature results in a higher maturity rank for source rocks. For example, the present-day value for vitrinite reflec-tance in Snadd Fm in the Snøhvit area is estimated using the BFTM-based approach as being ~1.05 Ro% (Ostanin et al., 2017); in comparison, our estimates, which use the CSTM-based approach, are close to 0.8 Ro%.

Thus, the estimates of TR, a mass of generated hydrocarbons, and the timing of the expulsion, migration and preservation of the analysed source rocks in the Kobbe, Snadd and Hekkingen Fms can contain significant errors, as has been demonstrated in Peshkov et al. (2021a), notwithstanding the satisfying well-data calibration performed in Duran et al. (2013a) and Ostanin et al. (2017).

Duran et al. (2013a) consider the chimney-formation mechanisms as a result of the impact of the Pliocene–Pleistocene glaciation cycles on the pore pressure regime. The primary reason for hydrocarbon loss from the Stø Fm reservoir in the absence of faults is due to the high pore pressure formed during the source rock maturation and seal capillary failure during the ice-loading peak. However, Ostanin et al. (2017) have proved that the pressure gradients do not reach values enough to frack the Fuglen Fm and Hekkingen Fm seal rocks in the model of Duran et al. (2013a). Additionally, we have shown that the source rocks' formations' temperature history performed using the BFTM-based approach was overestimated by both Ostanin et al. (2017) and Duran et al. (2013a). That means that it is impossible to obtain the natural hydrofracking of the overlying rocks, and the gas-leakage formation mechanism should be reconsidered. See details about another mechanism of chimneys formation in the work of Peshkov et al., (2021b).

3.3.5 Conclusions

In the Hammerfest Basin case study, it was demonstrated that the BFTM-based modelling results obtained by Duran et al. (2013) overestimate the maturity rank on 0.11 Ro%, at temperature overestimation varying in range from 11 ºC to 16 ºC at a depth of 3 km, relatively to CSTM-based approach. After comparing with Ostanin et al. (2017), it has been demonstrated that the use of the BFTM-based approach (instead of the CSTM-based approach) could lead to errors in the determination of temperatures in the past of up to 45 °C and in the present-day vitrinite reflectance of 0.25 Ro% (that is, 1.05 Ro% instead of 0.8 Ro%), despite the calibration of the thermal model in the well location points.

The errors in the determination of the late oil window (instead of the main oil window) lead to errors in estimations of the generation and

preservation of hydrocarbons, the oil and gas ratio and pore pressure. Incorrect pore pressure estimations could also lead to an incorrect forecasting of possible capillary failure and incorrect interpretations of a primary gas-leakage mechanism.

Chapter 4. Reducing the uncertainties in thermal history reconstruction by considering basement heterogeneity based on gravity data

Chapter 4 examines the role gravity data analysis plays in reconstructing thermal histories and petroleum system modelling for two basins with different basement structures. In addition, the so-called 'express estimation method' is presented in this chapter, highlighting the need to understand the importance of considering the HB when conducting thermal history reconstruction in full-rank 3D basin models.

The first object under study is the West Siberian Basin, which has a heterogeneous sub-basin structure (Section 4.2). This case study demonstrates how basement heterogeneity in density and in thermal properties reconstructed via gravity analysis can affect petroleum system modelling results. The impact of basement heterogeneity on thermal models and on source-rock maturity models is analysed through a comparative analysis, with a reference model built that has a laterally homogeneous basement. The uncertainties of the input basement's density and thermal properties are analysed through a sensitivity analysis.

The second object under study is the Okhotsk Sea Basin (Peshkov et al., 2019, Section 4.3), whose basement heterogeneity is not currently known. This case study considers two scenarios with different basement geometries. One scenario is fitted with seismic data and another with gravity data, since it is not possible to fit both of these calibration parameters simultaneously. Here, the density and thermal properties of the basement are distributed uniformly per strata. These scenarios consider two extreme solutions to the reconstructed thermal history in order to analyse uncertainty in the modelling of petroleum systems. This formulation of the problem aims to show the role gravity analysis plays in a scenario featuring a uniform distribution of density and thermal conductivity properties per strata.

The study of the impact of gravity data calibration on the accuracy of thermal history reconstruction (and, hence, of petroleum systems modelling) is assessed using a CSTM-based approach with the help of the Tecmod software package.

4.1 A workflow for the reconstruction of heterogeneous basement structures using gravity analysis and geological maps

The section describes a newly developed method for the express estimation of the effect of basement heterogeneity on thermal history reconstruction. The method assumes the construction of a set of models with HBs, allowing for comparative analysis with a reference model containing a laterally homogeneous basement. The workflow for 2D basin model construction and calibration used in the method is presented in Figure 19. This workflow, generally speaking, repeats the standard workflow seen in, for example, Hantschel and Kauerauf (2009) and Peters et al. (2017) and is extended by a newly proposed reduced-rank inversion (Figure 19, Step 3) that allows for basement heterogeneity reconstruction.

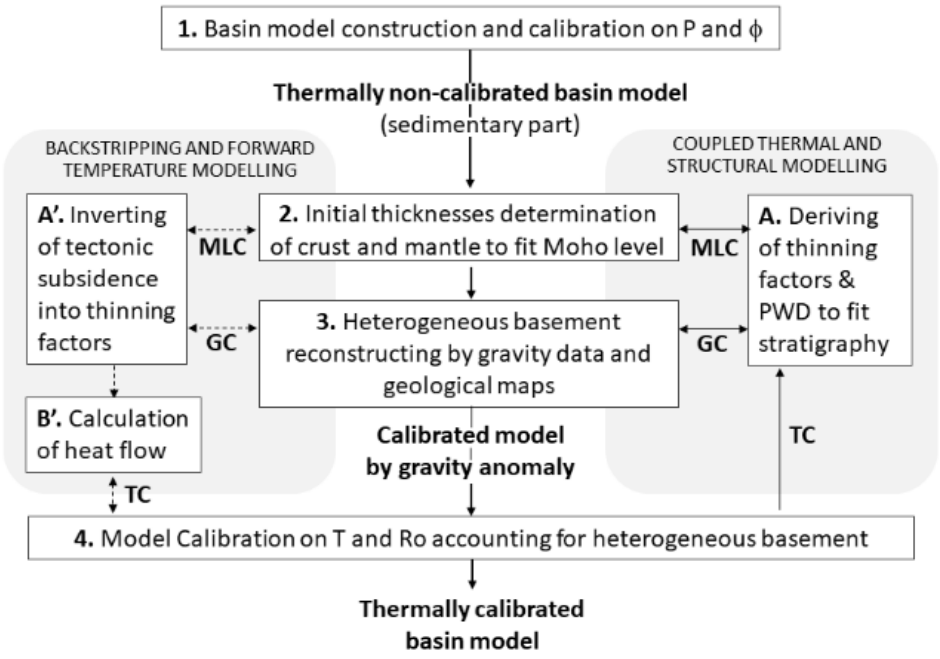

Figure 19. General workflow of the thermal history reconstruction of a riftogenic basin with an HB, where φ is porosity, P is pressure, T is temperature, Ro is vitrinite reflectance, PWD stands for PWD, MLC stands for Moho-level calibration, GC stands for gravity calibration, and TC stands for thermal calibration. The solid arrows show the path used in the case study; the dashed arrows show the path of the backstripping-based solution, and the bidirectional arrows indicate the additional simulations used during model calibration.

The set of models includes the following: (1) a model with laterally homogeneous basement properties that serves as a reference model (Model 1); (2) a model with directly determined HB properties (Model 2) based on the workflow from Figure 1; (3) two models with minimum (Model 2: ρ_{min}) and maximum (Model 2: ρ_{max}) possible density values, which are used to evaluate the impact of uncertainty in density estimation on thermal history reconstruction (following Figure 19); and (4) a series of sensitivity analysis models, which will be used to assess the impact of uncertainties in thermal conductivity in the HB on the predictions of thermal history and on petroleum system maturity in all models. Simultaneously considering uncertainty evaluations in the HB for density and thermal conductivity allows us to obtain the maximal possible range of associated heat flow solutions.

A step-by-step workflow for the models' construction is presented in Figure 19, with a corresponding description below. A detailed description of the reduced-rank inversion included in the workflow is presented in Figure 20.

In Step 1 (Figure 19), a classic basin modelling workflow (described, for example, by Hantschel and Kauerauf (2009)) is used to create a sedimentary cover model. The model is calibrated on measured porosity (φ) and pore pressure (P), producing a thermally non-calibrated geological model of a basin.

In Step 2 (Figure 19), homogeneous basement layers are added into the model. Estimations of the present-day Moho depth were used to determine the crust's initial thicknesses (i.e., before the rifting extension). The thermal calibration of the model performed in Step 4, and avoiding Step 3, gave us a reference model without any basement heterogeneity (Model 1); this model should be used in Step 3 as a precursor to constructing models with HBs (i.e., Model 2, Model 2: ρ_{min} and Model 2: ρ_{max}).

Following these steps, the modelling workflow is bifurcated according to the modelling approach selected, which may involve either coupled or decoupled thermal and structural solutions. We recommend the coupled thermal and structural approach (Rüpke et al., 2008) since it considers sediment stretching and coupled temperature and isostasy modelling

with subsidence, and does not require information on the PWD, in comparison to the BFTM approach (Clark et al., 2014; Theissen and Rüpke, 2010).

Importantly, while the two approaches both obtain the lithosphere's reconstructed configuration, they do so by following different paths. The backstripping-based approach follows the modelling of stretching factors in order to fit tectonic subsidence to theoretical subsidence, while PWD is used as an input parameter ('A'). This procedure is described by Hantschel and Kauerauf (2009). Next, heat flow calculation is performed ('B').

In the coupled thermal and structural solution (A), stretching factors and PWD are iteratively calculated using the regularisation procedure, by fitting the modelled stratigraphy section to the input stratigraphy section, with simultaneous temperature modelling (see, e.g., Poplavskii et al. (2001) and Rüpke et al. (2008)).

In Step 3 (Figure 19), the reconstruction of the HB properties and geometry (the width and thickness of each block of the HB) starts. First, the model with the directly determined properties concerning the geometry of the HB was built (Model 2). Here, the following assumptions have been made:

- The upper part of the basement is heterogeneous.
- Under the HB is a crystalline basement.
- The densities of the lithospheric layers, upper (ρu_crust) and lower (ρl_crust) crusts and the lithospheric mantle (ρl_mantle) are constant and change with temperature.
- The present-day width of each rectangular block is determined based on the basement maps.
- The first approximation of the thickness of each HB block is set.
- The physical properties of each heterogeneous block are based on lithological descriptions from maps and their interpretations, using standard mixing rules (Hantschel and Kauerauf, 2009).

The reconstruction of the basement's geometry and density (shown in Figure 20) uses an iterative approach that is similar to Bott's (1960) method.

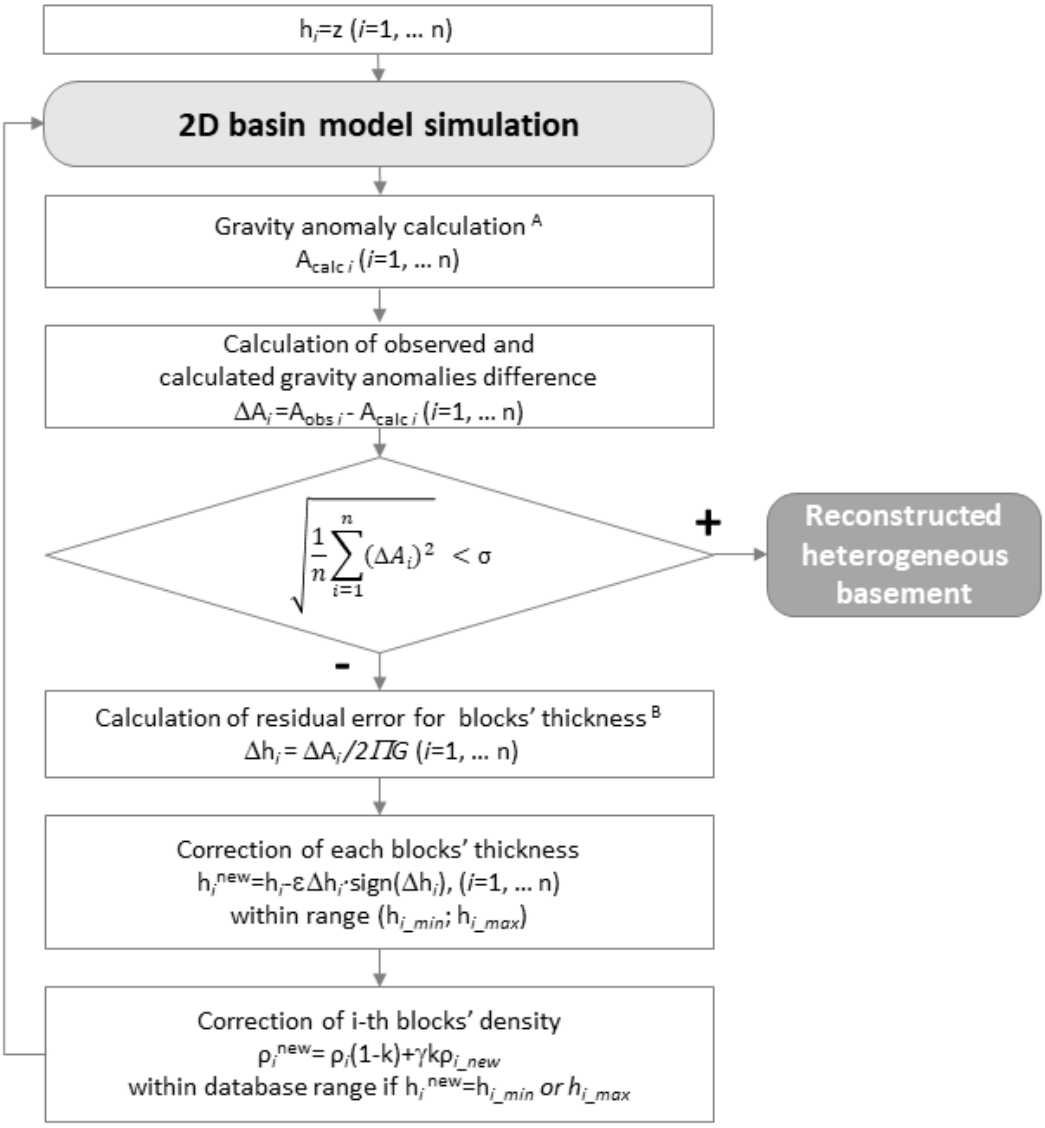

Figure 20. Inversion procedure reconstructing the geometry and density of an HB. [A] (Heiland, 1940), [B] (Bott, 1960).

When the above-mentioned assumptions about the basement properties and lateral extension were introduced into the model, the first approximation (z) for each (i = 1, … n) block's thickness (h_i) was made; for example, z = 1 km. Next, the model was simulated. The gravity anomaly was then calculated according to the formula for vertically sided two-dimensional blocks presented in Heiland (1940, p. 152). Further to this, the difference (ΔA_i) between the observed (A_{obs}) and calculated (A_{calc}) gravity anomalies was estimated for each *i* block.

The stopping condition of the inverse problem was then used as the standard error, as in, e.g., Essa (2012) and Martyshko et al. (2018):

$$\sqrt{\frac{1}{n}\sum_{i=1}^{n}(\Delta A_i)^2} \leq \sigma, \quad (1)$$

where σ is the desired accuracy. Some deviations of the modelled gravity anomaly from the measured gravity anomaly may result from compositional differences (e.g., Christensen and Mooney, 1995); additionally, 3D density structures that are not considered in the model may contribute to uncertainty in the 2D gravity modelling (Minakov et al., 2012). Otherwise, block thicknesses (or, in rare cases, densities) need to be refined.

Next, the residual error of thickness (Δh_i) was calculated for each *i* block using the formula from Bott (1960):

$$\Delta h_i = \Delta A_i / 2\pi G, \quad (2)$$

where G is the gravity constant. Following this, the new thickness (h_i^{new}) of the block is calculated as

$$h_i^{new} = h_i - \varepsilon \Delta h_i \times sign(\Delta hi_i), \quad (3)$$

where ε is the regularising multiplier, ranging from 0 to 1, defined by the user. If the new block thickness (h_i^{new}) is greater than the maximum (h_{i_max}) or less than the minimum (h_{i_min}) determined thicknesses for the *i* block, correction of the *i* block density (ρ_i) is required:

$$\rho_i^{new} = \rho_i \times (1 - k) + \gamma k \rho_i, \quad (4)$$

where *k* is a correction factor ranging from 0 to 1 that is defined by the user and γ is a multiplier equal to +1 if $h_i^{new} = h_{i\_min}$ and –1 if $h_i^{new} = h_{i\_max}$. In addition, h_{i_max} can be limited by h_{i_crust}, for example, while h_{i_min} can be limited by drilling data.

After the correction of values h_i and ρ_i for i = 1,…n (as recommended in Bott (1960)), the basin model was simulated and the gravity anomaly was calculated. The inversion procedures were then rerun before Condition (1) was complete.

There are cases when gravity data fitting for the block is completed along only part of the block. Therefore, the block in question needs to be split vertically, into several sub-blocks. The Δh_i for each sub-block should then be calculated separately. This procedure fits the gravity anomaly better (Bott, 1960), aiding the search for the best solutions and further estimations in thermal regime changes.

Databases of the petrophysical properties of rocks often contain errors or provide properties that are often not reliable (Chekhonin et al., 2020; Waples, 1998). Therefore, whenever possible, the most advanced experimental techniques for the determination of thermal conductivity should be used (see, e.g., Meshalkin et al. (2020) and Popov et al. (2019)) in order to reduce uncertainties in the properties derived from the database.

However, such a comprehensive and time-consuming thermal property analysis is beyond the scope of this work. For this reason, we followed the customary approach to setting the thermal properties of rocks in the model, although we remained aware that incorrect, frequently underestimated thermal conductivity values (due to contact resistance (Popov et al., 2014) or disregarding saturation (Duchkov et al., 2013)) lead to statically underestimated heat flow values (Chekhonin et al., 2020). The physical properties of the rock used in the lithological mixtures, which included density (ρ), specific heat capacity (C_ρ), radiogenic heat production (A) and thermal expansion (α), were calculated using the arithmetic mean rule, while thermal conductivity (λ) was calculated using the geometric mean rule. Measurements conducted on rock samples from outcrops and data from well logs and core samples may significantly narrow down the ranges of inferred petrophysical properties. Unlike density, thermal conductivity is a non-additive anisotropic characteristic of rocks that is frequently underestimated (see, e.g., Chekhonin et al. (2020)).

During the thermal calibration (Figure 19, Step 4), the value of radiogenic heat production (A) in the crustal layer was varied to fit the wellbore values of temperature (T) and vitrinite reflectance (%Ro) (Lachenbruch, 1968; Waples, 2001). If the thermal calibration does not produce a good fit in some wells, which occurrence cannot be explained by uncertainty in thermal conductivity, then the basement model needs to be refined within the blocks' possible ranges of density and geometry. Thus, the gravity and thermal calibrations complement each other and constrain the diversity of solutions.

In this step (Step 4), Model 2 was built, and (following the workflow in Figure 19) two additional models with minimum (Model 2: ρ_{min}) and maximum (Model 2: ρ_{max}) HB densities were constructed. In contrast to Model 2, these models had a different last assumption from the final above regarding the density of the HB. Here, the minimum and maximum

values for the determined rock lithology were based on a database of Schön (2011).

Sensitivity study was performed using Model 2, Model 2: ρ_{min} and Model 2: ρ_{max} in order to estimate the impact of the uncertainties in the thermal conductivity of the HB on the thermal history reconstruction. The studied ranges of the matrix thermal conductivity (λ) values were ±20% and ±50%, as previously used by Hicks et al. (2012) and Chekhonin et al. (2020), respectively.

When all the models had been built and calibrated and a sensitivity analysis had been performed, the significance of the HB's impact on thermal history reconstruction could be determined. Following the analysis, it should be decided whether the HB is needed in the construction of a full-rank 3D basin model and, if it is required, additional geophysical studies (e.g., deep seismic sounding and density and thermal property measurements) should be planned.

4.2 A case study from the West Siberian Basin

A study of the role gravity analysis plays in the basin thermal regime reconstruction was undertaken with the same dataset that was used in Chapter 3 (Figure 9 and Figure 10). The analysis of gravity data was ignored in Chapter 3, since the study aims to compare two thermal history reconstruction approaches for identical models. The considering of an HB can break the correspondence between the models due to the difference in the modelling approaches used and the capabilities of the software products.

The Western Siberian Basin is a good candidate for evaluation of the proposed express estimation methodology's efficiency because of the two main reasons: first, this basin is one of the largest petroleum provinces in the world (Ulmishek, 2003), and second, most basin modellers prefer to assume the pre-Jurassic strata as a laterally homogeneous crustal layer (see, e.g., Fjellanger et al., 2010; Kazanenkova, 2015; Morozov et al., 2016; Romanov et al., 2005; Safronov et al., 2011)), although these strata actually have a complex heterogeneous nature (Merkulov et al., 2019).

The reason for this assumption about the pre-Jurassic strata is twofold. First, the seismic data along the seismic study profile do not provide reliable reflections that would allow the reconstruction of Palaeozoic sedimentation. Second, according to an appraisal of the existing seismic data from the entire Siberia by Cherepanova et al. (2013), the rifts in our study area cannot be distinguished in the seismic models.

We consider these Paleozoic strata and syn-rift regional-scale intrusion in rift graben zones as an HB that was formed instantaneously, before the modelled Mesozoic–Cenozoic sedimentation. In the literature, the HB is known as the pre-Jurassic folded basement or, less commonly, as the economic basement (Stoupakova et al., 2015; Vyssotski et al., 2006).

4.2.1 Set of basin models

All built basin models have the same configuration: a sedimentary cover, temperature boundary conditions and rifting setting. The models are calibrated using porosity data and pressure regimes, Moho depth and a wellbore temperature data and vitrinite reflectance data. Model 1, the reference model, was constructed by assuming a homogeneous lateral distri-

bution of properties in the basement, introduced by the crust and lithospheric mantle strata. Referring to Figure 19, Model 1 was constructed by applying Steps 1, 2 and 4; thus, Model 1 was not fitted with the observed gravity anomaly. Model 2, Model 2: ρ_{min} and Model 2: ρ_{max} were all built with an HB, following all the steps in Figure 19 and the newly proposed inversion procedure (Figure 20). For our case study, the models labelled Model 2: ρ_{min} and Model 2: ρ_{max} were built with the minimum and maximum density values of the basement's igneous rocks. Based on our modelling results, heterogeneous blocks with a sedimentary genesis had a negligible impact on thermal history reconstruction. Several additional models were used to consider the impact of uncertainty in the thermal conductivity (λ) of the HB on thermal history reconstruction for Model 2, Model 2: ρ_{min} and Model 2: ρ_{max}. These models were referred to as Model 2: $\lambda\pm20\%$, Model 2: $\lambda\pm50\%$, Model 2: ρ_{min}, $\lambda\pm50\%$ and Model 2: ρ_{max}, $\lambda\pm50\%$.

All computations were performed using the non-steady-state coupled thermo-tectono-stratigraphic solver (Poplavskii et al., 2001; Rüpke et al., 2008), using TecMod 2019.1 software.

All the above-described models have the same settings, as follows:

- The sedimentary part of the basin model and boundary conditions repeat the model presented in Section 3.2 and in Peshkov et al. (2021a). All models are constructed under the assumption of the Airy isostasy.
- Since the basin has a rift nature, the lithosphere's stretching factors are found through inverse modelling. The rift period is defined as being from 251 to 228 Ma, with differential thinning of both the crust and the mantle (Vyssotski et al., 2006).
- At the upper boundary, the time-temperature is decreasing trend and is defined within the range 20 to 0 °C, following Isaev et al. (2014). The lower boundary condition on temperature is set at the lithosphere-asthenosphere interface, at a constant value of 1300 °C (Fischer et al., 2010).
- The upper crust, the lower crust, and the initial thicknesses of the lithospheric mantle are set to H_{UC0} = 30 km, H_{LC0} = 10 km and H_{UM0} = 70 km, as in Peshkov et al. (2021a).

- The reference gravity anomaly values along the investigated section were digitised from a map of the Bouguer anomaly that shows the Federal Ural district data (the map is accessible online; see 'Gravimetric map of the Ural federal district' (2019)). The map has an average topographic density of 2670 kg/m^3, with a terrain correction radius of r = 200 km, a normal gravity value derived from the Helmert formula (1901–1909) and a datum correction of −14 mGal to the International Gravity Standardisation Net (Morelli et al., 1972). The gravity survey was performed on a regional scale of 1:7,500,000, with a counter step of ε_c = 5 mGal. No other details of the gravity anomaly map building are known. The uncertainty value was not provided; therefore, ε_t = ±1.5 mGal (which is a typical requirement for a regional-scale Bouguer anomaly map) was assumed (Khmelevskoy et al., 2004; for more detail, see Appendix A, Section A.3.2). The desired accuracy required to fit the model and the measured results of the Bouguer anomaly (see Section 4.1), σ = 6.5 mGal, was defined as the sum of the counter step (ε_c) and the uncertainty value of measurements (ε_t).

Construction of a homogeneous basement: Model 1

Model 1 is based on the simplified assumption of the distribution of homogeneous lateral properties in a basement, namely in crustal and lithospheric mantle strata (Figure 21). The construction of this model corresponds to Steps 1, 2 and 4 in Figure 19. The rock properties used in the model for the sedimentary units are presented in Peshkov et al. (2021a) and for the basement units are presented in Table 4. The basement's rock density (ρ) and thermal conductivity (λ) increase, while radiogenic heat production (A) tends to decrease with depth (Allen and Allen, 2013). The Sekiguchi (1984) model was used to calculate temperature-dependent thermal conductivities.

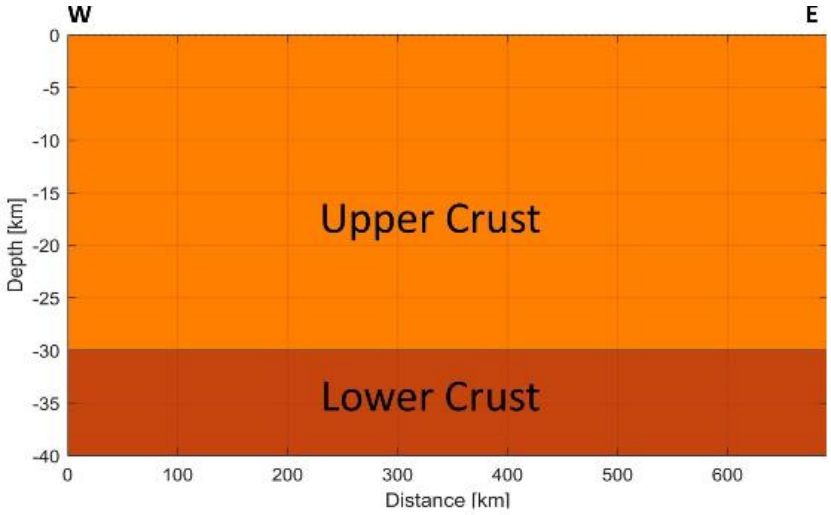

Figure 21. Initial state of the basin configuration of Model 1 before sedimentation at 251 Ma.

Calibration of Model 1

After construction, Model 1 was run to check the calibration on the stratigraphy section, porosity and pressure regimes, Moho depth and gravity anomaly:

- A good match between the modelled stratigraphy and the input stratigraphy sections was obtained, with an approximate convergence misfit of 5%. The result was reached after 15 forward-modelling inversion iterations (Rüpke et al., 2008).
- The used input values of the density and porosity of sediments are the same as in Peshkov et al. (2021a), in which study the modelled porosity and the lithostatic pressure are calibrated. Thus, we observed that Model 1 does not require additional calibration.
- The calculated present-day Moho depth is in good agreement with two published interpretations (Braitenberg and Ebbing, 2009; Cherepanova et al., 2013) within a 190 km interval located to the eastern end of the profile (Figure 22, red line). The absence of the flexural load by the Ural fold belt to the west in the model explains the discrepancy in calculated and published data within the 0 to 190 km interval.
- The gravity anomaly (Figure 23, red line) was not fitted, since the modelled σ_m = 10.5 mGal was greater than the desired accuracy of σ = 6.5 mGal.

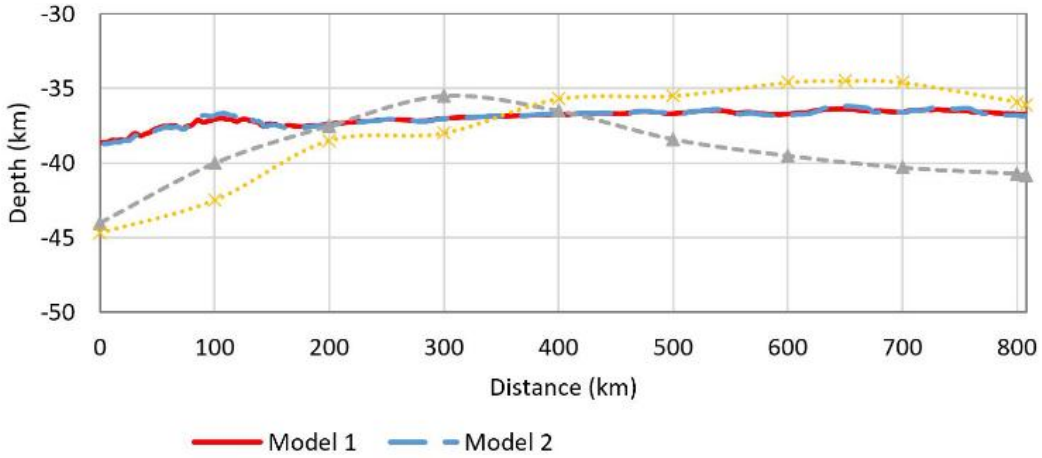

Figure 22. Present-day Moho depth taken from the models and open-source data, with dashed-grey (Cherepanova et al., 2013) and dotted-yellow (Braitenberg and Ebbing, 2009) lines showing the respective findings.

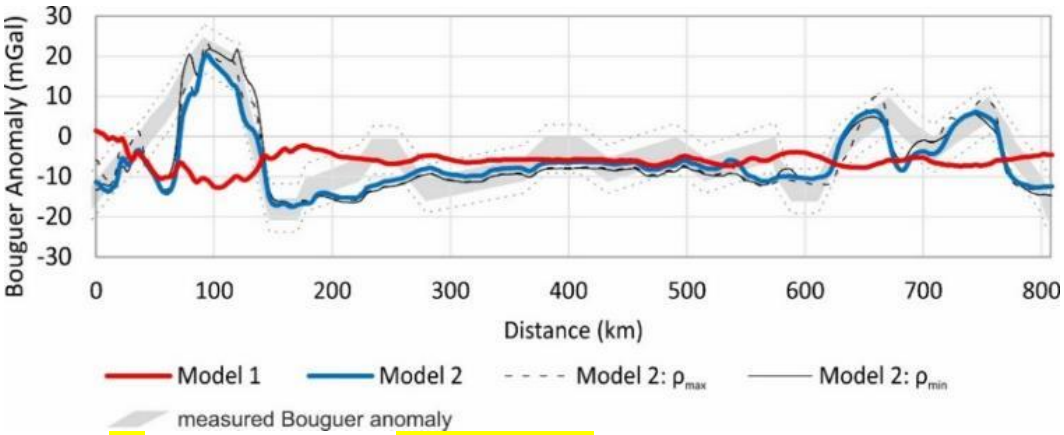

Figure 23. Comparison of the observed Bouguer anomaly data digitised from the gravity map ('Gravimetric map of the Ural federal district,' 2019; grey stripe) and calculated data for Model 1 (solid red line), Model 2 (solid blue line) and two models from the sensitivity study: Model 2: ρ_{max} (dashed black line) and Model 2: ρ_{min} (solid black line). Dotted grey lines show the ±1.5 mGal interval relative to the observed values.

The above calibration steps serve only as a robust quality check of the structural and sedimentary evolution models; the thermal solution needed additional calibration with the wellbore temperature data and vitrinite reflectance data (Figure 24).

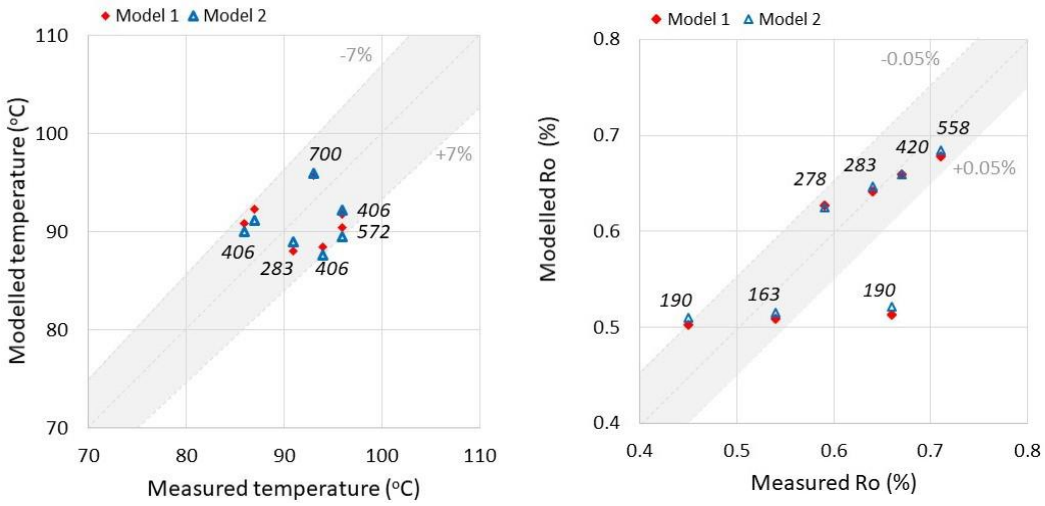

(a) (b)

Figure 24. Calibration results for (a) present-day measured and modelled temperatures and (b) vitrinite reflectance, using the EasyRo kinetic model (Sweeney and Burnham, 1990). The numbers in italics near the data points correspond to the wellbore location (in km) along the profile, while the grey zones show the ±7% area for temperature and the ±0.05% absolute for vitrinite reflectance.

The dataset considered here includes present-day temperatures in the boreholes at profile locations at 283, 406, 572 and 700 km (Figure 24a and Figure 25a) and vitrinite reflectance data in the profile points at 163, 190, 278, 283, 420 and 558 km (Figure 24b and Figure 25a) from Peshkov et al. (2021a). The thermal solution was only calibrated on a regional scale; i.e., without local tuning. An exponential reduction of the radiogenic heat production of the crust (A) from a surface value (A_0) at a rate given by the e-fold length was assumed (Lachenbruch, 1968); see the formula in the footnote of Table 4. The e-fold length parameter selected for Model 1 was equal to 20.4 km, and the well thermal data had a reasonably good match with the modelled thermal regime (Figure 24). Hence, the thermal properties did not need to be optimised in this case.

All the modelled temperature values fell within the ±7% interval relative to the observations (Figure 24a), which means that the discrepancy between the calculated and measured values does not exceed a typical estimation of uncertainty in formation temperature (see details in Appendix A, Section A.3.2). The calibration vitrinite reflectance (%Ro) was per-

formed using the EasyRo model (Sweeney and Burnham, 1990). Most vitrinite reflectance data fell within the deviation range of ±0.05 %Ro (Figure 24b); this is also acceptable, given the uncertainty in %Ro estimation (see details in Appendix A, Section A.3.2).

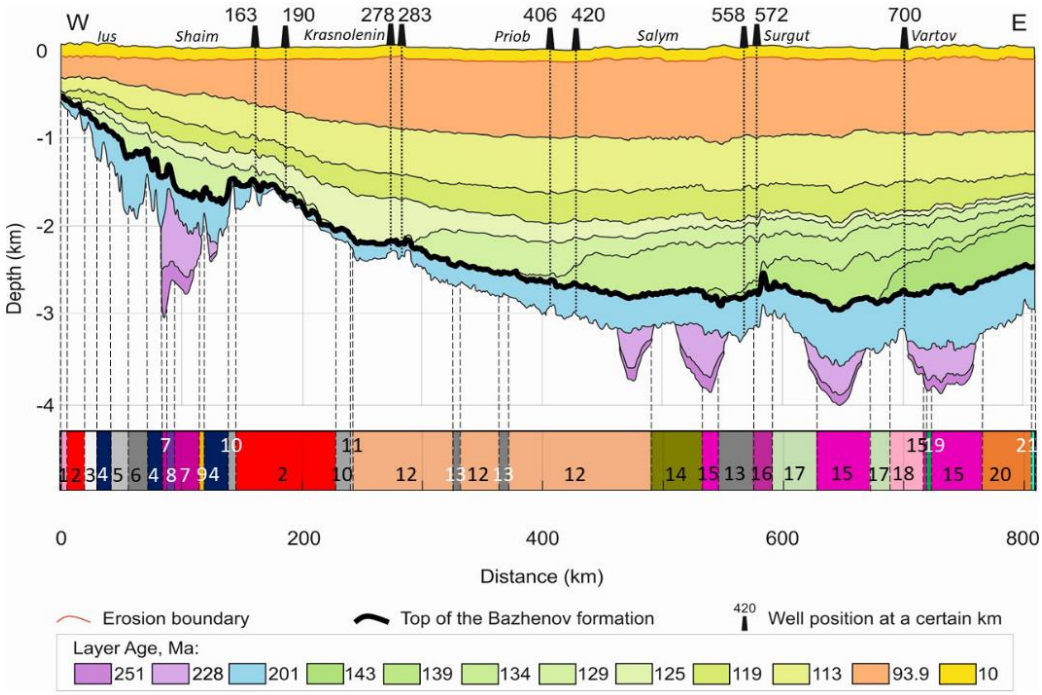

(a)

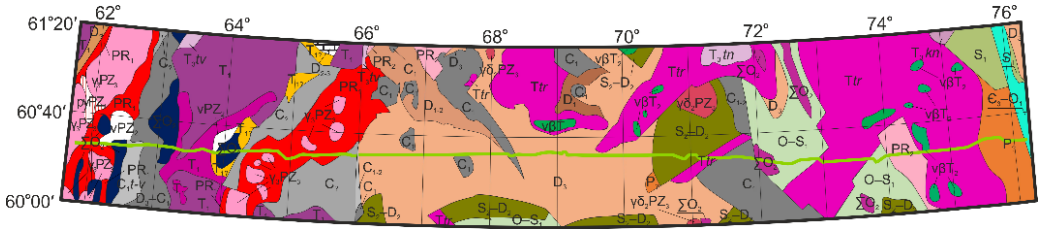

(b)

Figure 25. This figure shows (a) a present-day simplified stratigraphy section of Regional Profile #6 (Vyssotski et al., 2006) linked with the HB blocks' lateral boundaries in Model 2 (modified after Peshkov et al. (2021a)). The numbers of blocks and used colour codes correspond to the material properties in Table 4. The names of petroleum regions are in italic. (b) The geological map of the HB is modified after Ivanov et al. (2009), 'Map of Jurassic formations: P-42 (Khanty-Mansiysk)' (2009) and 'Map of Jurassic formations: P-43 (Surgut)' (2010), while the geological description used in the study blocks is provided in Table 4. The green curve shows the profile location.

The only value of vitrinite reflectance measured for the wellbore at 190 km exceeded the model's permissible confidence interval. Two measured %Ro values for this wellbore (0.45% and 0.66%) were significantly different from each other, even though both were obtained from almost the same depth (depth difference ~100 m). This can be explained by either the random error of measurements (observed deviation for other samples was within ±0.05 %Ro) or the redeposition of organic matter.

The final view of the geological section of Model 1 is presented in Figure 26a.

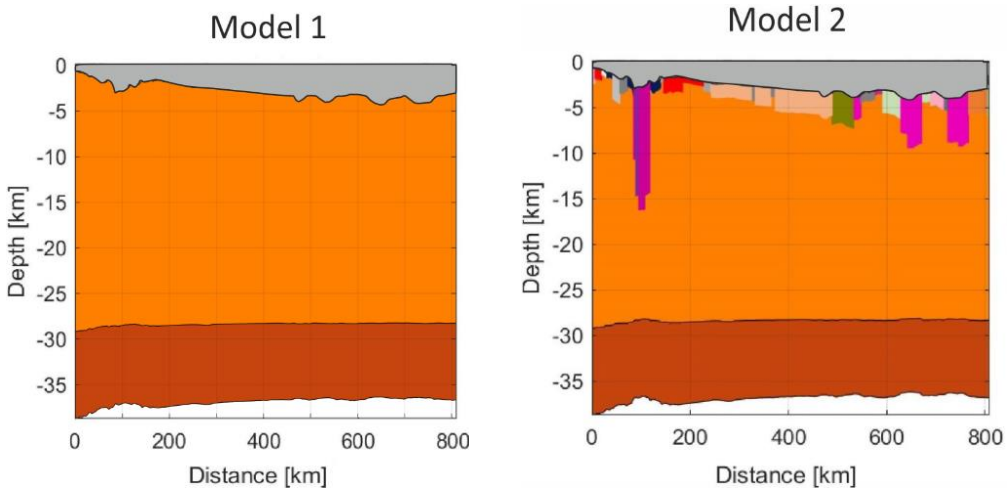

(a) (b)

Figure 26. Reconstructed present-day geological sections for (a) Model 1 and (b) Model 2. The grey area is the basin section. The colour codes beneath the basin section correspond to the basement units presented in Table 4. The corresponding modelled gravity anomalies are presented in Figure 23. For convenience, the lithospheric mantle layer is not shown in this figure.

Material properties of the heterogeneous basement

Following the standard procedure (Hantschel and Kauerauf, 2009), the lithological description was transferred from the maps to bulk material properties for each geological unit. The data taken from the maps (Ivanov et al., 2009; 'Map of Jurassic formations: P-42 (Khanty-Mansiysk)', 2009; 'Map of Jurassic formations: P-43 (Surgut)', 2010) and its interpretation are presented in Table 4.

Table 4. Material properties of basement units.[1]

Unit no.	Colour	Lithology description of basement units[D,E,F]	Physical properties[A] ρ (kg/m³)		α (10⁻⁵K⁻¹)	A (μW/m³)	C_ρ (J/kg/K)	λ (W/m/K)
1		Weathered granite (γ_3PZ_3)	2645	(2500–2800)	2.4	2	760	2.6
2		Sialitic gneiss, schist (PR_3)	2600	(2600[C]–2620[C])	2.4	2	850	3.0
3		Gabbro; (vPZ_2)	2870	(2800–3100)	1.6	0	800	2.9
4		Serpentinite, ultrabasit ($\sum O_2$)	3064	(3100–3340)	1.0	0	830	3.0
5		Terrigenous carbonate deposit ($C_?$)	2766	–	2.6	1	890	2.4
6		Effusive rock (D_3–C_1)	2690	–	1.6	1	820	2.3
7		Effusive mixed tuff (T_1)	2800	(2780[C]–3200)	1.6	1	820	2.3
8		Basalt (T_1)	2840	(2780[C]–3200)	1.6	1	800	1.8 [B]
9		Igneous–sedimentary rock ($T_{1?}$)	2757	–	2.2	1	840	2.3
10		Terrigenous–schist rock (C)	2740	–	2.3	1	920	2.8
11		Organogenic limestone, sandstone, calcareous sandstone and siltstone, basalt, basalt's tuffs ($C_{1–2}$)	2733	–	2.7	1	850	2.7
12		Clay and organogenic limestone, subordinate tufogenic–sedimentary rock, basalt (D_3)	2767	–	2.7	1	840	2.8
13		Organogenic limestone, clay, carbonaceous schist, siltstone, marl, andesibasalt, rhyolite (C_1)	2752	–	2.4	1	870	2.5
14		Siliceous and silty shale, siltstone, basalt, andesibasalt, andesibasalt's tuffs, tufogenic–sedimentary rock, sandstone, gravelite (S_2–D_2)	2749	–	2.1	1	880	2.4
15		Basalt, dolerite, dolerite's tuffs, tufogenic–sedimentary rock, mudstone, siltstone, sandstone, gravelite, andesite, rhyolite (T_{tr})	2809	(2750[C]–3200)	1.8	1	850	2.2
16		Serpentinized dunite, harzburgite, lerzolite, pyroxenite, serpentinite ($\sum O_2$)	2800	(2750[C]–2800[C])	1.0	0	780	4.1[B]
17		Shale, siliceous shale, jasper, limestone, basalt, andesibasalt, andesibasalt's tuffs (O–S_1)	2712	–	2.5	1	860	2.7

[1] Note. [A]Here, ρ is the density (its acceptable range, according to Schön (2015), is shown in parentheses), and α is the volumetric coefficient of thermal expansion. For unit numbers 1–21, A is the radiogenic heat production of the rock matrix. For the crust and lithospheric mantel, A is surface radiogenic heat production (A_0) in the equation $A(z) = A_0 * \exp(z/a_r)$, where A(z) is bulk radiogenic heat production, z is the negative value of a depth (km) and a_r is the length of the e-fold parameter (km) (Lachenbruch, 1968). C_ρ is the rock matrix specific heat capacity, and λ is the rock matrix thermal conductivity at 20 °C. Values are calculated based on the petrophysical database in Hantschel and Kauerauf (2009), using the geometric mean rule used for λ and the arithmetic mean rule used for ρ, C_ρ and A. [B]Questionable values (see the text for details). [C]The manually truncated edge of the density range by Schön (2015) was used to obtain the gravity anomaly calibration for Model 2: ρ_{min} and Model 2: ρ_{max}. A designation of rocks will follow. [D]Ivanov et al. (2009). [E]'Map of Jurassic formations: P-42 (Khanty-Mansiysk)' (2009). [F]'Map of Jurassic formations: P-43 (Surgut)' (2010).

18		Metamorphic schist, sericite–chlorite, sericite and carboneous phyllite, quartzite (PR_2)	2840	(2750[C]–2900)	2.7	1	900	2.8
19		Gabbrodolerite, dolerite ($v\beta T_2$)	2909	(2800–3100)	1.7	0	860	2.4
20		Siltstone and tuff siltstone basalt, basalt clastolavas, andesite, tuffite, rhyolite ($P_?$)	2721	–	2.1	1	860	2.0
21		Clay limestone, greenish-grey with lenses of organogenic clastic limestone ($Є_3$–O_1)	2728	–	2.4	1	850	2.3
		Upper crust	2700	–	2.4	2	1000	3.0
		Lower crust	2900	–	2.4	2	1000	3.0
		Lithospheric mantle	3340	–	3.2	0	1000	3.5

Density (ρ), thermal conductivity (λ), specific heat capacity (C_ρ), radiogenic heat production (A) and the thermal expansion of each block in Model 2 were all defined based on the petrophysical database and the application of the mixing rules (Hantschel and Kauerauf, 2009). These properties were then assigned to Model 2. The Sekiguchi model (Sekiguchi, 1984) is used for the temperature correction of thermal conductivities (λ).

Published rock thermal conductivity data are often unreliable (see, e.g., Chekhonin et al., 2020). Therefore, any justification of the basement's thermal conductivity values requires reliable experimental data and is beyond the scope of this work. Instead, we have suggested quantifying the impact of uncertainty in the thermal conductivity of the HB on thermal history reconstruction by performing a sensitivity analysis, varying the λ of the HB blocks by ±20% and ±50% relative to the values determined from the database.

Two additional comments can be made about the thermal conductivity values obtained from the database (Hantschel and Kauerauf, 2009) (these are marked by [B] in Table 4). The database value of the basalt rocks' matrix thermal conductivity (Table 4, Unit 8) is 1.8 W/m/K, while the measured value of the basalt rocks' thermal conductivity is 1.8 to 3.5 W/m/K (Chekhonin et al., 2020; Clauser and Huenges, 1995; Hantschel and Kauerauf, 2009; Kukkonen et al., 1999; Norden et al., 2020; Robertson, 1988). Similarly, the thermal conductivity of basal rocks from a neighbouring area (the Nizhne–Tabachanskaya area of the Western Siberian Palaeozoic basement) varies from 2.46 to 3.33 W/m/K, according to Duchkov et al. (2017). The value of 4.1 W/m/K connected with the lithological Unit 16 (Table 4) seemed too high for this rock type, since the

thermal conductivity of serpentinite equals 2.1 W/m/K according to Kukkonen et al. (1999), 2.15 W/m/K as per Seipold and Schilling (2003) and 2.77 W/m/K (for the serpentinite sample from the Nizhne–Tabachanskaya area of the Western Siberian Palaeozoic basement) according to Duchkov et al. (2017). Data on the volumetric thermal expansion coefficients (α) were in good agreement with the published values (Allen and Allen, 2013; Haines, 1982; Robertson, 1988).

Density values for the same rock type can exhibit significant variations (see, e.g., the corresponding ranges in Schön (2015)). The variations in density considered in this thesis were taken from Schön (2015, p. 116) and modified (see the values in parentheses, Table 4).

Construction of the heterogeneous basement: Model 2, Model 2: ρ_{min} and Model 2: ρ_{max}

Model 1 (Figure 26a) was used as a precursor to constructing models with HBs, since Steps 1 and 2 in Figure 19 had already been performed. Next, the heterogeneous geological blocks between the basin bottom and the upper crust layer were reconstructed using the reduced-rank procedure (Figure 19, Step 3, and Figure 20). The upper part of the crust was replaced with the HB (Figure 27). The origin of the HB was assumed to lie at the beginning of the Triassic sedimentation.

Several steps were used to specify the HB. Firstly, each block's present-day lateral borders were defined from the pre-Jurassic geological map (Figure 25b) and linked to the profile (Figure 25a). (The full version of the maps is accessible online. See Ivanov et al. (2009); 'Map of Jurassic formations: P-42 (Khanty-Mansiysk)' (2009) and 'Map of Jurassic formations: P-43 (Surgut)' (2010)). Next, the material properties from Table 4 were assigned to each block and used as fixed input parameters.

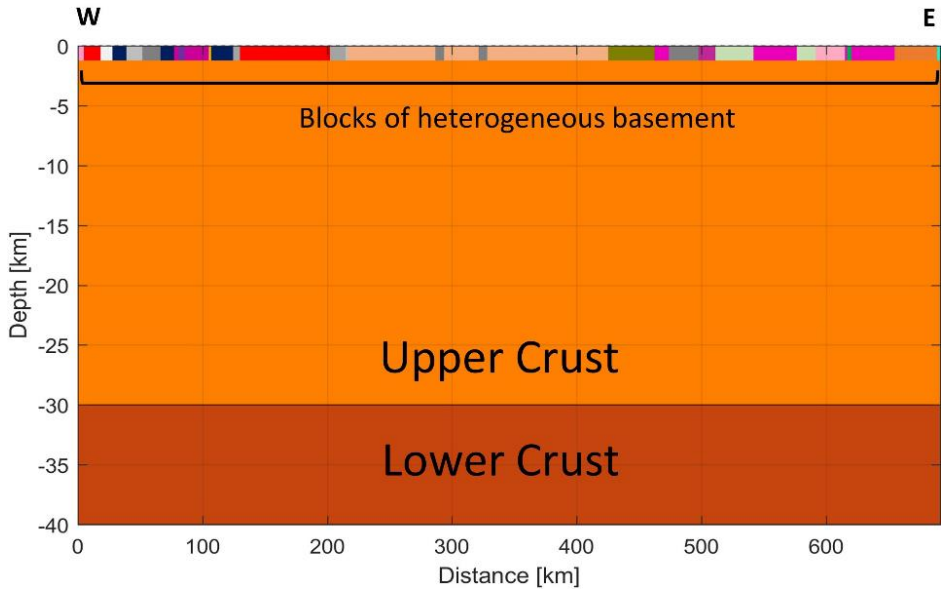

(a)

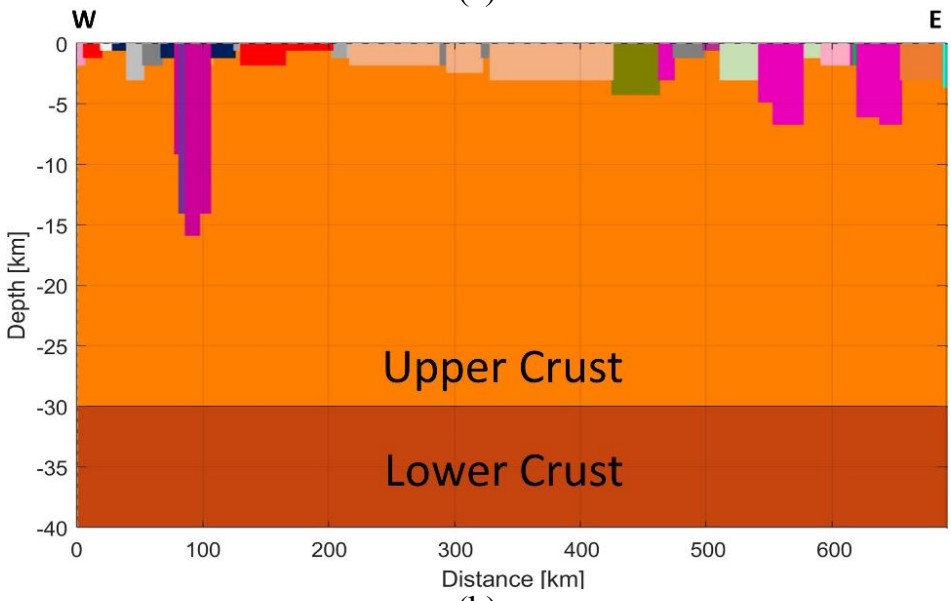

(b)

Figure 27. Initial state of the basin configuration before sedimentation at 251 Ma: (a) Model 2, with the preliminary assumption of the HB (Figure 25) being 1 km thick; (b) Model 2, with the thickness of the HB determined by gravity analysis. Coloured blocks correspond to the HB, with their assigned petrophysical properties coming from Table 4. For convenience, the lithospheric mantle layer is not shown here.

The thicknesses of the HB blocks were defined (Figure 26b and Figure 27b) by fitting gravity anomaly data (Figure 20). At the first itera-

tion, the HB's initial thickness (i.e., before the rifting extension) was approximated to 1 km (Figure 27a). The resulting geometry and densities of the blocks were reached when gravity fitting was performed after Condition (1) from Figure 20 was satisfied. For Model 2, the density values of Units 8 and 18 were manually adjusted: from 2870 and 2740 to 2840 and 2840 kg/m^3, respectively (Table 4), following Schön (2015, p. 116). However, the thermal properties remained unchanged. Those blocks with an igneous origin were split vertically into several sub-blocks in order to obtain a better fitting of the gravity anomaly and to estimate the maximal-possible impact of basement heterogeneity on thermal history reconstruction. The initial design of the Model 2 basement before the sedimentation started is shown in Figure 27b.

The uncertainty in the determined density of the blocks in the basement may affect the thickness of the reconstructed blocks, impacting the entire thermal regime reconstruction. We have only considered the uncertainty of density for igneous rocks, since they have a critical impact on the thermal history. We built Model 2: ρ_{min} and Model 2: ρ_{max} using the range of acceptable densities for igneous rocks taken from Schön (2015, p. 116) for Units 1, 2, 3, 4, 7, 8, 15, 16, 18 and 19 (Table 4). The basement geometry was obtained following the reduced-rank procedure in Figure 20; only the thicknesses of the heterogeneous blocks were varied, while the maximum and minimum acceptable density values were fixed (marked by ^{C} in Table 4). The thermal conductivity values were fixed.

Calibration of Model 2, Model 2: ρ_{min} and Model 2: ρ_{max}

While the calculated gravity anomaly fits the observed patterns for Model 2 where $\sigma_m = 4.7$, for Model 2: ρ_{min} where $\sigma_m = 5.8$ and for Model 2: ρ_{max} where $\sigma_m = 5.5$, slight discrepancies were still visible in some intervals (Figure 23). Hidden bodies beneath the basement surface, the large-scale gravity survey's low sensitivity to small bodies and/or the effect of density anomalies outside the studied 2D object could explain these discrepancies.

After the Bouguer anomaly was fitted, the remaining calibration parameters were rechecked:

- The stratigraphy section, porosity and pressure profiles remained unchanged.

- The Moho depth stayed almost unchanged (Figure 22). A negligible difference with respect to Model 1 was observed only in rift graben zones.
- The thermal regime was refined by the e-fold length parameter, which was set to 21 km. In contrast with Model 1, e-fold length values for models with an HB were set at 21 km. The difference was explained by decreased radiogenic heat production and decreased thermal conductivity in the HB. The calibration results were satisfactory (Figure 24); as such, the optimisation of thermal conductivity values in the model (Figure 19, Step 4) was not necessary.

The final modelled geological section in Model 2 is shown in Figure 26b, while those in Model 2: ρ_{min} and Model 2: ρ_{max} are shown in Figure 28.

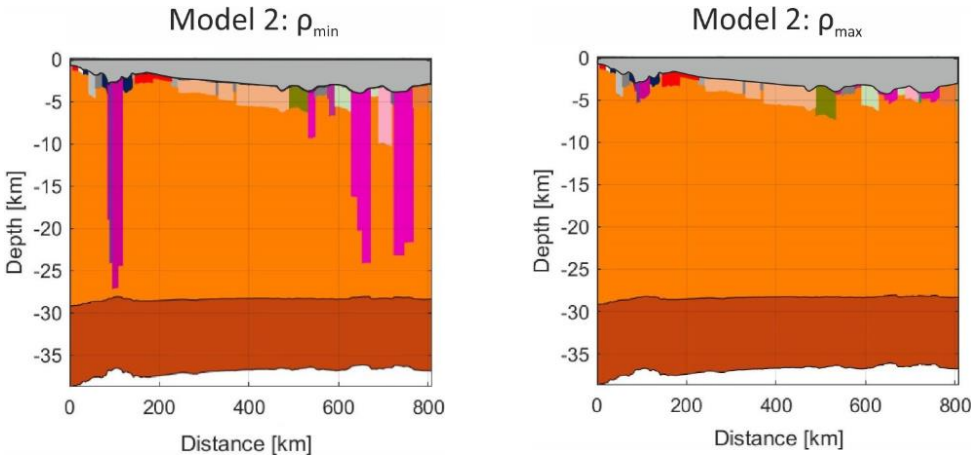

(a) (b)

Figure 28. Reconstructed present-day upper part of the basement design for Model 2: ρ_{min} (a) and Model 2: ρ_{max} (b). The grey area is the basin section. The colour codes beneath the basin section correspond to those of the basement units presented in Table 4. For convenience, the lithospheric mantle layer is not shown in this figure.

4.2.2 Results and discussion

According to the calibration of results by the Moho boundary depth (Figure 22), porosity and pressure, present-day temperatures and vitrinite reflectance (Figure 24), we concluded that all the models (Model 1, Model

2, Model 2: ρ_{min} and Model 2: ρ_{max}) were acceptable. However, the additional calibration using gravity data showed that Model 1 does not provide reliable results (Figure 23). We can explain it by the simplifying assumption made during the construction of this model.

Model 1 vs Model 2

Thicknesses of basement heterogeneity blocks

The present-day reconstructed basement in Model 2 is presented in Figure 26b. Deep-rooted and vertically elongated bodies of magmatic origin are clearly visible in the reconstructed geological section of the basement, beneath the rifted zones (coloured violet in Figure 26b). We associated their origin with the latest Palaeozoic to Early-Mesozoic global plate boundary and plate kinematics reorganisation (Nikishin et al., 2002)'. Thus, the magmatic bodies originate from voluminous intracontinental flood basalts. Earlier evidence of deep-rooted magmatic bodies in rift zones is mentioned in Blackbourn (2014), Braitenberg and Ebbing (2009) and Nezhdanov et al. (2014).

The basement geometry is in good agreement with studies by Braitenberg and Ebbing (2009), who estimated the thickness of intrusive igneous rocks based on gravity and magnetic anomalies up to 5 km beneath the eastern rift graben area, at around 620–690 km and 720–750 km of the profile intervals. The thickness of the pre-Triassic paleobasin is in accordance with the interpretation of the seismically derived bottom of the neighbouring regional seismic profile (Stoupakova et al., 2015). The thickness of the paleobasin outside rift graben zones increases as it goes eastward, growing from less than 1 km to ~3.5 km (Stoupakova et al., 2015). The modelled heterogeneous blocks' thicknesses match the minimal thickness of the blocks determined by drilling in adjacent territories ('Map of Jurassic formations: P-42 (Khanty-Mansiysk)', 2009; 'Map of Jurassic formations: P-43 (Surgut)'; 2010). In the 256–574 km profile interval, the thicknesses of Units 11, 12 and 13 were more than 66, 250 and 1226 m, respectively ('Map of Jurassic formations: P-42 (Khanty-Mansiysk)', 2009). In the 574–808 km profile interval, the thicknesses of Units 13, 15, 17, 18, 20 and 21 were more than 320, 1500, 500, 200, 380 and 100 m, respectively ('Map of Jurassic formations: P-43 (Surgut)', 2010).

Basement densities

An additional analysis of the Bouguer anomaly (Figure 23) emphasised the significant underestimation of density heterogeneity within the basement in Model 1 (Figure 29a), compared with the estimation given in Model 2 (Figure 29b). A distinct difference was observed beneath the rift graben zones. The granites in the upper crust of Model 1 were less dense than mafic or ultramafic rocks formed during mega-rifting. The difference in the basement density distribution between Model 1 and Model 2 resulted in an insignificant change to the Moho boundary position of up to 450 m. Thus, the weight of the vertical columns of the crust and the lithospheric mantle had a negligible effect on the isostatic compensation (Figure 22). We estimated, using the Model 1 dataset, that heat flow values are changed by less than 2% when the Moho boundary moves up to 450 m in the same 110 km total lithospheric thickness. The 450 m difference in the Moho depth between Model 1 and Model 2 was negligible, since the variations in Moho boundaries defined in Braitenberg and Ebbing (2009) and Cherepanova et al. (2013) were more than 5 km.

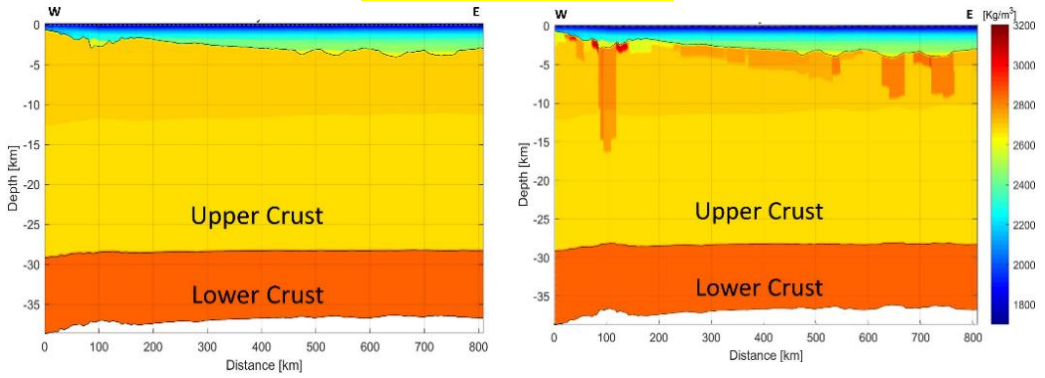

(a) (b)

Figure 29. Present-day distribution of bulk density in the crust and basin domains: (a) Model 1 and (b) Model 2. The density colour code applies to both images. For convenience, the lithospheric mantle layer is not shown in this figure.

The density distribution in the model by Isaev (2008), which was obtained for a sub-parallel 350 km–long seismic profile located about 100 km north of our model, demonstrated a similar lateral increase in density up to 150–300 kg/m^3 beneath the rift structure in its western part (around 80–120 km of the profile interval).

Thermal regime

In Model 2, a heterogeneous distribution of thermal conductivity and radiogenic heat production within the basement was obtained by fitting the gravity data (Figure 30 a–d). Generally, effective thermal conductivity and radiogenic heat production are lower in the HB domain because the substituted upper crust unit has a higher thermal conductivity and radiogenic heat production (Table 4) than the HB's igneous and sedimentary rocks.

As a result, in Model 2, the value of radiogenic heat production in the crust increased by increasing the e-fold parameter, from 20.4 to 21 km, in order to compensate for the difference in the basal heat flow in the well's thermal calibration points. The most significant divergence between the results in Model 1 and Model 2 was observed beneath the rift graben zones in the so-called magmatic roots, where thermal wellbore calibration was absent. In this area, in Model 2, the bulk thermal conductivity and radiogenic heat production were 2.0–2.2 W/m/K and 1 $\mu W/m^3$, respectively, while in Model 1, they were 2.2–2.7 W/m/K and 1–2 $\mu W/m^3$, respectively. The difference between the magmatic roots' thermal properties and the crustal layer led to anomalies in the temporal variations in the basal heat flow (Figure 30 e and f).

In Model 2, the present-day heat flow values in the rift graben zones of the Vartov High (the eastern graben on the profile) are 5 mW/m^2 lower relative to the surrounding areas (Figure 30f), which is entirely consistent with Kurchikov's (2001) geothermal study. Figure 31a shows the difference in the basal heat flow caused by the basement's thermal properties as a function of time for Models 1 and 2. The time-averaged difference in heat flow (Figure 31b) is predominantly positive, since HB blocks have lower thermal conductivity and radiogenic heat production values than do the corresponding values for the crust (Figure 31). The maximum mean value of the difference corresponds to the rift graben zones, reaching10.2 mW/m^2 in the deepest HB units in this location (Figure 31b). Unit 16 (578–590 km of the profile) had the lowest negative values of difference (down to −1.5 mW/m^2), since this unit has a higher thermal conductivity than the crust. All the other negative values occurred due to increased radiogenic heat production, impacted by the e-fold length parameter for the crust's radioactivity in Model 2 during its thermal calibration.

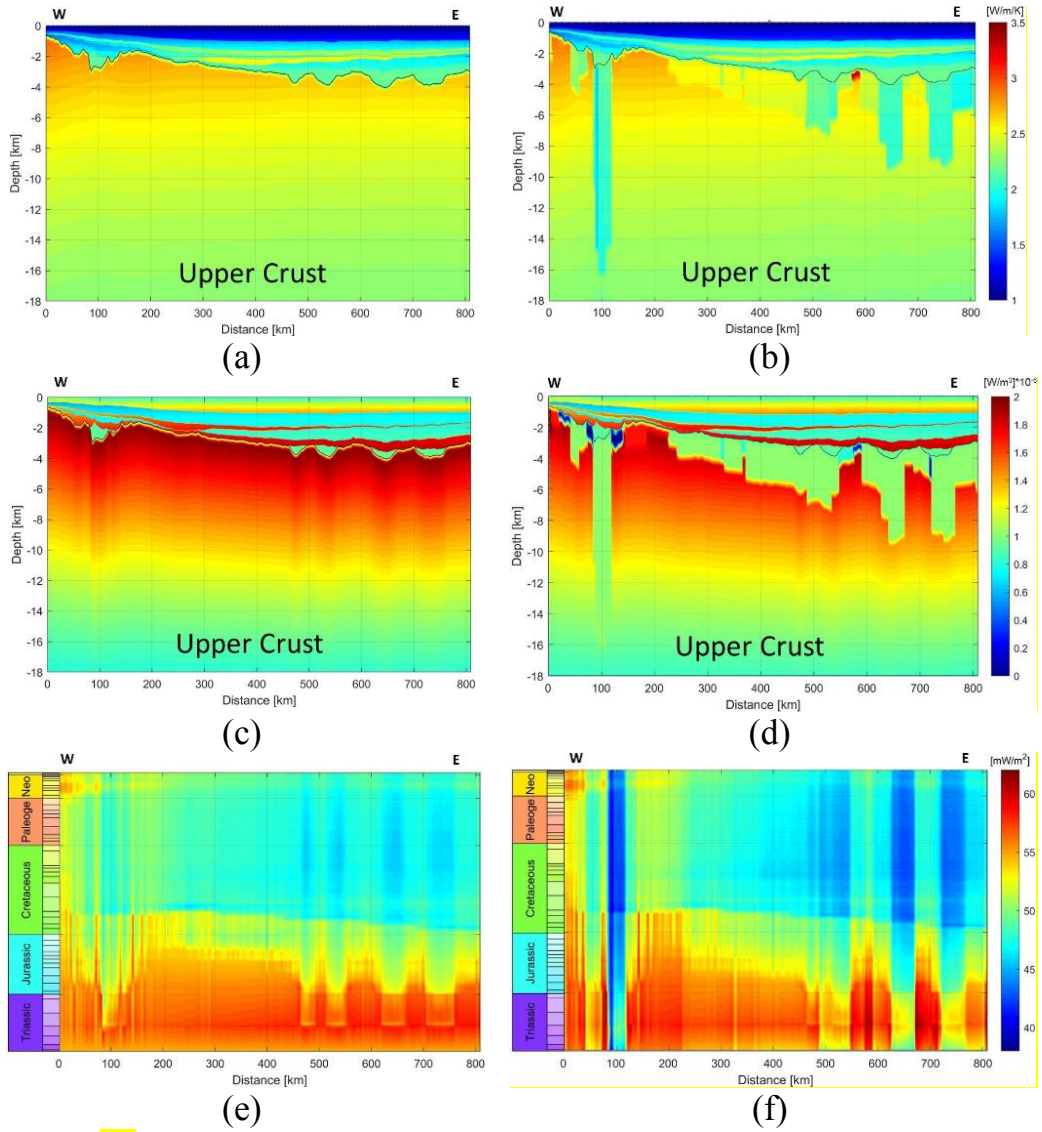

Figure 30. Present-day effective thermal conductivity distribution: (a) Model 1 and (b) Model 2. Present-day radiogenic heat production: (c) Model 1 and (d) Model 2. Heat flow histories of the basement surface: (e) Model 1 and (f) Model 2 (the density colour code applies to both images).

Since the primary source rock in the Western Siberian Basin is the Bazhenov Fm, it is necessary to evaluate the impact of basal heat flow changes on its present-day temperatures and vitrinite reflectance distribution (the red and blue lines in Figure 32 a and b). Discrepancies were observed between Model 1 and Model 2's estimations of present-day temperature and vitrinite reflectance in the Bazhenov Fm surface in areas with insufficient well coverage.

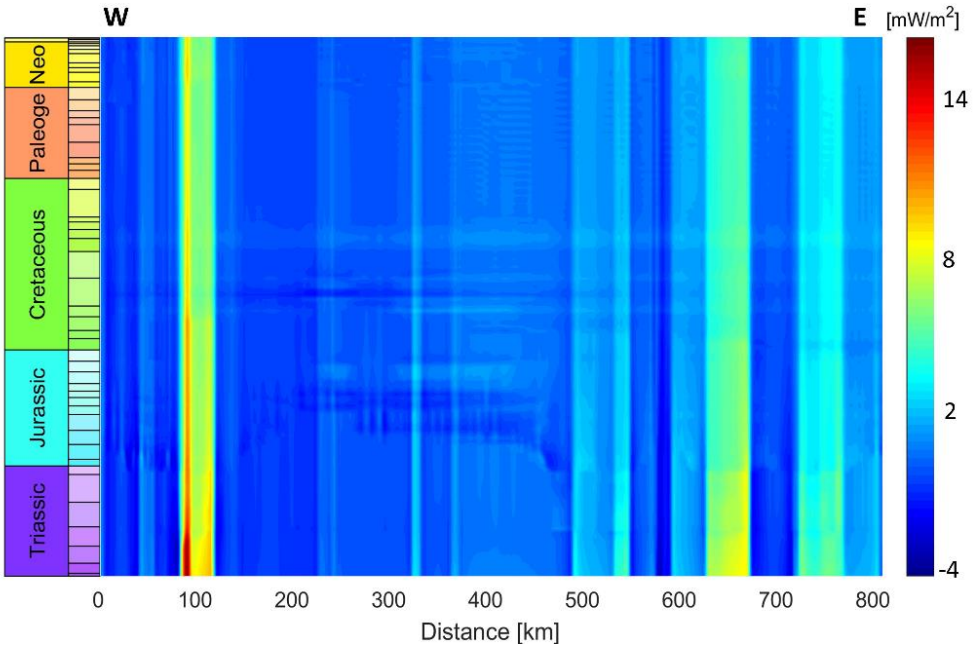

(a)

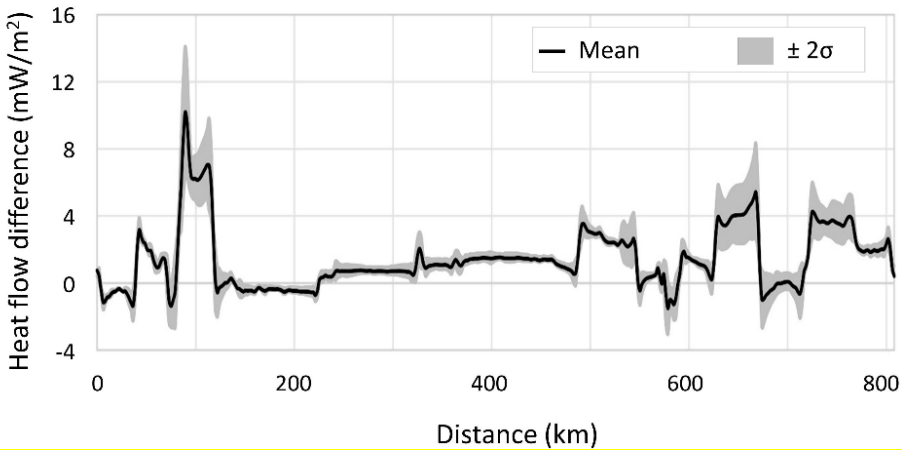

(b)

Figure 31. (a) Differences in the spatio-temporal variations of calculated basal heat flow in Model 1 and Model 2 (values of plot = values of Model 1 − values of Model 2) as a function of distance from the west end of the profile; (b) where ±2σ denotes a two-standard-deviation interval around the mean value.

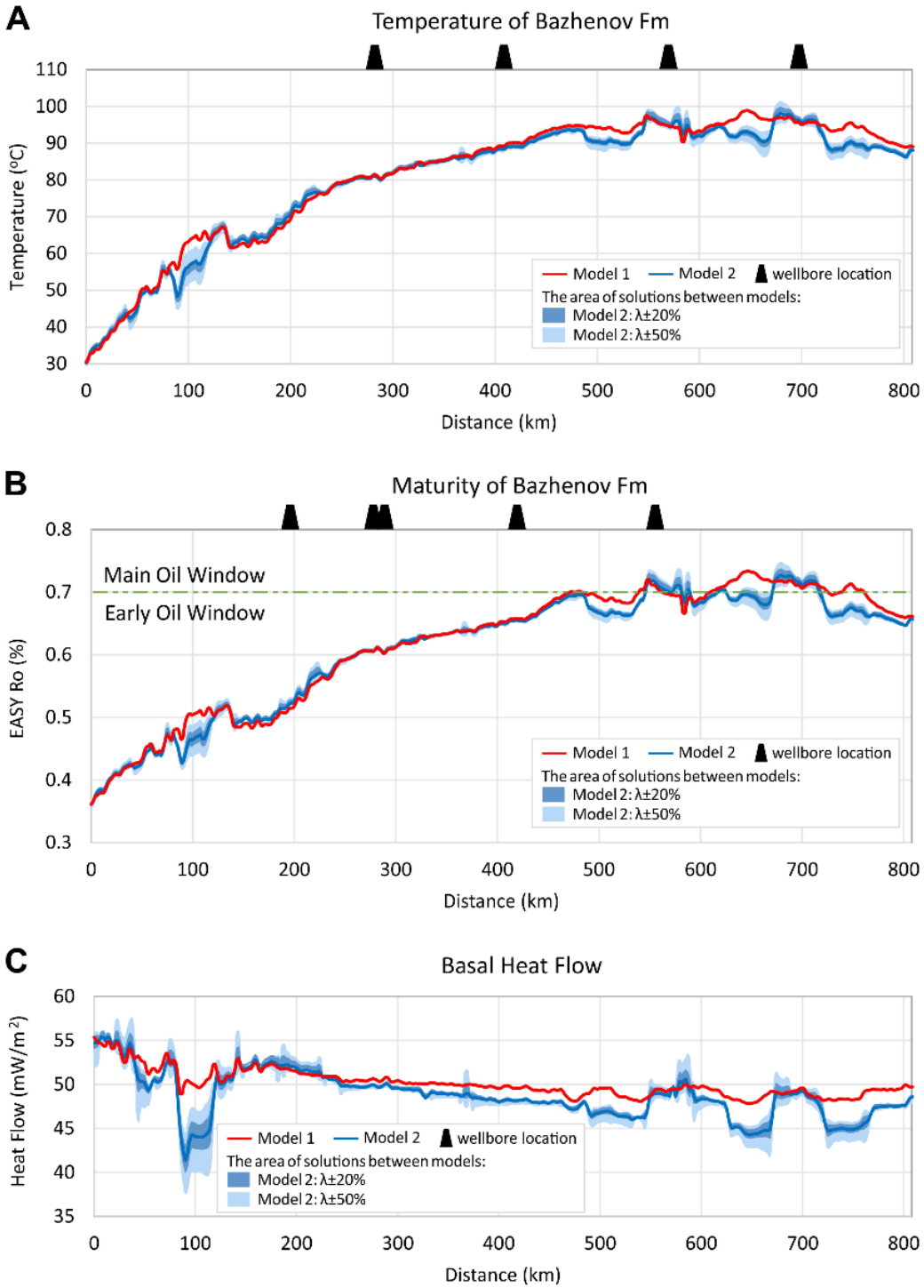

Figure 32. Calculated present-day (A) temperatures and (B) vitrinite reflectance using the EasyRo model (Sweeney and Burnham, 1990) of the Bazhenov Fm surface, and (C) the basal heat flow for the investigated models.

Such discrepancies are associated with the rift graben zones (four segments along the profile with a total length of 210 km), where Model 1 provides temperatures and vitrinite reflectance that are higher than those in Model 2 by up to ~9 °C and 0.05 %Ro, respectively. The essential feature of this discrepancy is that Model 1 predicts the main oil window along 75 km of the profile, while Model 2 predicts the early oil window (Figure 32b) according to the definition given by Tissot and Welte (1984), where boundary value between the early oil window and main oil window is defined by 0.7 %Ro.

Such a difference between the two predictions may lead to a significant divergence in petroleum system evaluation and may result in errors in the estimated mass generation of hydrocarbons, the critical moment, reservoir volumes (for 3D modelling) and other important parameters. The remaining discrepancies in the estimations of temperature and vitrinite reflectance profiles do not exceed 2 °C and 0.02 %Ro, respectively, and so are less than the uncertainty in the calibration values.

Model 2: ρ_{min} and Model 2: ρ_{max}

The results in Model 2: ρ_{max} regarding the thermal regime are similar to those in Model 1 (Figure 33). The thin HB (which has a thickness of up to 1.8 km) explains the similarity in temperature (Figure 33a) and maturity (Figure 33b) beneath the rift graben zones. The discrepancy between the models was only observed in the profile zone from 490 to 540 km, which is explained by the presence of the thick paleobasin block with lower thermal conductivity (2.4 vs 3.0 W/m/K) and radioactive heat production (1 vs 2 $\mu W/m^3$) in the Model 2: ρ_{max} HB (compared to Model 1's crystalline basement).

Model 2: ρ_{min} demonstrates the lowest limit of the thermal regime governed by the thick HB beneath the rift graben zones (up to 27 km), since its blocks show lower thermal property values than those found in Model 1. The differences between Model 2: ρ_{max} and Model 2: ρ_{min} in the temperature and maturity of the Bazhenov Fm surface reach 9 °C and 0.06 %Ro, respectively, while the difference in the basal heat flow is 5 mW/m^2 (Figure 33).

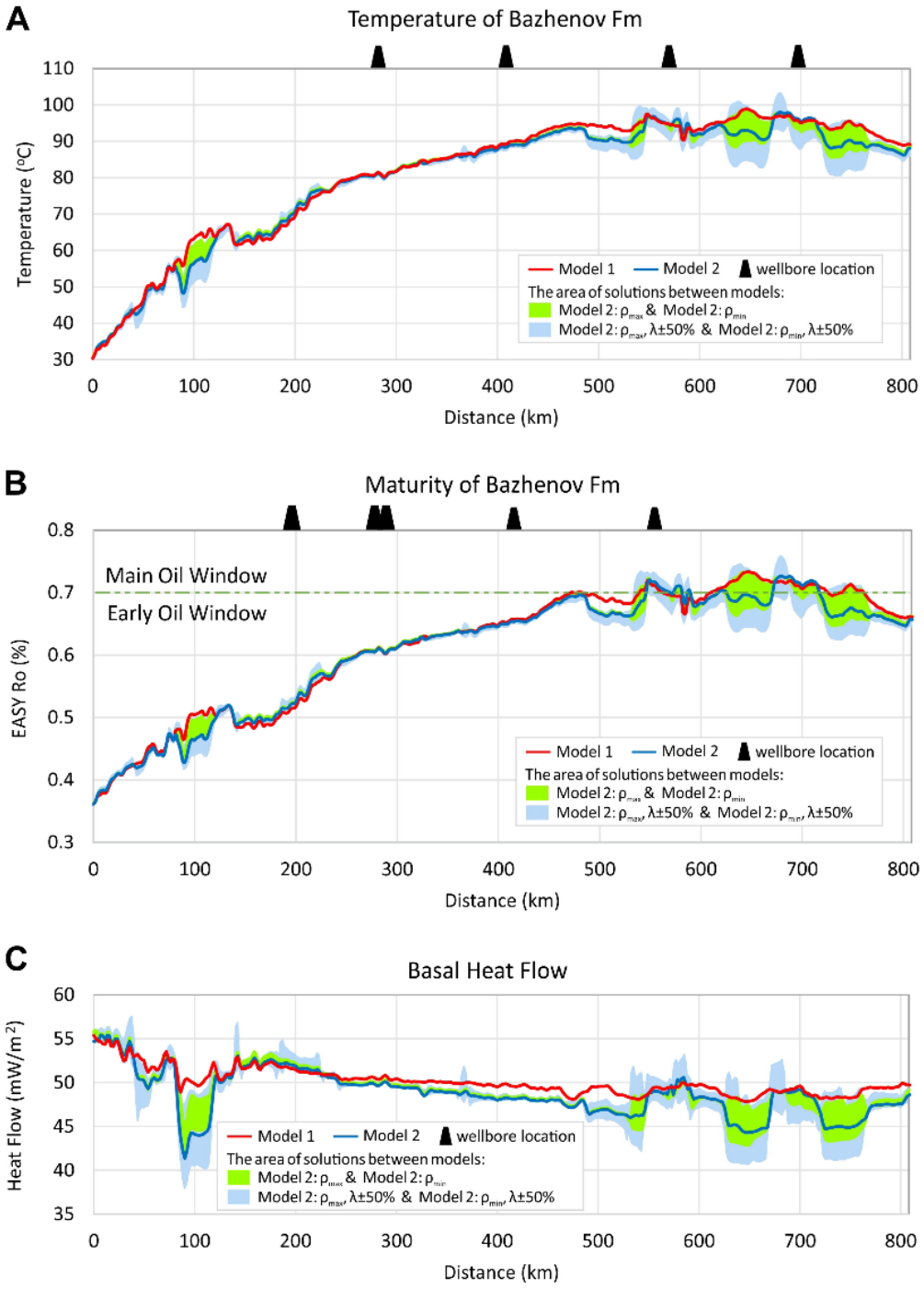

Figure 33. Calculated present-day (A) temperatures and (B) vitrinite reflectance using the EasyRo model (Sweeney and Burnham, 1990) of the Bazhenov Fm surface, and (C) basal heat flows for Models 1 and 2. The lower edge of the blue infill corresponds to Model 2: ρ_{min}.

The spread between Model 2: ρ_{min} and Model 2: ρ_{max} in terms of the temperatures and the vitrinite reflectance on the Bazhenov Fm surface

increases with time, while the corresponding residual basal heat flow decreases with time (Figure 34). At the profile location, at 645 km, the spread of temperature increases from 0 to 9 °C (Figure 34a), while vitrinite reflectance increases from 0 to 0.06 %Ro (Figure 34b). Residual basal heat flow decreases from 8 to 4.5 mW/m^2 (Figure 34c), which can be explained by the blanketing effect (Lucazeau and Le Douaran, 1985; Wangen, 1995).

Model 2: ρ_{max} and Model 2: ρ_{min} make it possible to determine the range of HB geometry and to quantify its impact on the modelled thermal regime. Such estimates are particularly relevant in rift graben zones, where the resolution of the available seismic surveys is not detailed enough for us to distinguish certain structural features.

Analysis of thermal conductivity uncertainties in a heterogeneous basement

A sensitivity analysis of thermal conductivity was conducted for all models with an HB. The analysis involved systematic changes in the matrix thermal conductivity (λ) relative to the values from Table 4 in the ±20% and ±50% range.

Model 2 includes a study of the uncertainty in the ±20% and ±50% range; the modelling results are referred to as Model 2: λ±20% and Model 2: λ±50%, respectively. In Model 2: ρ_{min} and Model 2: ρ_{max}, the study of uncertainty considers only the ±50% range; the models in this case are referred to as Model 2: ρ_{min}, λ±50% and Model 2: ρ_{max}, λ±50%, respectively.

The results of thermal conductivity uncertainties that impact present-day basal heat flow, surface temperature and the vitrinite reflectance of the Bazhenov Fm are presented in Figure 33 and Figure 34. The matrix thermal conductivity of the crust and the lithospheric mantle remains unchanged. The difference in thermal conductivity values in Model 2: λ±20% relative to Model 2 is equivalent to minor changes in the basal heat flow of up to ±1.6 mW/m^2 (around 4%), which corresponds to changes in temperature and vitrinite reflectance values of ±0.9 °C and ±0.01 %Ro, respectively.

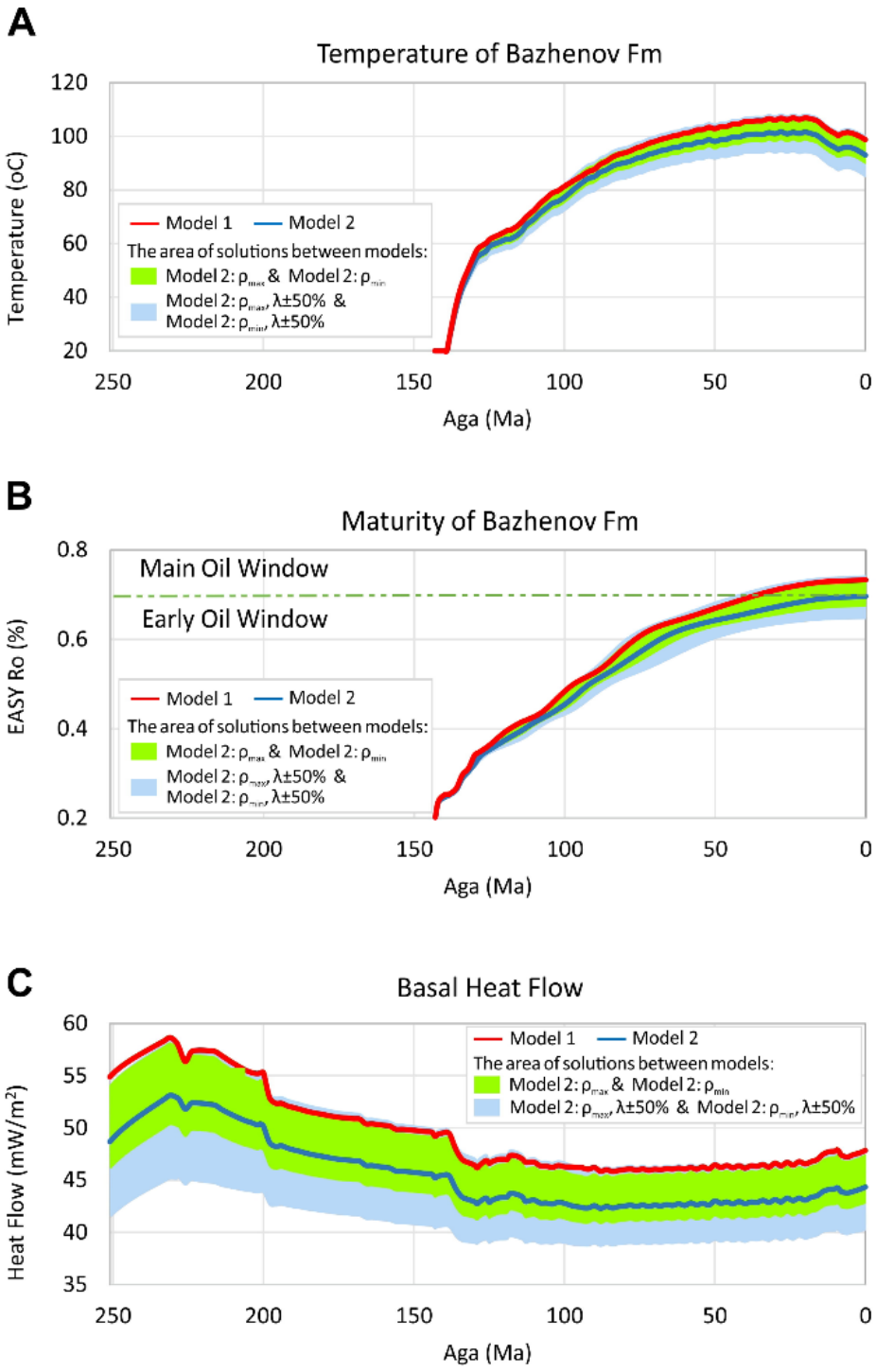

Figure 34. Extraction of the time-dependent (A) temperatures and (B) vitrinite reflectance using the EasyRo model (Sweeney and Burnham, 1990) of the Bazhenov Fm surface, and (C) the basal heat flow in the 645 km section for all models. The lower boundary of the blue infill corresponds to Model 2: ρ_{min}.

The difference in the thermal conductivity values found in Model 2: λ±50% relative to those shown in Model 2 results in a difference in the basal heat flow of up to ±4.8 mW/m^2 (around 11%), a difference in temperature of up to ±5 °C and a difference in vitrinite reflectance of up to 0.03 %Ro, which can lead to erroneous estimates of the organic matter's maturity rank in some of the profile intervals (e.g., 468–485, 577–587 and 644–654 km). These values may increase with the thickness of the igneous rock.

One additional study for Model 2 was conducted with the purpose of estimating the effect of possible errors in the matrix thermal conductivity of Units 8 and 16 (Table 4). Taking λ = 3.0 W/m/K in Unit 8 (instead of 1.8 W/m/K) leads to an insignificant increase in %Ro of up to 0.01 %Ro and an increase in temperature of up to 3 °C on the Bazhenov Fm surface. Taking λ = 2.1 W/m/K in unit 16 (instead of 4.1 W/m/K) leads to a decrease in %Ro of around 0.01 %Ro and a decrease in temperature of around 3 °C in the corresponding area of the Bazhenov Fm surface.

The estimations of the impact of thermal conductivity uncertainties on thermal history reconstruction for Model 2: ρ_{min}, λ±50% and Model 2: ρ_{max}, λ±50% are presented in Figure 33 and Figure 34. Figure 33 shows the present-day combined sensitivity models' range of estimations for the surface temperature and vitrinite reflectance of the Bazhenov Fm and for basal heat flow. The maximum estimates of the effect of the HB on thermal and source-rock maturity models were obtained in the eastern rift graben zones. The upper edge of the thermal solution range generally coincides with the estimates found in Model 1, except for in extensive intervals of 182–220, 535–592, 630–650, 672–678 and 720–750 km. In these intervals, the maximum overestimations in temperature, vitrinite reflectance and basal heat flow values relative to Model 1 reach 6 °C, 0.28 %Ro and 2.5 mW/m^2, respectively. However, these differences do not affect estimations of the organic matter's maturity rank. Conversely, the lower edge of the thermal solution range gives significantly underestimated values relative to those in Model 1, particularly in the extended intervals of 88–113 and 490–808 km. In these intervals, the maximum underestimation of temperature, vitrinite reflectance and basal heat flow values relative to Model 1 reach 12 °C, 0.1 %Ro and 6 mW/m^2, respectively. Following the lower

edge of the thermal solution range, we observed the early oil window maturity rank, instead of the main oil window of the Bazhenov Fm surface, for the 610–725 km and 745–757 km profile intervals (a total of 127 km). The spread variation over time on the Bazhenov Fm surface increases between the lower and upper edges of the thermal solutions in terms of temperature (Figure 34a) and vitrinite reflectance (Figure 34b), while the difference in basal heat flow decreases (Figure 14c). At the 645th km of the profile, the spread of temperature increases from 0 to 15 °C (Figure 34a), while vitrinite reflectance increases from 0 to 0.09 %Ro (Figure 34b). The difference in basal heat flow decreases from 13 to 8 mW/m^2 (Figure 34c). The difference in the basal heat flow decrease is also explained by the blanketing effect, being the difference between Model 2: ρ_{max} and Model 2: ρ_{min}.

Summary of the express estimation

We constructed and analysed a set of models with two different assumptions, that is, with and without the HB beneath the basin bottom, before determining the express estimation of the impact of the HB on thermal and maturity modelling results. These models, which have different HB geometries, combined with uncertainty studies in thermal conductivities, demonstrate the significant impact that contrasting thermal properties have on thermal and maturity models in rift graben zones. The reconstructed Model 2 is in accordance with other available investigations. A comparison of Model 2 and Model 1 demonstrates that the latter can overestimate the maturity rank of the Bazhenov Fm surface along 75 km of the profile, viewing it as the main oil window instead of the early oil window.

Models containing estimations of the minimum and maximum densities of the HB offer more extended estimations of the possible impact of an HB on the thermal history of the basin compared to Model 2 estimations. The upper edge of the thermal solution range containing the HB almost coincides with the solution that does not contain the assumption of an HB (Model 1). However, the lower edge of the thermal solution range exceeds the temperature and vitrinite reflectance estimates in the Bazhenov Fm within rift graben zones, relative to Model 2, by up to 3 °C and 0.02 Ro%, respectively.

Models providing different estimations of thermal conductivity uncertainties in the HB make it possible to determine the ultimate range of

modelled thermal histories. As a result, the maturity rank of the main source rock can be underestimated as the early oil window instead of the main oil window along 127 km of the profile; that is, along 16% of the total profile length and ~75% of the profile length where the main oil window was forecast in Model 1.

4.2.3 Conclusions

Section 4.2 has presented an application of the method for the express estimation of the impact of basement heterogeneity on thermal history and petroleum system modelling.

Reduced-rank inversion (added as an extension to the classic basin modelling workflow) provided a rough model of deep-rooted bodies and the remnants of the pre-Triassic basin; this is otherwise impossible to create, as seismic data at the basement's domain cannot be distinguished in seismic models (Cherepanova et al., 2013). We believe that the introduction of magmatic bodies in the model of rift graben zones could significantly change thermal history reconstructions of the basin and forecast petroleum system maturity. The reason for this is the contrast in the thermal properties of the upper crust and magmatic bodies.

The commonly used simplified assumption of the homogeneous crystalline basement, instead of the complex HB beneath the Jurassic strata, may lead to erroneous predictions regarding the maturity of the Bazhenov Fm, primarily in the rift graben zones.

The reconstructed basement geometry and properties of Model 2 in the eastern part of the profile agree with the results of other investigations: the depth of intrusive roots reaches 5 km (Braitenberg and Ebbing, 2009); the thickness of the pre-Triassic sedimentary paleobasin remnants increases eastwards up to 3.5 km (Stoupakova et al., 2015); and the negative anomaly of the heat flow amounts to –5 mW/m^2 (Kurchikov, 2001). The basal heat flow correction leads us to revise the maturity rank of the Bazhenov source rock, except for west of the rift graben zones from the main oil window to the early oil window, at three segments along the total length of 75 km of the profile. In any case, the area west of the rift graben zones is presumed to be immature.

When considering the uncertainty in density and thermal properties, the range of possible thermal solutions in the rift graben zones is extensive. The uncertainties found in basement densities form uncertainties in the temperature and vitrinite reflectance models of the Bazhenov Fm of up to 9 °C and 0.06 %Ro, respectively, relative to the model that does not contain an HB. The ±50% uncertainties in the basements' thermal conductivities in Model 2 lead to uncertainties in estimations of temperature and vitrinite reflectance of up to ±5 °C and 0.03 %Ro, respectively. Therefore, the maturity rank of the Bazhenov Fm can be overestimated as residing in the main oil window, instead of the early oil window, along 127 km of the profile.

A full-rank 3D model of the Western Siberian Basin that accounts for the geometry and properties of the basement in the rift graben zones should therefore be constructed. Constructing such a model would require the planning of additional geophysical studies such as deep seismic sounding, the building of seismic models, analysis of gravity and magnetic anomalies and measurement of the density and thermal properties of the rocks. Otherwise, the uncertainty range for the temperature and vitrinite reflectance of the Bazhenov Fm surface may reach 12 °C and 0.1 %Ro, respectively.

4.3 A case study of the Okhotsk Sea Basin

The results, discussions, and conclusions of the case study of the Okhotsk Sea Basin are presented in Peshkov et al. (2019). Due to the lack of studies related to the Okhotsk Sea Basin, compared to research into the West Siberian Basin, it is impossible to apply the workflow presented in Section 4.1, although the basement could be heterogeneous.

Profile common depth point (CDP) 1632 was chosen (Figure 35 and Figure 36), since it crosses the whole Okhotsk Sea Basin and has both gravity data and interpreted seismotomography data regarding the crustal and mantle strata. Even so, the information about the lithology of and thermal regime along the profile is weak because of sparse and shallow well-drilling. Detailed information about the study area is presented in Konstantinovskaya (2004), Krovushkina (2001), Lomtev et al. (2009) and Verzhbitsky et al. (2006).

4.3.1 Model construction

The 2D model constructed here is based on open-source data published in different papers (see below). The model's construction follows the typical workflow presented in Al-Hajeri et al. (2009), Hantschel and Kauerauf (2009) and Peters et al. (2017), adapted to account for forward modelling. The initial thicknesses, at 65.5 Ma, of the upper crust, lower crust, and upper mantle are determined according to Konstantinovskaya (2004) and Petrishchevsky (2016) to be 15 km, 20 km and 80 km, respectively. The duration of the riftogenesis is determined to have been from 65.5 to 23 Ma (Krovushkina, 2001), and the profile's stratigraphy is taken from the interpretation of seismic reflections by Lomtev et al. (2009). The description of lithological units (Figure 38) at an interval of 0–90 km is taken according to Krovushkina (2001). The characteristics of the remaining profile (90–1100 km) are assumed to be the same, since there are no wells available to describe the lithology. Each layer's petrophysical properties are obtained from Hantschel and Kauerauf's (2009) petrophysical database (Table 5). The correction of thermal conductivity by temperature is based on Sekiguchi's (1984) model. The measurements of the thermal material properties are absent.

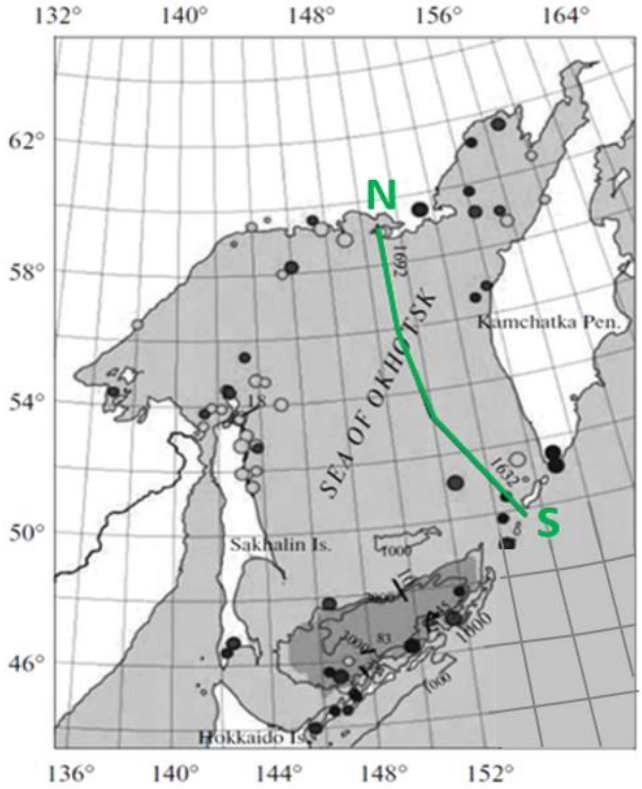

Figure 35. Location of the study profile, edited after Tikhonov and Lomtev (2015).

Table 5. Material properties of the lithology units according to descriptions from Krovushkina (2001); the used colour codes correspond to Figure 38.

Colour	Age of lithology	Physical properties*						
		ρ (kg/m^3)	α (K^{-1}·10^{-5})	A (μW/m^3)	C_ρ (J/kg/K)	λ (W/m/K)	φ_0	B (km)
	65.5-50	2656	3.3	1	870	2.62	0.46	0.42
	50-33.9	2715	3.3	1	860	2.74	0.43	0.38
	33.9-28.4	2665	3.3	1	870	2.24	0.48	0.46
	28.4-15.97	2706	3.3	2	880	1.75	0.66	0.73
	15.97-11.61	2820	3.3	1	830	1.95	0.49	0.58
	11.61-5	2356	3.3	1	860	1.66	0.68	0.49
	5-0	2593	3.3	1	860	2.17	0.62	0.58

*Properties of rock matrix: ρ – density; α – thermal expansion; A – radiogenic heat production; C_ρ – specific heat capacity; λ – thermal conductivity; parameters of rock by Athy's (1930) low $\varphi(z)=\varphi_0 \exp^{z \cdot B}$: φ_0 – surface porosity; B – length scale factor, z – negative values of depth.

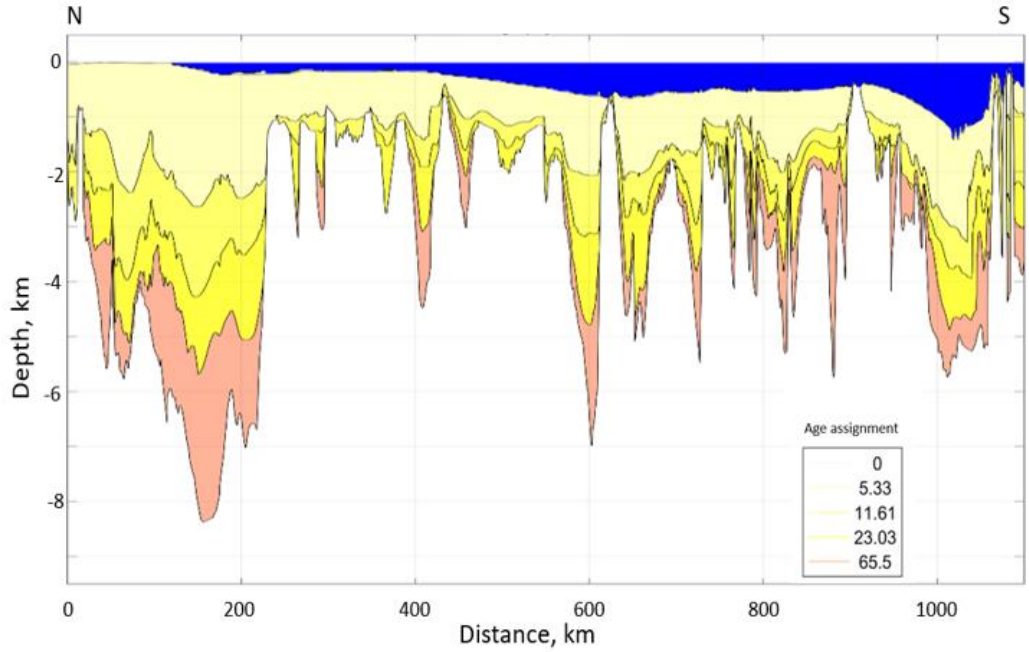

Figure 36. Stratigraphy of the study profile CDP 1632.

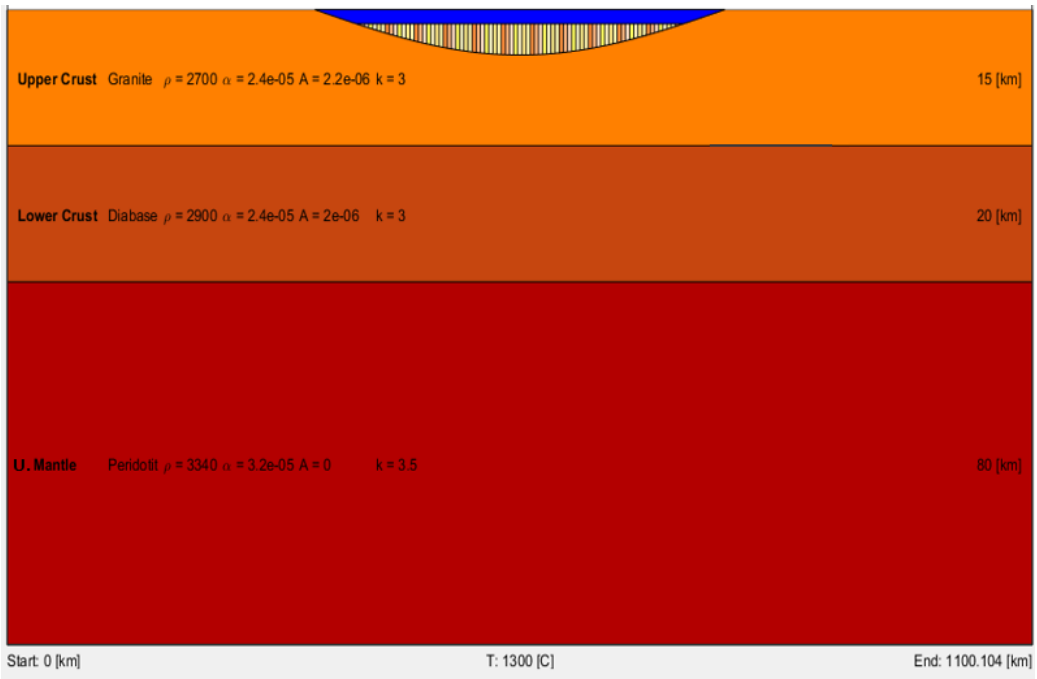

Figure 37. Initial condition of the following parameters of each lithospheric layer at 65.5 Ma: density (ρ), coefficient of thermal expansion (α), radiogenic heat production (A) and thermal conductivity (k).

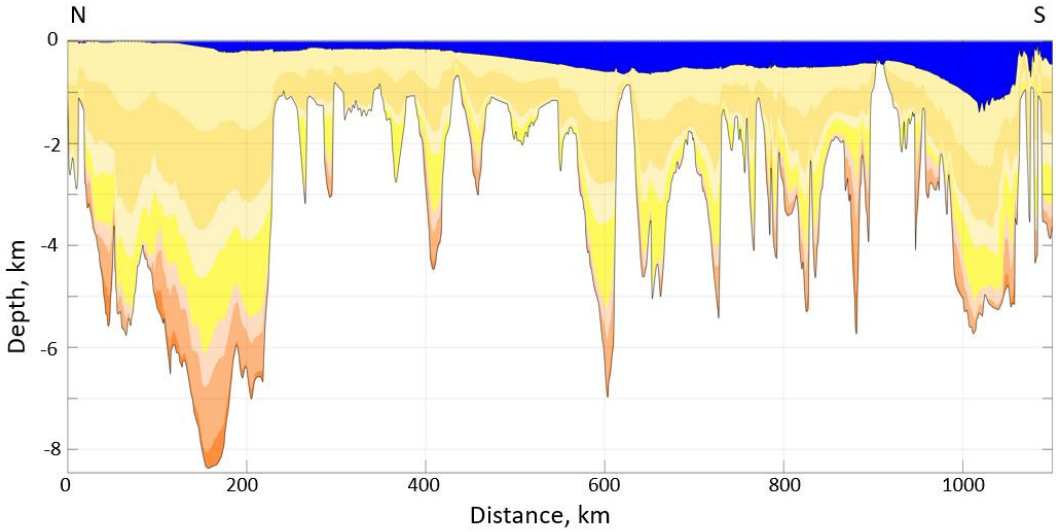

Figure 38. Basin infill architecture. Properties of the lithology units are described in Table 5.

The temperature boundary condition at the lithosphere bottom is set as 1300 °C according to Fischer et al. (2010). The paleoclimate parameters for the upper boundary condition are borrowed from the work of Galushkin et al. (2009).

4.3.2 Calibration

The porosity data calibration step is ignored because of a lack of data.

Assumptions of the Airy and flexural isostasy regimes are examined in this case study to find the best fit between the modelled and the observed stratigraphy sections. The flexural isostasy demonstrates the best fit with the following parameters: a necking level (NL) of NL = 5 km and elastic thickness (T_e) of T_e = 3 km (see details in Appendix A.1.2). The residual value of the stratigraphy sections' misfit is determined to be 5 % after 30 automated iterations of forward modelling.

The model contains two tectonic scenarios: first, to fit the free-air anomaly (since it is offshore) (Figure 39 a and c), and second, to fit the level of Moho (Figure 39 b and d) using seismotomography data (Figure 39e). The first scenario assumes only the lithosphere's extension during the rift phase and correctly reproduces the free-air gravity anomaly (Figure 39 a and c). However, the thickness of the crustal layers does not correspond to the seismic interpretation data (Figure 39e).

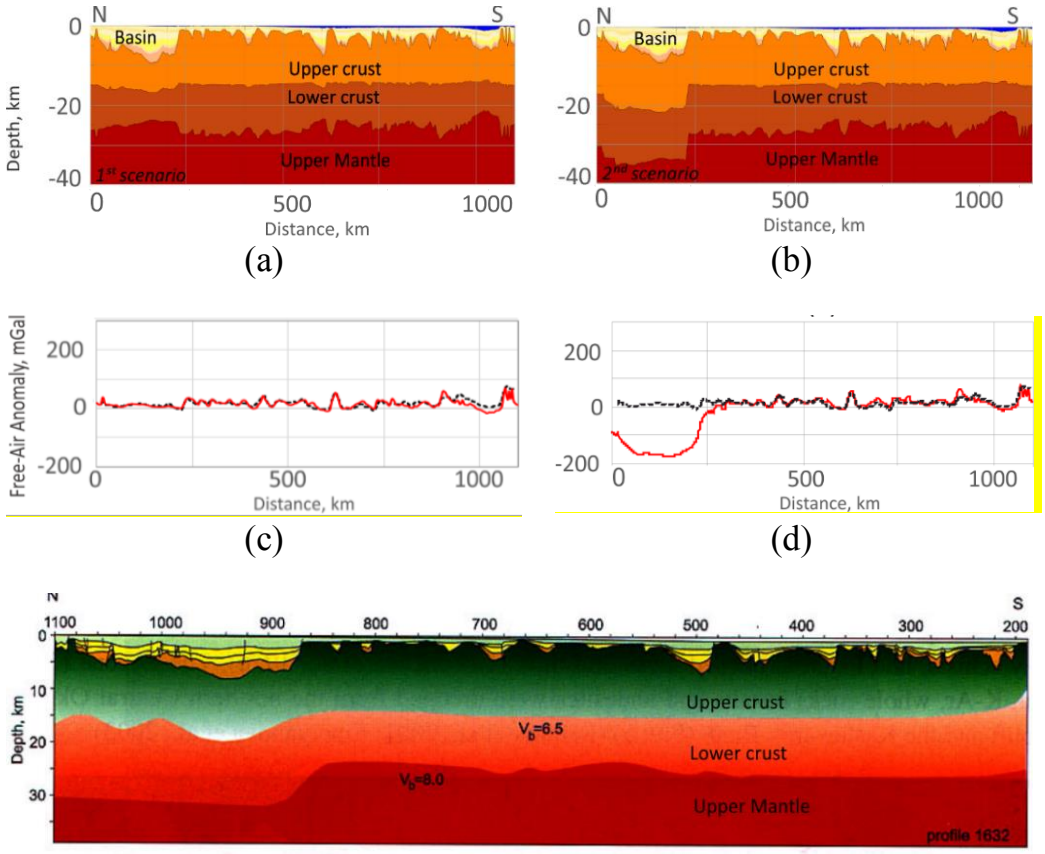

Figure 39. (a, c) – fitting the free-air gravity anomaly (first scenario); (b, d) – fitting Moho level defined from the seismic data (second scenario). (e) – basin's profile obtained from interpretation of seismotomography data Konstantinovskaya, (2004). Red and black lines in (c) and (d) are the modelled and measured gravity anomaly profiles, respectively (modified after Peshkov et al. (2019).

The second scenario limits the north side's stretching factors, with a profile interval of 0–230 km. An artificial load by weight is added to this part of the profile in order to complete the isostasy law. Thus, the second scenario is calibrated using interpreted seismotomography data (Figure 39 b and e), while the gravity anomaly calibration is ignored (Figure 39d). The reason for the gravity anomaly misfit is the deficit in the density in the vertical weight column.

Both scenarios are calibrated on temperature and vitrinite reflectance data (Figure 40) (Krovushkina, 2001). The satisfying calibration is

reached by tuning the radiogenic heat production in crustal layers using the e-fold length factor (Lachenbruch, 1970, 1968).

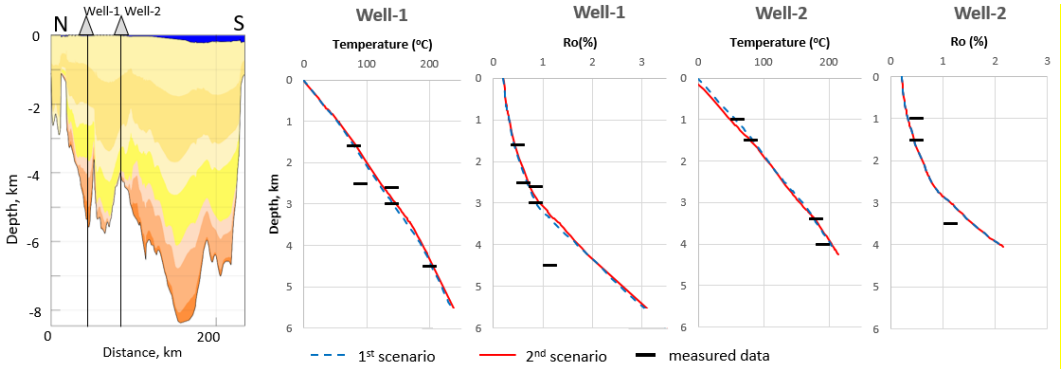

Figure 40. Results of model calibration for the considered tectonic scenarios using temperature and vitrinite reflectance (Ro) data in the Well-1 and Well-2 areas.

4.3.3 Results and discussion

This study does not aim to reconstruct a detailed thermal history; therefore, it does not consider a model wherein both seismic and gravity calibrations satisfy each other, although such a model may be reached by varying the basement density values in the 0–230 km profile interval, following the example set by Klitzke et al. (2015, 2016), Maystrenko et al. (2018), etc. Instead, models separately fitted to gravity and seismotomography data at the same time as with temperature and vitrinite reflectance data from the wells demonstrate the minimum and maximum (extremum) possible values in the basal heat flow range in the 230–1100 km profile interval.

The reason these two scenarios are considered to be extremum is explained by the fact that the lithosphere has the same total thickness in both scenarios. Thus, the different strata thicknesses in the two scenarios lead to a different balance of radiogenic heat production because of the partial replacement of the crustal rocks (granite and diabase) by mantle (peridotite) rocks in the first scenario and vice versa in the second scenario. Crustal and mantle types of rock have the extremum values for the radiogenic heat production – 2 $\mu W/m^3$ and 0 $\mu W/m^3$, respectively (Hantschel and Kauerauf, 2009). Thus, we compensate for this difference in heat production when fitting the thermal solution to both scenarios to the 0–230

km profile interval by varying the e-fold parameter responsible for radiogenic heat production. As a result, we obtain the extremum values of the radiogenic heat production, varied by the e-fold parameter for an all profile simultaneously, in the remaining 230–1100 km profile interval.

The absolute difference in the effective thermal conductivities for the crustal and mantle layers decreases with temperature. Therefore, for the typical crustal temperatures, the partial replacement of the mantle rock by the crustal component in the 0–230 km profile interval should not significantly impact the temperature evolution in the studied area.

The two modelled tectonic histories control the basal heat flow and basal temperature in the 0–230 km profile interval by sedimentation rate (Figure 41) in different ways. The peak discrepancy in sedimentation rate, basal heat flow and basal temperatures is found in the Eocene–Oligocene epochs, in the 120–200 km profile interval. However, the present-day thermal regime is almost identical for both scenarios (Figure 40). The maximum discrepancy at the point of the 150 km profile interval leads to a slight lag in the maturation of organic matter in 3 Ma. This estimation was performed using the kinetic scheme EASY%Ro (Sweeney and Burnham, 1990) for the first sedimented layer, aged 65.5 Ma. In the present-day profile of the organic matter maturity (Figure 42), 0.25 % of the 150 km discrepancy at the basin bottom is reached using the EASY%Ro. However, the main oil window depths diverge not exceeding 80 m between the two scenarios along the whole 230–1100 km profile interval, while the thicknesses of the source-rock formations in this region cover hun-dreds of meters.

Note that the absolute basal heat flow values demonstrated in this section should be viewed with caution, because there is a lack of reliable thermal properties data used for the model's construction and heat flow estimates.

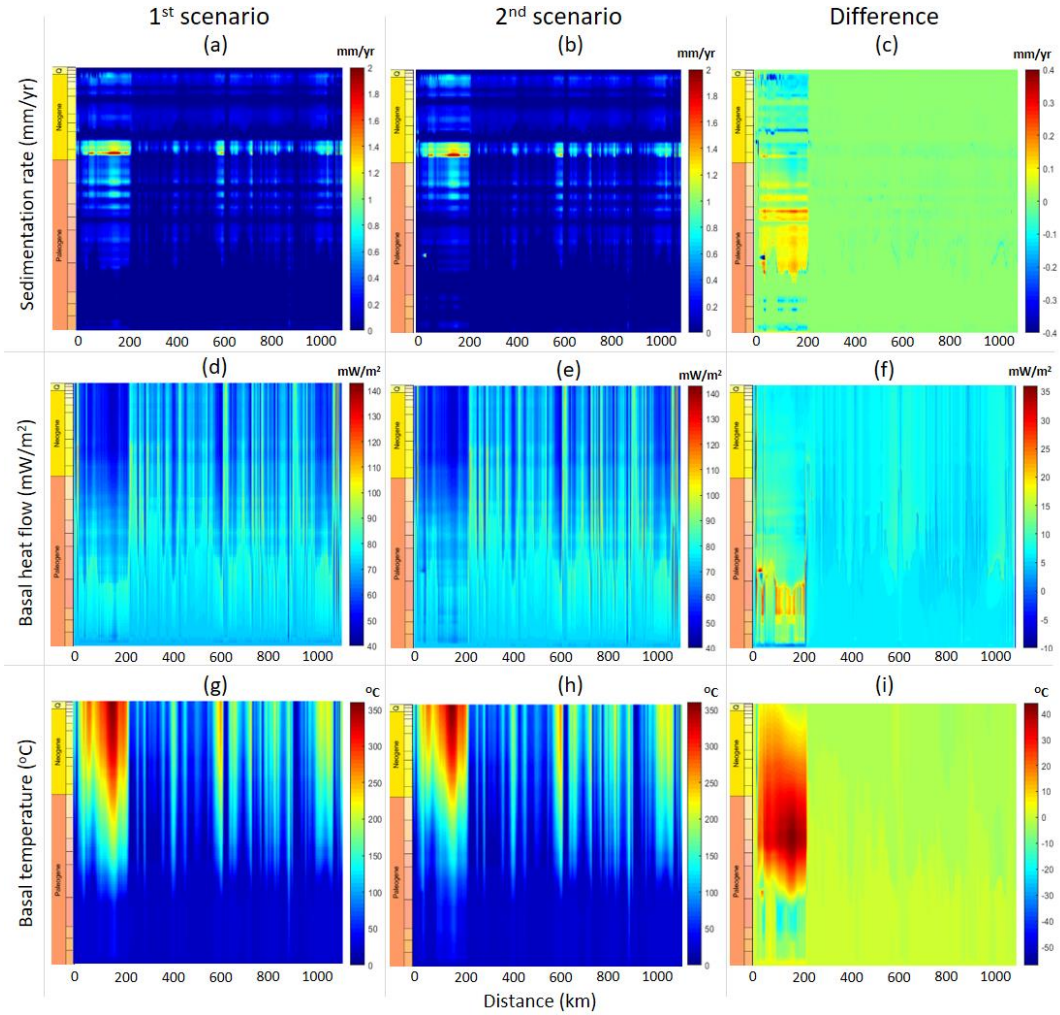

Figure 41. Illustration of the sedimentation rate, basal heat flow, and basal temperatures in time for the first scenario ((a), (d) and (g), respectively) and for the second scenario ((b), (e) and (h), respectively). (c), (f) and (i), modified after Peshkov et al. (2019), show their differences.

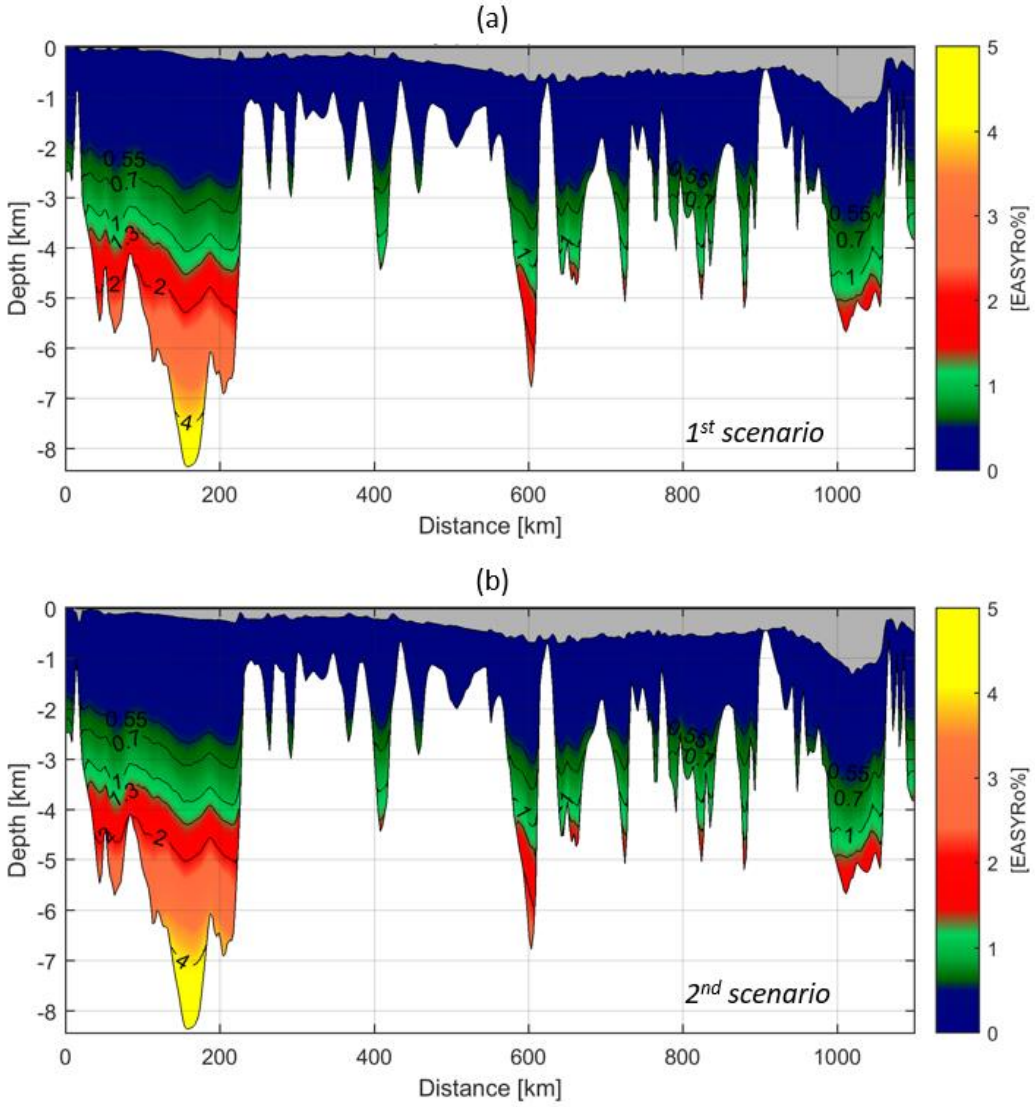

Figure 42. The present-day maturity profile using the EASY%Ro model (a) for the first scenario and (b) for the second scenario.

4.3.4 Conclusions

In the example given by CDP 1632 in the Okhotsk Sea Basin, the minor role played by the gravity anomaly fitting in the thermal history reconstruction is determined when the uniform distribution of the density and thermal conductivity properties per strata are set. The study was conducted using two models constructed considering different lithosphere's tectonic evolution scenarios and calibrated by fitting either temperature and gravity data or temperature and structural data for the basin. Con-

structed models allowed the re-construction of two extreme thermal history cases for the studied basin, providing minimum and maximum temperature estimates. Constructed models cannot be calibrated to simultaneously fit gravity anomaly and seismotomography data in the profile interval of 0 – 230 km without the corresponding adjustment of the basement's structure and properties. However, the computations with the models, calibrated on the wellbore temperature and vitrinite reflectance data, show that both scenarios closely estimate the rock maturity profile for the studied transect. For instance, it is observed that the main oil window shifts vertically by not more than 80 m in the 230–1100 km profile interval, while in the 0–230 km, it remains almost unchanged.

4.4 A summary of conclusions regarding gravity analysis in basin modelling

In Section 4.1, we proposed a so-called express estimation method that explains the need to consider the HB in terms of thermal history reconstruction in full-rank 3D basin models. The express estimation method is based on reduced-rank inversion, using two-dimensional (2D) basin-modelling simulator capabilities. In contrast to customary inversion, reduced-rank inversion does not require the use of seismic data; rather, it obtains the petrophysical properties of the HB and of its geometry. The proposed procedure uses geological maps of the basement and gravity anomaly data.

Two cases (with and without basement heterogeneity) were considered in order to estimate the role played by gravity data fitting in thermal history reconstruction. In the case of the West Siberian Basin, it was proven that a more in-depth analysis of gravity data could lead us to revise the maturity rank of the Bazhenov source rock – from the main oil window to the early oil window along the entire length of the 127 km profile.

In the case study of the Okhotsk Sea Basin, it was proven that the applied fitting of gravity (instead of seismic tomography) fitting results in the level of the main oil window shifting not more than 80 m in a source-rock formation with a thickness of over hundreds of meters. Based on these case studies, we can conclude that accounting for gravity data analysis and fitting is obligatory for basins with HBs.

Chapter 5. The extended version of the developed workflow for 3D thermal history reconstruction

This chapter describes the development of the advanced extension of the workflow for the coupled 3D thermal history reconstruction and demonstrates its successful application in the study of the South Kara Sea Basin.

5.1 Workflow for the coupled 3D thermal history reconstruction

The workflow is based on a combination of the 3D basin modelling advantages of the backstripping-based approach (Hantschel and Kauerauf, 2009) and a 2D thermo-tectono-stratigraphic approach (Rüpke et al., 2008) through the geostatistical processing of data (Figure 43). The workflow integrates the previously suggested workflows for the 2D solution given in Chapters 2, 3 and 4.

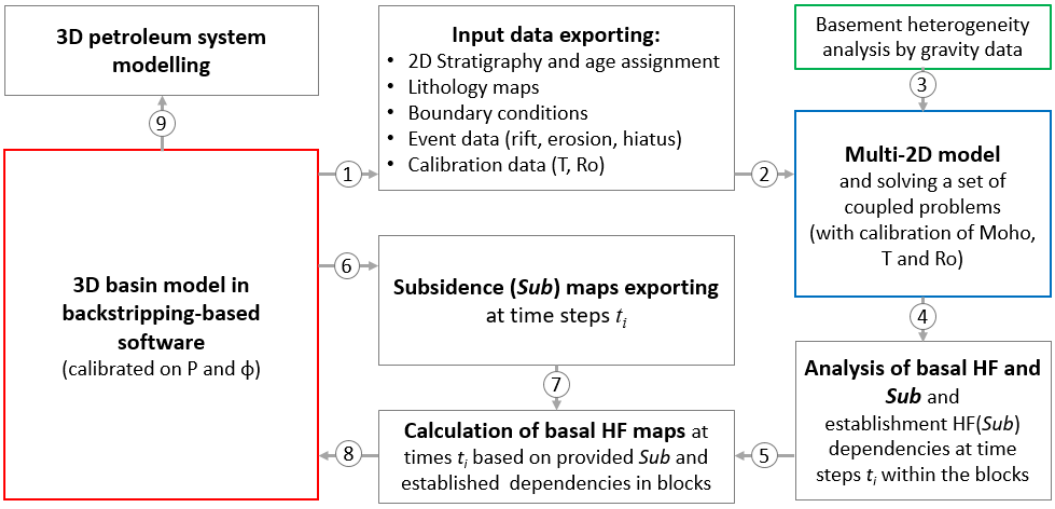

Figure 43. Workflow combining a 3D backstripping-based approach with thermo-tectono-stratigraphic 2D modelling, resulting in a consistent 3D basal heat flow historical reconstruction. The models and massive data are found in the red boxes, while the grey boxes contain the actions that are to be carried out.

The 3D basin model (red box) should be created in the backstripping-based simulator, since this can obtain the structural history of a basin and usually has the most advanced option for petroleum system modelling.

When the creation of the 3D structural model is complete and material properties are determined to be one of the three methods (see Section 2.1), it is necessary to fit the modelled vs measured porosity data and pressures through the refinement of geomechanical and petrophysical parameters. Next, in Step 1, it is required to analyse the study area by the basement's regional structure in order to define the blocks with different burial depths, different tectonic and geological histories and various basement constructions. Following this analysis, a net of 2D sections is created that covers as many blocks with different geological histories and reference wellbores as possible, which will be exported from the 3D model as part of Step 1.

Step 2 involves the creation of a multi-2D basin model (the blue box in Figure 43) in the CSTM-based simulator. It is essential to create grids in the same scale in both the backstripping-based and the CSTM-based simulator.

Step 3 involves express estimation, which is performed in order to understand the need to consider the HB (should it exist) in terms of thermal history reconstruction, based on the 2D analysis of gravity data (shown by the green box in Figure 43), as described in Section 4.1. In cases where a reconstruction of the basement heterogeneity is required, a reduced rank-inversion (Figure 20) should be undertaken.

In Step 4, we export the basal heat flow maps, basement subsidence maps and maps of PWD at t_i time steps from multi-2D models. Next, we subtract the PWD maps from the subsidence maps at time steps t_i in order to obtain the basin subsidence caused by the sediment load only (*Sub*).

In Step 5, it is necessary to determine the regression dependencies of the heat flow (HF) values and (*Sub*) at time steps t_i in each delineated block from Step 1 separately. In addition, splitting the basin's history into several (or multiple) time intervals is recommended to achieve more accurate regression dependencies.

Step 6 involves the exporting of subsidence maps from the 3D backstripping-based model (shown by the red box in Figure 43). It is recommended that the subsidence maps be calculated using an assumption of PWDs equal to zero at each in-plane point and each time step t_i.

Step 7 reconstructs the basal heat flow maps for an all square of the study area. This is achieved by applying established regressions at Step 5 in each delineated block from Step 1 to the subsidence maps from Step 6.

Here is essential to mention that Clark et al. (2014), Theissen and Rüpke (2010) and Peshkov et al. (2021a) all observe a discrepancy in the depth-dependent thinning of both backstripping- and CSTM-based approaches that could contribute to uncertainties in reconstructed basal heat flow maps. In order to evaluate the impact of uncertainties, it is necessary to estimate the discrepancies of *Sub* curves extracted from both backstripping- and CSTM-based approaches along the multi-2D profiles.

In Step 8, the obtained basal heat flow maps are imported into the 3D model (shown by the red box in Figure 43), serving as the lower boundary condition at the basin bottom. The thermal task then calculates for further petroleum system modelling.

5.2 A case study from the South Kara Sea basin

This section, which concerns the example of the South Kara Sea Basin (Figure 44), offers a demonstration of the workflow's application (Figure 43), showing its ability to precisely reconstruct a 3D thermal history. It is essential to mention that details and certain results from some of the models used are not described in this section, since these data were used and processed during a commercial project.

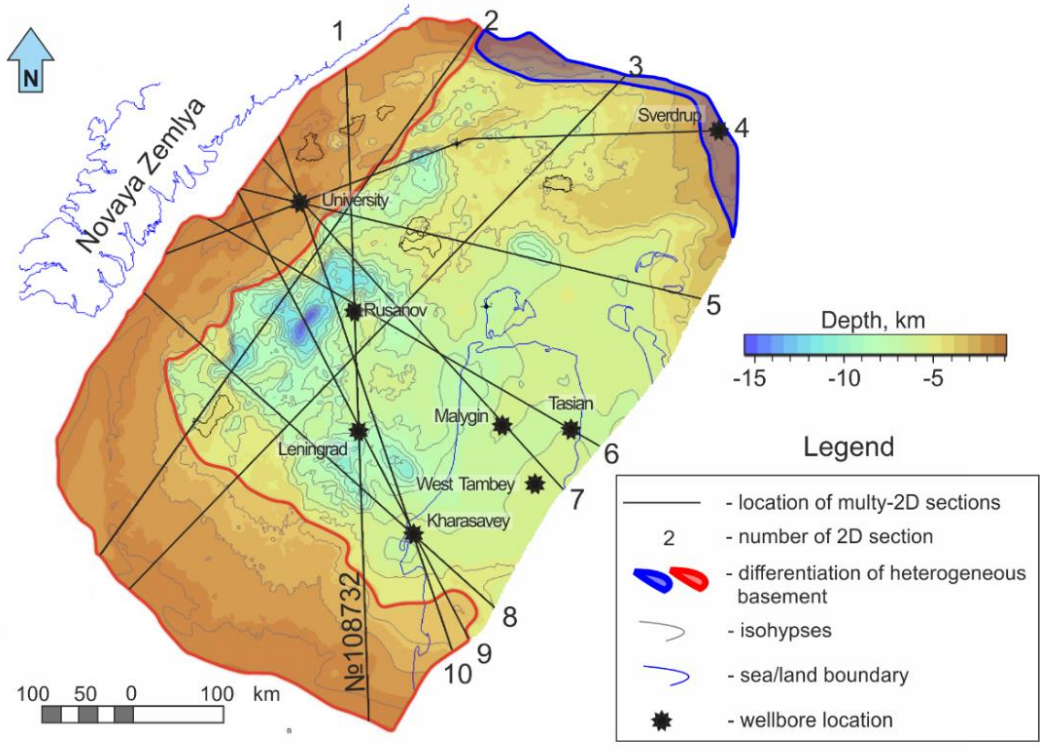

Figure 44. Structural map of the top of the pre-Triassic deposits in the South Kara Basin, with the studied profiles, wellbores and delineated zones of HB blocks indicated.

5.2.1 A brief characterisation of the South Kara Sea basin model

The 3D basin model is created in the backstripping-based simulator. The geological model assumes that the Archean–Proterozoic and Paleozoic platforms' weakly dislocated metamorphosed deposits are the basement for the Mesozoic–Cenozoic sedimentary cover. The Airy isostatic model is used in this work. The lithosphere layers' initial thicknesses

are 30 km for the upper crust, 10 km for the lower crust, and 80 km for the upper mantle. The stretching of the lithosphere elements (with a rifting period of 250–232 Ma) is assumed to be non-uniform. The post-rift Jurassic subsidence is followed by a series of tectonic uplifts, accompanied by erosion, from 34 to 2.1 Ma. Erosion predominates along the periphery (up to 1500 m thick) of the South Kara Basin's central part. The model considers the widespread occurrence of Pleistocene glaciation from 2.1 to 0.75 million years, with an assumed thickness of at least 100 m, followed by rapid uniform erosion of sediments to about 50 m throughout the study area.

5.2.2 The basal heat flow reconstruction procedure

When the model was first constructed, the porosity and pressure regimes were calibrated and three basement blocks with different geological and thermal histories were delineated (Figure 44). The red-coloured (the North Siberian threshold) and the violet-coloured areas correspond to the Timanides' structural-formation zone (Nikishin et al., 2019), while the not-coloured area corresponds to the Hercynian folding (Nikishin et al., 2019).

Next, ten 2D geological sections (Figure 45) were extracted from the 3D CSTM-based model and imported into the BFTM-based simulator in order to create the coupled multi-2D model described in Step 2.

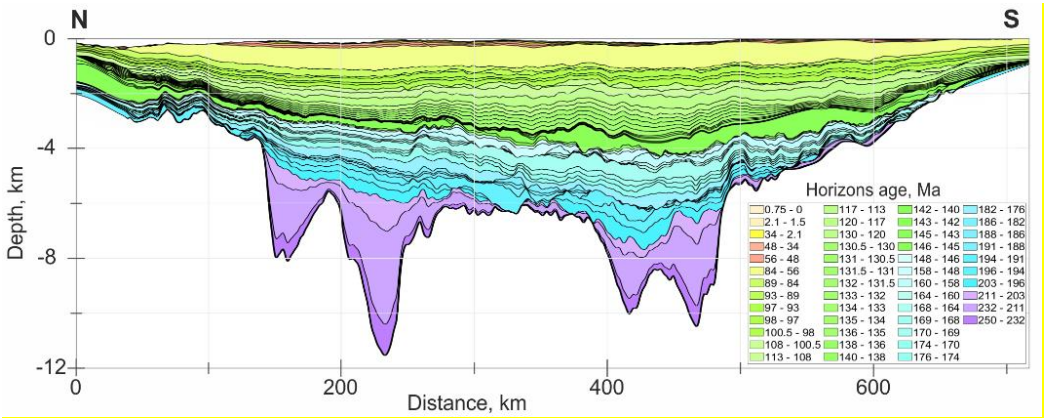

Figure 45. An example of the stratigraphy Profile №108732, used for 2D thermo-tectono-stratigraphic modelling.

The basement heterogeneity analysis presented in Step 3 (Section 4.1) is ignored due to poor basement data. Only the refinement of thermal

properties using basement blocks from the map showing the different basement formation megazones is conducted, based on the analysis of the wellbores thermal regime and regional basement map (Nikishin et al., 2019). Data regarding the measured thermal properties are absent.

In Step 4, the following are exported from the multi-2D model: basal heat flow maps (Figure 46a); basement subsidence (Figure 47a); and PWD maps (Figure 47b) at each t_i time step. A total of 30 control points t_i in time are chosen (at 0, 0.75, 1.5, 2, 3, 5, 10, 14, 20, 25, 30, 34, 48, 56, 84, 93, 105, 113, 120, 130, 140, 143, 148, 158, 164, 170, 182, 190, 203 and 232 Ma). Next, the PWD maps are subtracted from the subsidence maps at each corresponding time step in order to obtain the basin subsidence using the sediment load (*Sub*) only.

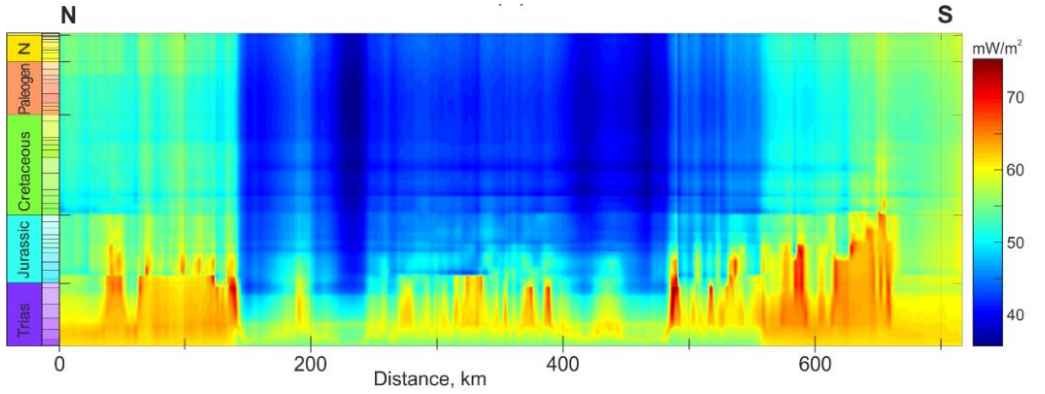

(a)

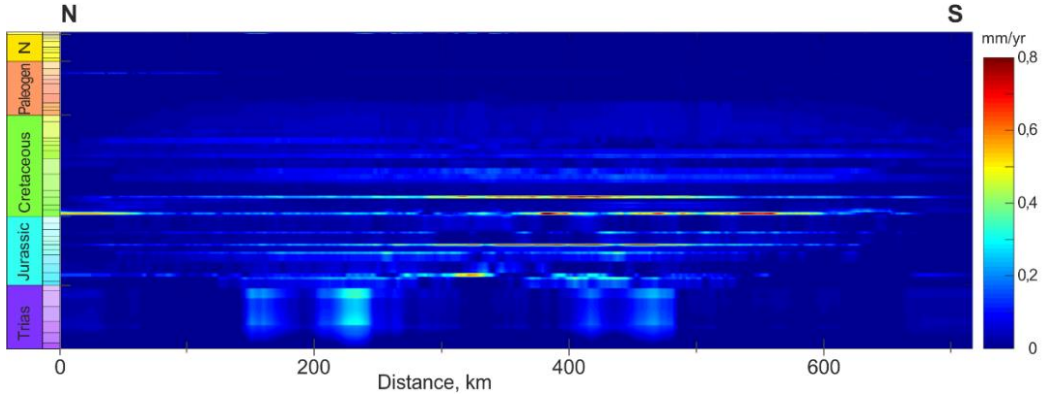

(b)

Figure 46. Simulated temporal variations along Profile №108732 for (a) basal heat flow maps and (b) sedimentation rate.

Step 5 determines three regression dependencies (R_r, R_g, R_b; Figure 49b) for basal heat flow values (HF) from *Sub* at time steps t_i (Figure 47a) in each delineated block (Figure 48a).

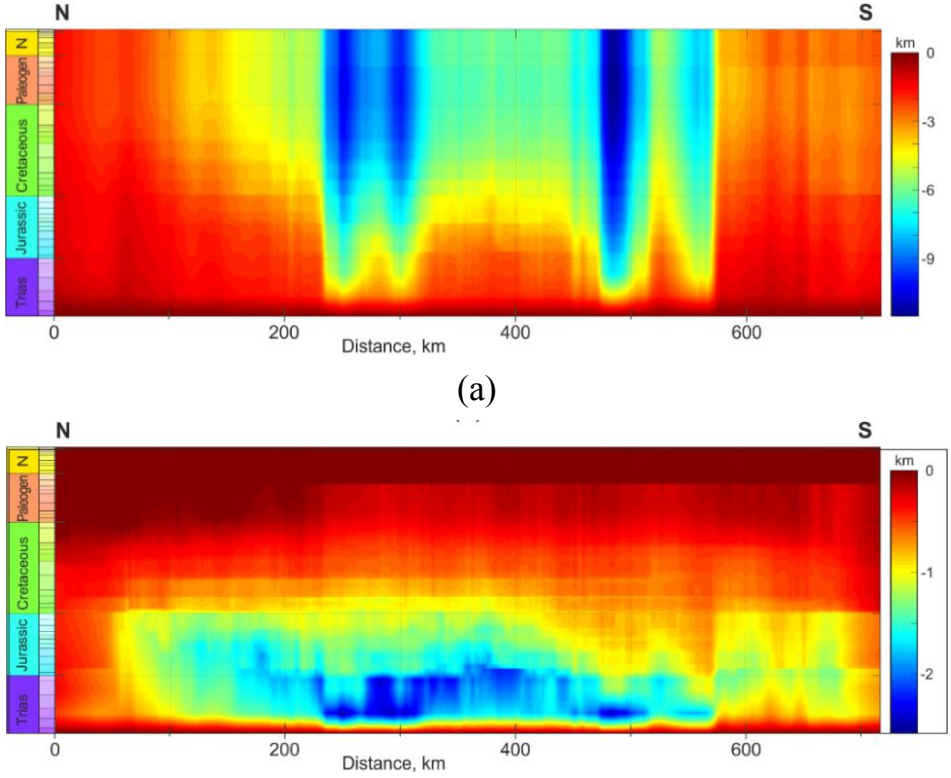

Figure 47. Simulated temporal variations along Profile №108732 for (a) basin subsidence and (b) PWDs.

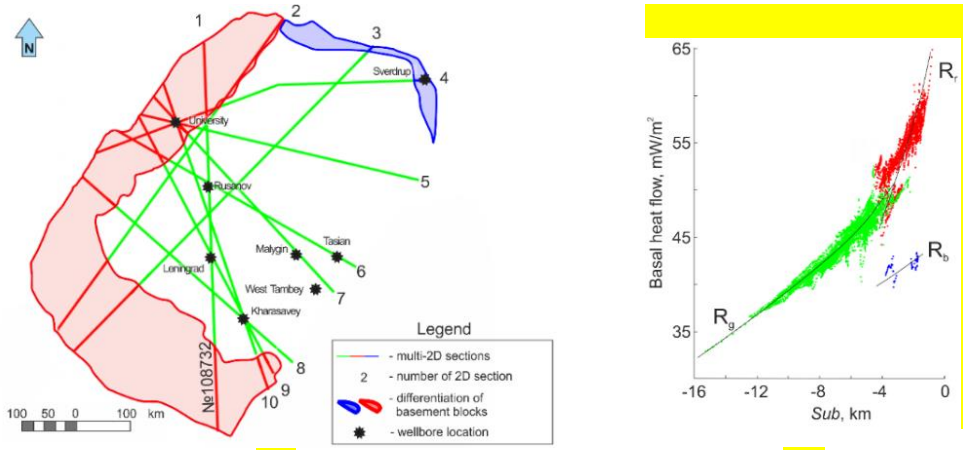

Figure 48. (a) Three delineated blocks for regression analysis; (b) a cross-plot for three regressions.

Step 6 exports subsidence maps from the backstripping-based model (the red box in Figure 43) for all study areas of the 3D model at time steps t_i. Next, in Step 7, basal heat flow maps are reconstructed at 30 time steps t_i (Figure 49) for all study areas, using three regressions (R_r, R_g, R_b; Figure 49b). The present-day basal heat flow map is presented in Figure 49. A selection of 18 paleo basal heat flow maps are given in Appendix B, in Figure 53, Figure 54, and Figure 55; these have been chosen as the most informative maps out of the 30 reconstructed.

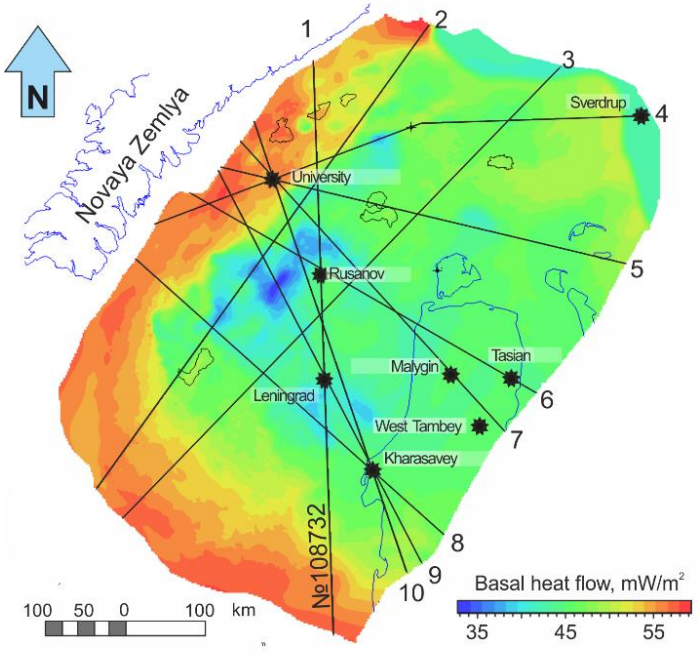

Figure 49. Map reconstructed out of basal heat flow regressions at 0 Ma (see legend in Figure 44).

5.2.3 Discussion of the results

The analysis of thermo-tectono-stratigraphic models has demonstrated that basal heat flow values are primarily controlled by various tectonic events and rates of sedimentation. In Profile №108732 (Figure 45), it is observed that, during the rifting period, the basal heat flow values (Figure 46a) are higher in the basement uplift zones that have no sedimentation, and lower in the zones of graben-like structures (Figure 46b). Heat flow values decrease in line with increasing basin depth (Figure 47a). Moreover, the magnitude of heat flow in this area of graben-like structures

is reduced by an increase in the sedimentation rate (Figure 46b). This phenomenon is explained by the blanketing effect (Lucazeau and Le Douaran, 1985; Wangen, 1995) when colder deposits with low thermal conductivities quickly overlap warmer deposits. This effect is seen in the explication of the basement heat flow evolution and sedimentation rates at the point of the profile, corresponding to the Leningrad-1 Well (Figure 50); each wave of sedimentation is accompanied by a corresponding decrease in the heat flow value.

Figure 50 provides estimates of sedimentation rates from Ognev et al. (2019). These were made using the decompaction approach with using an averaging of sedimentation rates. Such an approach is used in the backstripping-based simulators and does not consider the stretching of sediments. The underestimation of sedimentation rates and stretching of sediment cover by the backstripping-based approach leads to an overestimation of heat flow values compared to the values in the thermo-tectono-stratigraphic (CSTM-based) approach.

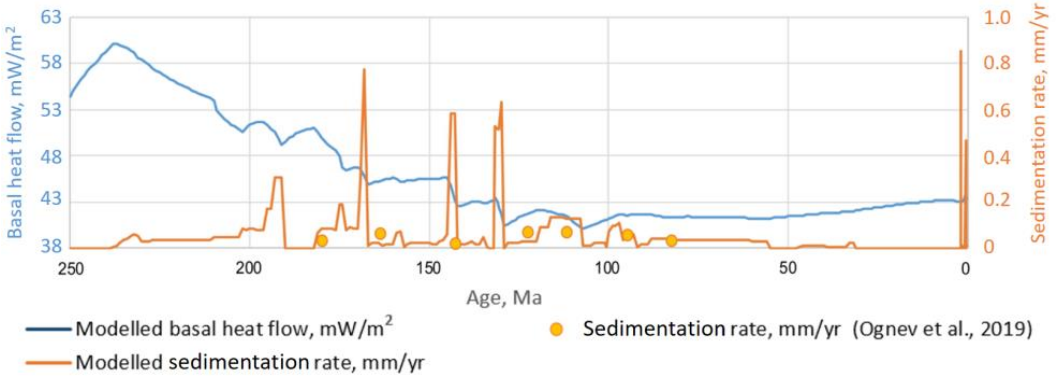

Figure 50. Evolution of basal heat flow values and sedimentation rate in the Leningrad-1 Well, with a time resolution of 1 Ma. The yellow circles indicate the values of the sedimentation rate (Ognev et al., 2019).

A gradual increase in the heat flow values along the all Profile №108732 (Figure 46a) over the last tens of millions of years is associated with a gradual decrease in the paleotemperature at the upper boundary condition. The paleoheat flow values along the periphery of the profile are higher throughout the basin's history, not only because of the lower thickness of the sedimentary cover, but also because of the different thermal properties of the basement that were established during the analysis of the

wells' thermal regime. In addition, in the post-Oligocene epoch, the increase in heat flow values observed along the periphery is associated with the thickest erosion.

The case study of the South Kara Sea Basin observes a discrepancy in depth-dependent thinning curves, as discussed in Sections 1.1.3 and 3.2 and in Clark et al. (2014), Theissen and Rüpke (2010) and Peshkov et al. (2021a). Compared to the CSTM-based approach, the backstripping-based approach underestimates subsidence values caused by sediment load (*Sub*) (Figure 51) because of not accounting for sediment stretching (Clark et al., 2014)

.

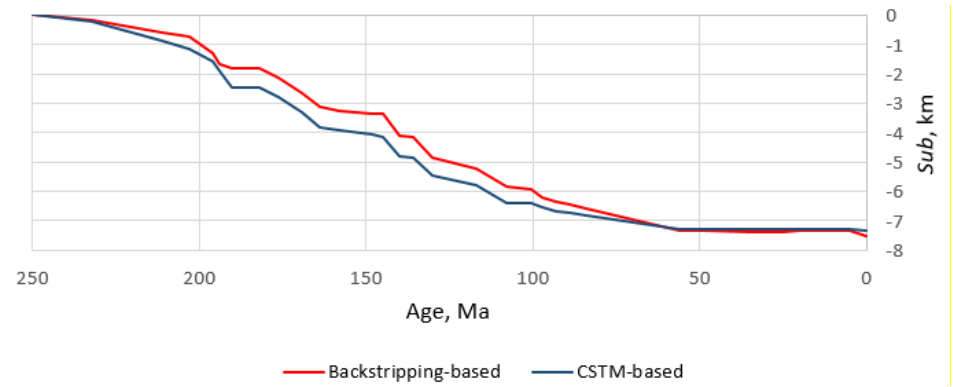

(a)

(b)

Figure 51. 1D model extraction at the location of the Leningrad-1 Well by time step t_i: (a) curves of subsidence caused by sediment load (*Sub*); (b) basal heat flow values modelled by the CSTM-based approach and reconstructed by a regression (R_g).

The maximum discrepancy of the *Sub* values in the Leningrad-1 Well reaches 0.76 km at a −4.1 km subsidence (at 145 Ma). According to the cross-plot (Figure 51b), such a discrepancy can lead to up to 1.5 mW/m^2 deviation in the basal heat flow estimation using the developed regressions. Particularly in the case of the Leningrad-1 Well, the discrepancy between the modelled and reconstructed by regression basal paleo-heat flow does not exceed 1.5 mW/m^2. Such a discrepancy is acceptable, since it allows us to achieve the thermal calibration of the model when feeding heat flow data (maps) into the BFTM-based simulator as the lower boundary condition at Step 8, with no additional calibration actions required.

5.2.4 Conclusions

In this section, the South Kara Sea Basin's basal heat flow maps were reconstructed using geostatistical dependencies based on a combination of the 3D backstripping-based model and the multi-2D coupled structural and thermal model. The thermal history was reconstructed along ten 2D profiles that cover three basement megablocks with different geological histories. Three separate regressions of basal heat flow values and subsidence values by the sediment load derived from the coupled solution were also established.

Despite a slight discrepancy in the subsidence figures derived from the backstripping- and CSTM-based approaches, the thermal regime's calibration from the multi-2D solution was preserved after the basal heat flow maps had been fed into the 3D model of the BFTM-based simulator. The reconstruction of the basal heat flow is highly accurate; this is because it considers the effect of sediment stretching and non-linear sedimentation rates. Such an approach does not require additional input data on PWD maps, which usually contribute additional uncertainties in modelling results.

The 3D model thus presented can be refined by integrating measured rock thermal properties instead of the database values. The obtained results reduce the range of the possible basin evolution scenarios, which helps to minimize economic risks during the exploration and development of the Arctic Shelf.

Chapter 6. Summarised conclusions and recommendations

6.1 Conclusions

Thermal history reconstruction is a crucial task in BPSM. However, despite the huge amount of interest in thermal modelling coming from both the scientific community and industry, there are still severe challenges to obtaining a reliable approach to conducting thermal history reconstruction.

This thesis has cumulated and demonstrated the drawbacks of modern thermal history reconstruction approaches, predominantly for rift basins. It has established that the drawbacks produce significant uncertainties in thermal modelling results and has assessed the impact of such uncertainties on petroleum system modelling. It then suggests three workflows, designed to reduce such uncertainties, that take advantage of the capabilities of present-day technical software.

There are many pitfalls in the present day's customary approach to the geothermal characterisation of a model: neglect of the thermal conductivity and the measured basal heat flow; significant uncertainties in thermal conductivity coming from petrophysical databases; the use of the Sekiguchi model; the application of the widely used geometric-mean mixing rule to determine bulk thermal conductivity; and the use of old, unreliable HFD maps. Calibration using these old maps leads to incorrect thermal models in which the uncertainties concerning rock thermal conductivity and HFD are often underestimated and significantly impact the reconstructed thermal regime and, hence, the petroleum system modelling. The use of reliably measured HFD is an indispensable aspect of thermal modelling. The case study of the superdeep Tyumen SG-6 provides evidence for these conclusions. The lack of reliable experimental geothermal data (which is often replaced with data from databases) produces many different combinations of thermal conductivities and HFDs. It can also produce different scenarios for the maturation of source rocks, even when a model is calibrated against temperatures and vitrinite reflectance. Hence, the method for the thermal model characterisation at the present-day is presented.

This thesis also establishes when gravity calibration is required for proper reconstruction of the basin's thermal history. The case study from

the Okhotsk Sea basin, characterised by the uniform distribution of densities and thermal properties per strata, allows us to ignore gravity fitting. In comparison, the case study from the West Siberian Basin, characterised by an HB, demonstrated that, in such instances, the role of gravity analysis becomes important to thermal history reconstruction and petroleum system modelling. In the West Siberian case study, the additional calibration on gravity data allowed us to re-estimate the location of the main oil window up to 127 km along the 808 km profile. The workflow coupled with the reduced-rank inversion procedure, which uses gravity anomaly and HB's maps for the HB reconstruction, is presented.

The use of the decoupled thermal and structural solution produces inconsistent thermal models and leads to significant uncertainties in petroleum system modelling, despite the successful calibration on temperatures and vitrinite reflectance. Ignoring the blanketing effect and sediment stretching leads to an overestimation of time-dependant basal heat flow, thereby producing uncertainties in estimations of timing and mass for hydrocarbon generation. The case study from the West Siberian basin provides evidence for these conclusions, demonstrating that the Neocomian blanketing effect plays a significant role in the reconstruction of the palaeothermal regime. Ignoring the blanketing effect could lead to overestimating hydrocarbon mass by 86 wt.% and the critical moment 12 Ma early. In the case of the south-western Barents Sea (Hammerfest Basin), it was proved that ignoring the blanketing effect could lead to the change in estimations of the source-rock's maturity reaching up to 0.25 Ro% and peak temperatures in the past reaching up to 45 ^{o}C. The workflow, which combines the thermal model from the CSTM-based approach with the petroleum system modelling abilities of the BFTM-based software, is presented.

At present, there is as yet no perfect software solution to producing a consistent 3D coupled thermal and structural solution, which highlights the need to create such a software in future. This thesis provides the workflow, that allows us to combine the best advances of 2D thermo-tectono-stratigraphic modelling with a 3D structural solution for the backstripping approach through the geostatistical survey makes the 3D thermal solution the most reliable option. Any uncertainties are reduced by means of accounting for the lateral heat transfer effects, sediment stretching and the

non-linear sedimentation rate. In addition, this approach does not require paleo-bathymetry as input, which is beneficial as this usually contributes additional uncertainties to the modelling results. The demonstration of the provided workflow is performed on the example of the South Kara Sea Basin.

6.2 Recommendations

It is recommended to reduce the uncertainties in geothermic model characterization by use of the best advances in thermal petrophysics (Popov et al., 2016, 2012), i.e. by the measurements of the reliable thermal conductivities, their thermobaric corrections and HFD with further these data integration into the model. Such a reliable 1D thermal model should be used as a reference model for 2D and 3D thermal modelling of a basin. In addition, the presented method for integration of measured thermal properties under thermobaric conditions in basin model could be also useful for the reservoir models building and computation. The method may require some modification according to the specificity of data input into reservoir modelling software.

Based on the advances in thermal petrophysics, it is needed to develop new mixing rules or modifications of existing rules, update thermal conductivities and its thermobaric corrections in databases and revise present-day HFD old-measured maps.

In the present work, three workflows have been presented and recommended to reduce the significant uncertainties in thermal history reconstruction.

The first workflow recommends using the combination of the advances of coupled thermo-tectono-stratigraphic modelling with the best advances of petroleum systems modelling from backstripping-based simulators in 2D.

The second workflow is recommended to account for the structure and thermal regime of the HB by using gravity data and geological maps of the basement to consider the thermal impact of poorly studied deep structures. The workflow is primarily recommended to the regions where the poorly studied earth interior of the basin are identified with the economic basement or acoustic basement. Nevertheless, using the gravity data is strictly recommended for basin model construction to get a view of the lithosphere structure. Otherwise, the heterogeneity of the basement might not be known.

The third workflow is recommended to use as an extension of the first workflow to reconstruct thermal history in 3D. It bypasses the drawbacks existing in the 3D decoupled thermal and structural solution.

Following the above recommendations, modellers can significantly reduce the uncertainty in 1D, 2D, and 3D thermal models and quantitative estimates of the generation, migration, and accumulation of hydrocarbons.

Aside from applying the results in oil and gas exploration and production, the results of this PhD thesis can also be useful for estimating geothermal resources. The developed method and three workflows open up a number of new opportunities to improve the accuracy of resource estimates for geothermal energy exploration. This application of the PhD thesis results could play a major role in the energy transition period when the interest from energy-producing companies significantly grew in the sphere of geothermal energy.

Appendix A

A.1 Theory of the lithosphere extension

The sedimentary basins' life cycles are directly connected with the Wilson cycles (Wilson, 1965). Thus, using this theory as a frame, we can consider any basin's genesis through the concept of convergent, trans-current and divergent plate motions (Kingston et al., 1983). The so-called rift–drift divergent mechanism creates different types of basins for continental and oceanic lithospheres. In the case of a continental substrate, the following basin types are created: cratonic sag, failed rift, and passive margin. In the case of an oceanic substrate, the types created are rift on ridge, proto-oceanic rift and active oceanic (abyssal) basins (Allen and Allen, 2013). Both substrates are parts of an evolutionary sequence of basins, which are unified by the lithospheric extension processes (Dewey and Bird, 1970; Dietz, 1963; Veevers, 1981). Thus, the unifying terminology is used for all extensional basin types, as this thesis uses a rift basin.

There are two mechanisms in the characterisation of the continental rifting process (Allen and Allen, 2013). The first is passive rifting, whereby a mechanical extension of the lithosphere is established by indeterminate distant tensile forces, with a passive rise in the asthenosphere. This mechanism is associated with Wernicke's (1985) simple-shear model. The second mechanism is active rifting, associated with McKenzie's (1978) pure-shear model, whereby the lithosphere extends in response to ascending the asthenosphere. The syn-rift subsidence that occurs during the stretching of the lithosphere is due to the brittle extension of the crust, while the post-rift subsidence is caused by the thermal contraction of the cooling lithosphere. The active and passive formed rifts disrupt the isostatic equilibrium, and the basin experiences post-rift subsidence due to the hot asthenosphere's thermal contraction. The lithosphere's thinning and subsidence can also be reached by the mineral phase transition in the lower crust or mantle (Artyushkov, 1983; Kaus et al., 2005; Podladchikov et al., 1994).

A.1.1 Lithospheric stretching models

There are three continental riftogenesis models (Figure 52): pure-shear (McKenzie, 1978), simple-shear (Wernicke, 1985), and combined pure- and simple-shear (Barbier et al., 1986; Kusznir et al., 1991; Kusznir and Park, 1987).

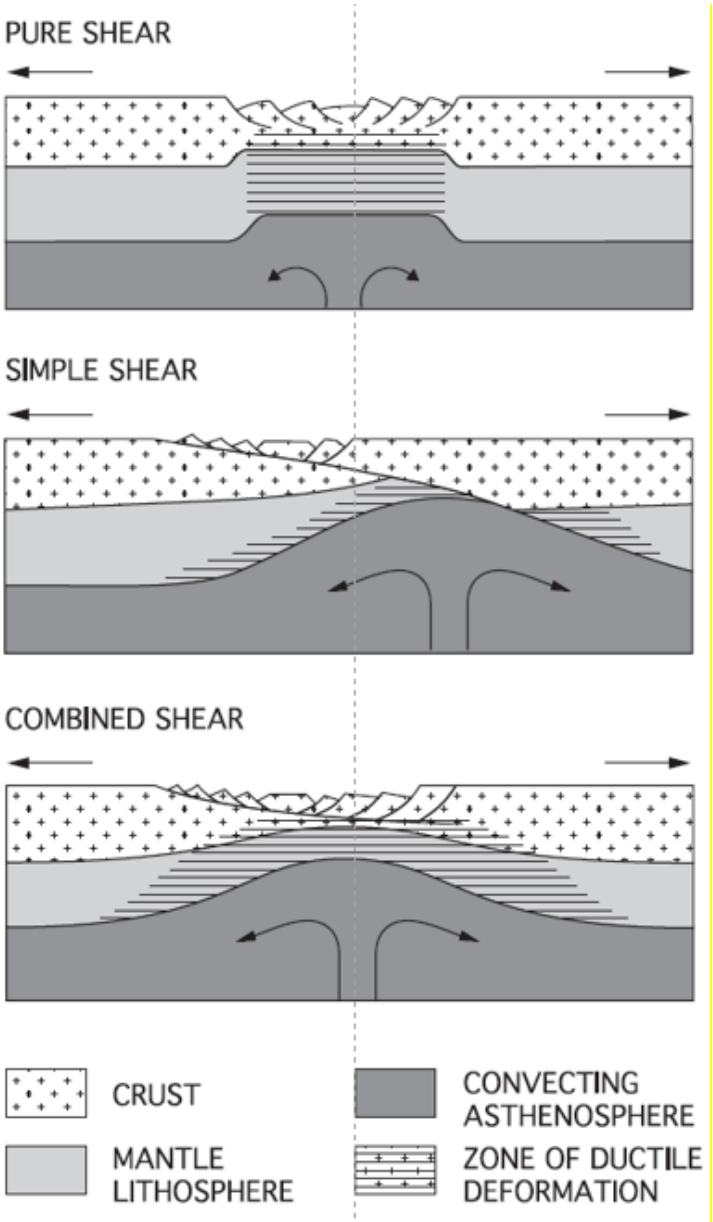

Figure 52. Lithospheric shear models (Ziegler and Cloetingh, 2004).

In the pure-shear model, the displacement of adjacent blocks that move away from the primary fault is not accompanied by a noticeable displacement of these blocks along the fault (which would create a symmetric basin). Various scientists have developed a theory for this model. McKenzie (1978) made the first fundamental attempt to create a passive rifting theory, one in which the syn and post-rift phases of lithosphere evolution were assumed. A rift phase is provided by the uniform stretching of crust and mantle layers; the isostatic compensation determines the raising of the Moho level and sinking of the lithosphere's surface. The pre- and post-rift crustal and mantle layers' geometry is related by the stretching factor (β) as a ratio of thicknesses, while the post-rift subsidence phase is determined to be about 50–60 Ma (Allen and Allen, 2013; Waples, 2001). McKenzie's model also uses the temperature to consider the density dependence of rocks, which allows us to consider thermal lithospheric effects (such as thermal contraction and expansion, which control the thermal subsidence and uplift, respectively).

Jarvis and McKenzie (1980) demonstrate that the assumption of instantaneous stretching is valid for rifting durations of up to 20 million years. The model, which has a constant rate of lithospheric extension, is suggested by Jarvis and McKenzie (1980) and Royden and Keen (1980), and with the exponential rate of the extension by Sheplev and Reverdatto (1998). Numerous researchers have criticised McKenzie's assumption of uniform stretching, since the rheological properties of the crustal and mantle layers change with depth (Vierbuchen et al., 1982). The upper crust should be considered within the brittle rheology, while the lower crust and mantle should be considered within the ductile. Therefore, non-uniform stretching models have been proposed, in which the stretching factors in the brittle upper crust (δ) can be different to those in the rest of the lithosphere (β) (Hellinger and Sclater, 1983; Keen et al., 1990; Royden and Keen, 1980; Sclater and Christie, 1980; Steckler, 1985; Vierbuchen et al., 1982; White and McKenzie, 1988).

Waples (2001) modified one more assumption in the McKenzie model of heat sources. Based on previous studies (Jaupart, 1986; Kusznir and Park, 1987; Sclater and Christie, 1980), he introduced a new model that accounts for the radiogenic heat of the crust and mantle, wherein the asthenosphere heat flow accounts for about 40% ± 10% of the heat flow at

the top of the basement. The idea that thermal conductivity in the lithosphere changes with temperature is suggested by Royden and Keen (1980).

Wernicke's (1985) simple-shear model describes a riftogenic basin's formation with extended width, without the assumption of a significant thinning of the underlying crust. Here, the formation of listric faults on a particular shear surface within the brittle crust is linked to the lower ductile lithosphere and asthenosphere. This model is considered primarily at a qualitative level, since the asymmetric disconnect between the stretched/rotated lithosphere and the thermal anomaly is difficult to quantify. The basin investigations have proved that, while both of the processes described by McKenzie and Wernicke are presented in nature simultaneously (Galushkin, 2007), they can affect rift evolutions at different times. Pure shear mechanism acts on relatively thick crusts, while simple shear mechanism dominates in extended crustal margins.

Barbier et al., (1986) Kusznir et al., (1991) and Kusznir and Park, (1987) presented a hybrid of the pure- and simple-shear models. Here, the simple-shear model works in the upper crust to create listric faults, while the pure-shear model provides the ductile thinning in the lower crust and mantle layers.

In fact, the most popular model used in quantitative basin analysis is the pure-shear model (McKenzie, 1978) with the modifications listed above that describe the active rifting processes (Baur et al., 2018).

A.1.2 Isostasy

Different isostasy theories are used to explain the long wavelengths (100–200 km) found in the topography of the Earth's surface and at the bottom of the lithosphere (Abrehdary, 2016; Gvirtzman et al., 2016; Watts, 2001). Watts defines isostasy, saying that it 'considers there is a certain surface within the Earth, known as the depth of compensation, on which the vertical stresses due to an overlying column of rock are equal' (2011, p.647). There are three distinctly different approaches used to account for isostatic compensation: hydrostatic, flexural, and thermal (Watts, 2001, 2011).

The first approach, the hydrostatic approach, is based upon Archimedes' principle of hydrostatic equilibrium, whereby the less-dense Earth crust 'floats' in a denser mantle. The lithospheric shell tends to reach a

gravitational equilibrium, taking the shape of a geoid. The weight of the solid lithospheric column, overburdening the liquid–ductile mantle, should be equal to the reference lithospheric column's weight if it is to approach an isostatic equilibrium. Isostatic equilibrium is usually associated with a non-changed continental lithosphere. The thinned lithosphere, loaded with sediment and water, tends to reach equal gravity with the reference column. Airy (1855) and Pratt (1855) suggested the first isostatic models in this regard. The Airy model assumes a permanent density for the entire crust. According to this model, the 'roots' of the mountains are formed, called the compensation mass. The higher the mountain, the larger the root, the thickness of which should be several times greater than the height of the mountain range above sea level. In Pratt's model, the bottom of the Earth's crust is assumed to be flat. Thus, isostatic compensation is driven by the variations in the density of the crustal blocks (i.e., the crustal density should be lower in blocks of mountains than in blocks of depressions). Both isostatic models involve the assumption of a local compensation in a point, where there is no influence by adjacent points to each other.

Vening Meinesz (1941) suggested a more sophisticated and realistic model wherein the lithospheric loads are compensated regionally and described by their flexure. In Meinesz's model, the Earth's crust behaves as an elastic plate that bends under its own weight; that is, it is not split into separate blocks but is a single whole. The elastic plate is described by an elastic thickness (Te) and NL parameters. The higher the value of Te, the more widespread flexural effects become. If Te is equal to zero, then the flexural isostasy becomes the Airy isostasy. Here, NL is a neutral plane of vertical stresses in a pure-shear deformation. In other words, it is a theoretical, fixed plane in the lithosphere that remains horizontal during stretching prior to flexural isostatic compensation. A deep NL produces rift shoulders, while a shallow NL results in the downward flexure of the rift basin's lateral boundaries. The NL in the Airy isostasy is meaningless, because 1D columns are balanced independently of the initial lithosphere's geometry (Braun and Beaumont, 1989; Clark et al., 2014; Fjeldskaar et al., 2004). According to Watts et al. (1982), use of the Airy model (instead of the flexure model) leads to a significant underestimation of the amount of lithospheric mantle and crust extension.

The theory of thermal isostasy assumes that the outermost lithospheric layers form a cooling thermal boundary layer and that regional differences in topography are controlled by differences in the temperature structure, which is why heated regions have a higher elevation than cold regions (Nakiboglu and Lambeck, 1985).

Isostasy compensation is essential to constructing the lithosphere's reliable structural model, since it defines the history of a basin in terms of geology and thermal regime. Gravity anomaly data or seismotomography data are instrumental in selecting isostasy models' scenarios, allowing for the construction of a present-day lithospheric model. To date, Airy and flexural isostasy principles are the ones most often used in basin modelling simulators.

A.2 Basin modelling approaches

There are two distinctly different groups of basin modelling approaches used to reconstruct the basin history. The first group is based on a combination of backstripping with forward temperature modelling (BFTM) (Sclater and Christie, 1980; Steckler and Watts, 1978; Watts et al., 1982; Watts and Ryan, 1976), while the second is based on simultaneous time-forward modelling for both the structural and the thermal evolutions (Galushkin, 2016, 2007; Kooi et al., 1992; Kusznir and Ziegler, 1992). In some examples, the latter group uses an iterative forward-modelling scheme for the modelled and input stratigraphy section fitting (Poplavskii et al., 2001; Rüpke et al., 2008; White, 1993).

A.2.1 Backstripping

The backstripping-based group of approaches determines the structural basin evolution from present-day basin geometry in a time-reversed manner (Watts and Ryan, 1976). Basin reconstruction is achieved by sequentially removing the top layer of sediments accumulated over a specified time interval. The section thickness is re-estimated at each time step by controlling for decompaction from present-day porosity and pressure regime. Normal fault slip between each time step is reconstructed through simple vertical shear. This group's approaches usually involve obtaining the total and tectonic subsidence from the compaction curves of the deposited sediments (Athy, 1930; von Terzaghi, 1923), combined with local or flexural (only for 2D or 3D) isostasy calculations (Norris and Kusznir,

1993; Watts et al., 1982; Watts and Torné, 1992) and assuming a given PWD. The total subsidence in time is derived from sediments and water load by backstripping, while the tectonic subsidence is derived from water load under the assumption that it is caused by instantaneous, pure-shear lithospheric thinning (Lee et al., 2018). Crustal (δ) and mantle (β) stretching factors are obtained through the inversion when the theoretical subsidence is fitted to the tectonic subsidence (see details in Hantschel and Kauerauf (2009)). One of the weak points of a backstripping-based structural approach means that the approach does not account for sediment stretching by lithospheric extension, as it is only carried out locally, through faulting.

The simulation of thermal history is decoupled from the structural solution and is calculated after stretching factors have been determined. Two methods can be used to compute thermal history. The first involves calculating the thermal history on the entire lithosphere scale when the lower boundary temperature condition is set at the lithosphere's bottom. The upper boundary condition is set on the SWI or sediment–air interface (e.g., by temperature). Following this, the heat transfer accounting for the radiogenic heat can be calculated using the non-steady-state solution. As a rule, most backstripping-based simulators calculate the heat transfer problem in multi-1D.

The second method assumes the sequential calculation of heat transfer for the basement and basin infill. First, the heat flow maps need to be calculated on the basement surface. The lower boundary condition in the basement domain is the same as described for the first method, while the upper condition is set on the basement top. Basal heat flow maps are then used as a lower boundary condition at the basin bottom. The non-steady-state heat transfer problem needs to be restricted at the SWI or sediment–air interface's upper boundary (e.g., by temperature). A discussion of the advantages and disadvantages of these methods is provided in Section 1.1.3. The backstripping-based approach is considered in detail by Hantschel and Kauerauf (2009). In this work, the thermal solution limited by basal heat flow at the basin bottom is denoted as backstripping-based with forward modelling (BFTM).

A.2.2 Forward modelling

The time-forward approach starts modelling from an initial configuration of the lithosphere, reproducing the present-day basin configuration. This approach offers a simultaneous solution for full-thickness lithospheric stretching, sedimentation, compaction, temperature, and isostatic flexural and hydrostatic compensation (Rüpke et al., 2008). Forward modelling requires an a priori knowledge of the basin parameters from before the first rifting event. Lithospheric deformation is only accounted using a pure-shear kinematic model, so faults are not explicitly restored. In forward modelling, the stratigraphy section results from a forward run. The most advantageous tool in the forward-modelling approach uses the iterative search's inversion procedure for the optimal set of stretching factors, sedimentation rates and PWD values. The iterative search's inversion procedure minimises the chosen goal function to fit the modelled stratigraphy section to the observed (input). This approach, called as thermo-tectono-stratigraphic and also denoted in this work as CSTM (coupled structural and thermal modelling), is implemented in TecMod software package and is widely used in the present research work. More details can be found in Poplavskii et al. (2001), Rüpke et al. (2013, 2008), Theissen et al. (2010) and Theissen and Rüpke (2010).

A.3 Input data and model calibration

Construction of a basin's model is preceded by the general basin evolution evaluation. It includes information about the basin's tectonic history, any rifting events, and the depositional environments over geological time, paleoclimate and paleo-bathymetry. The model input data can be divided into five groups: present-day model, age assignment, paleo-geometry, boundary conditions, and facies (Hantschel and Kauerauf, 2009). There are slight differences in the input data used in the forward- and back-stripping-based modelling approach. Forward (thermo-tectono-stratigraphic) modelling does not require the use of PWD maps, since they are obtained by the inversion procedure (see, e.g., Rüpke et al., 2008).

A.3.1 Input data

1. The present-day model is usually built using interpreted seismic and well data by reproducing basin geometry, fault structures and facies

maps. The gravity data is used to estimate the lithospheric crust and mantle configuration.

a. The geometry is described by horizon interfaces between two layers, which are usually interpreted from seismic reflections and refined with wellbore data. In areas where there is a lack of data usually are used methods of extra and interpolations.
b. The building of facies maps assumes the characterisation of infilled material between horizon surfaces. One facies corresponds to one sedimentation environment. Lateral facies variation reflects the different sedimentation environments. A layer change usually corresponds to vertical variations in facies.
c. Fault surfaces are built from seismic, well and dips data analysis.

2. The age assignment relates the geometry of the present-day horizon to the geologic age of their deposition, hiatus and erosion. Erosion events require additional maps of the erosion thicknesses and have to be combined with the corresponding PWD in order to characterise the erosion level.

3. The paleo-geometry setting usually assumes knowledge from regional geology, tectonics, and sedimentology, using it to reconstruct eroded paleo-sections, the dynamic of erosion processes, PWD maps, sea-levels and salt movements.

4. The boundary conditions need to be defined for thermal, pressure and fluid flow problems' solutions through the entire modelled evolutionary history. The typical boundary condition data for the heat transfer problem are temperature on the sediment–air or the SWI as an upper boundary, and temperature on the lithosphere–asthenosphere interface or basal heat flow maps on the basin–basement interface. The upper boundary condition is usually obtained from paleoclimate investigations, while the lower for the lithosphere–asthenosphere interface is determined by an isotherm of 1300 °C (Fischer et al., 2010). To obtain the basal heat-flow maps, it is necessary to model the crustal and mantle layers' structural and thermal evolution. The boundary conditions for the pore pressure and fluid flow analysis are ignored in this section, since they fall out of the scope of the research. Further details are given in Hantschel and Kauerauf (2009).

5. A facies map usually characterises the sediment bodies by their common properties (lithology) or by the properties of their organic matter. The sediments' material properties can be determined in two ways, as

follows. (1) Based on the lithological characterisation of rocks and petrophysical database. Here, a variety of rock-mixing rules are used to achieve a full set of the required material properties for each facies (see details in Hantschel and Kauerauf (2009)). (2) Based on measurements of the rock properties. This approach can reduce uncertainties when determining the primary material properties (such as density, thermal conductivity, heat capacity, radiogenic heat production, permeabilities, compressibilities, and capillary entry pressures, depending on temperature and porosity). A detailed discussion of the existing problems related to defining rock thermal conductivities can be found in Section 1.1.1.

A.3.2 Model calibration

Calibrating the basin model is an essential procedure if we are to obtain reliable results and constrain any possible variations. Calibration of the different elements of the model is performed at different steps of the model construction. Following the classic model-building workflows by Al-Hajeri et al. (2009), Hantschel and Kauerauf (2009) and Peters et al. (2017), the calibration procedures (excluding the petroleum system modelling procedure) are undertaken in this order: pressure and pore compaction; gravity; thermal; and the various maturity indicators.

Pressure and pore compaction

Sedimentary model building has to be accomplished involving reconstructing of porosity and pressure evolution. The porosity calibration on geophysical and laboratory-measured data is essential, since the porosity has significant impact on other model's parameters such as bulk thermal conductivity values, bulk density, subsidence and permeability, etc. Ignoring the porosity calibration leads to significant uncertainties in the final results. The calibration of the lithostatic pressure increases the accuracy of the density model, while the calibration of the pore pressure increases the accuracy of the fluid dynamic modelling results (Hantschel and Kauerauf, 2009).

Gravity data

Gravity data analysis is widely used to characterise the sub-basin domain of the lithosphere (Jacoby and Smilde, 2009). The basin model can be calibrated on different gravity interpretations, provided the model is

created under the isostasy assumption. The gravity analysis has several advantages when it comes to constraining the model scenarios: it allows us to characterise the basin/basement interface geometry (Kanthiya et al., 2019; Pallero et al., 2017; Radziamir et al., 2019; Veeken and Titov, 1996) and to estimate the Moho level (Aitken et al., 2013; Eshagh et al., 2011). The analysis is helpful to the density characterisation of large-scale intrusive bodies in the sedimentary and crusts' layers (Hansford, 2014; Radziamir et al., 2019; Saltus et al., 1999; Webb et al., 2001) and to the determination of the continental–oceanic crust boundary (Roberts et al., 2013). In addition, it is used to characterise the lithospheric-scale faults, estimating their strike direction, shape and depth (Abtout et al., 2014; Stein et al., 1989). This calibration step refines the tectonic history of the basin and, hence, the thermal regime of the lithosphere.

The value of the total error in the Bouguer anomaly (Chapin, 1996; LaFehr, 1991) takes into account several components: an error in reference network observation, ε_{rn}; an error in accounting for terrain correction, ε_r; an error in introducing corrections for free air (which depends on the error in the station heights), ε_F; an error in introducing the Bouguer correction (which includes the error in determining the topographic relief and average density of rocks), ε_B; and an error in calculating the normal gravitational field (which is associated with the error in calculating the normal value of the acceleration of gravity and determining the coordinates of observation points, ε_γ (see details in Jacoby and Smilde (2009), Khmelevskoy et al., (2004), LaFehr (1991) and Talwani, 1998 and the links therein). The total error of the Bouguer anomaly must have standard limitations for maps in different scales (Khmelevskoy et al., 2004): the total error should not exceed $\varepsilon_t = \pm 0.4$ mGal for the 1:5000 scale and $\varepsilon_t = \pm 1.5$ mGal for the 1:500,000 scale, which is consistent with Jacoby and Smilde (2009).

The value of total error in the free-air anomaly, compared with the Bouguer anomaly, does not consider the error of accounting for terrain correction ε_r nor the error in determining the topographic relief.

Thermal measurements and maturity indicators

Thermal measurements and maturity indicators are instrumental in calibrating the model's thermal regime. Simultaneously measured temperature and HFD in boreholes allow us to obtain a reliable temperature regime for the present day. The maturity markers (vitrinite reflectance, T_{max},

fission-track, biomarkers) show the cumulative effect of the rock elements' temperatures through history (Hantschel and Kauerauf, 2009).

The model's thermal calibration, which is obtained using different approaches (CSTM and BFTM) can be achieved in various ways. Parametric studies and the refinement of the thermal properties of the all lithosphere and the tuning of radiogenic heat production in the crust with depth are suitable for use with both approaches. An exponential reduction of the radiogenic heat production of the crust (A) from a surface value (A_0) at a rate given by the e-fold length can be varied (Lachenbruch, 1968, 1970), see the formula in the footnote of Table 4. A local tuning the heat flow values at the basin/basement interface is suitable for a back-stripping based solution when the computational domain of the heat problem is limited by basin bottom.

When calculating *vitrinite reflectance*, we consider the uncertainty in the experimental determination %Ro, employing the kinetics model used for %Ro calculation. Often, if experimental data are absent, specialists use different standard kinetic models (see, e.g., Nielsen et al. (2017), Schenk et al. (2017) and Sweeney and Burnham (1990)). The model's choice must be supported by the best simultaneous fitting of the modelled vitrinite reflectance and temperature with the massive set of measured data. If a massive set is absent, models with different kinetics should be considered. An illustrative example of the difference in applying different kinetic models to evaluate maturity is presented in Nielsen et al. (2017). A comparison of the BasinRo model and the widely used EasyRo model shows that the EasyRo model can overestimate vitrinite reflectance in the interval of 0.5–1.7 %Ro by up to 0.35 %Ro (Nielsen et al., 2017).

Within the same field, and in identical environments, the Ro values often differ by 10–15%. One reason for this is the insufficient number of measurements at each microinclusion of vitrinite (e.g., 10–15 measurements instead of 100) (Kurchikov and Stavitsky, 1987). Another reason is the value of uncertainty in determining %Ro, depending on the method and equipment used. When measuring the reflectance of macerals, it is crucial to know what parameter of the vitrinite reflectance value is determined – minimal (R_{min}), maximal (R_{max}) or random (R_r) (ASTM D2798-20, 2020; 'GOST P 55659-2013,' 2015; ICCP, 1971). However, this is not often mentioned in publications. With the example of Upper Silesian coal,

Komorek and Morga (2002) demonstrated that the standard deviations in R_{max} and R_r are similar and do not exceed 0.05 %Ro for the range of maturity 0.2–0.9 %Ro. For maturities higher than 0.9 %Ro, the standard deviation increases and R_{max} becomes more precise than R_r (up to 0.13 %Ro, vs 0.33 %Ro); therefore, it serves as a more suitable rank indicator. The standard deviation of vitrinite reflectance measured for dispersed macerals in sedimentary rocks also increases with the advancing thermal maturity and increasing anisotropy of the organic matter. In Hackley et al. (2015), vitrinite reflectance for different types of organic matter (using the method in ASTM (2014) is demonstrated, wherein an increase in standard deviation from 0.04 to 0.19 %Ro in the range of 0.31–1.53 %Ro (without mentioning what method of Ro determination has been used) is observed. Houseknecht and Matthews (1985), using the example of R_r measurements of dispersed matter in carboniferous strata in the Ouachita Mountains, established that standard deviation $\sigma = 0.083+0.145*R_r$ (correlation coefficient = 0.808, number of samples = 89). Summarising the review above, for the measured values of vitrinite reflectance 0.45–0.72 %Ro (Figure 5b), a standard deviation in the range of 0.01–0.02 %Ro per Komorek and Morga (2002), 0.06–0.09 %Ro per Hackley et al. (2015) and 0.15–0.19 %Ro per Houseknecht and Matthews (1985) can be estimated.

The uncertainty in the indirect determination of %Ro (e.g., via the recalculation of T_{max} from pyrolysis data) includes the uncertainty in the pyrolysis measurement temperature (about ±2 °C with Hawk and Rock-Eval 6 tools according to Vtorushina et al. (2018) and Yang and Horsfield (2020)) and the uncertainty caused by the formula used for recalculation. For example, the widely used formula (see, e.g., Wust et al. (2013)) $\%Ro = 0.018*T_{max}-7.16$ by Jarvie et al. (2001) implies a standard deviation σ = 0.23 %Ro at N = 179 (N is the number of samples); i.e., the uncertainty is much higher than the previously described uncertainty resulting from direct measurements.

Uncertainty related to *formation temperature* includes the instrumental uncertainty of measurement and the uncertainty of the non-equilibrium formation temperature. The first depends on the equipment used; according to Blackwell and Spafford (1987), it is about ±0.5 °C for commercial temperature logs and ±0.05 °C for scientific equipment. The second is caused by uncertainty in undisturbed temperature measurements, as the

temperature readings in a well during drilling or completion do not reflect the equilibrium formation temperature (Hermanrud et al., 1990; Waples and Ramly, 2001), and the measured temperature values can be underestimated by up to ~22 °C, with standard deviation σ = 10 °C for depths of 500 to 9000 m (Förster, 2001; Gallardo and Blackwell, 1999). Various correction schemes have been presented and discussed in the literature (see, e.g., Peters and Nelson (2012) and Schumacher and Moeck (2020) and references therein); however, the uncertainty is rarely estimated. Förster has stated that the application of corrections improved 'a prediction of formation temperatures with an error less than ±10 °C at somewhat deeper depths than the log in several boreholes' (2001, p. 241).

Appendix B

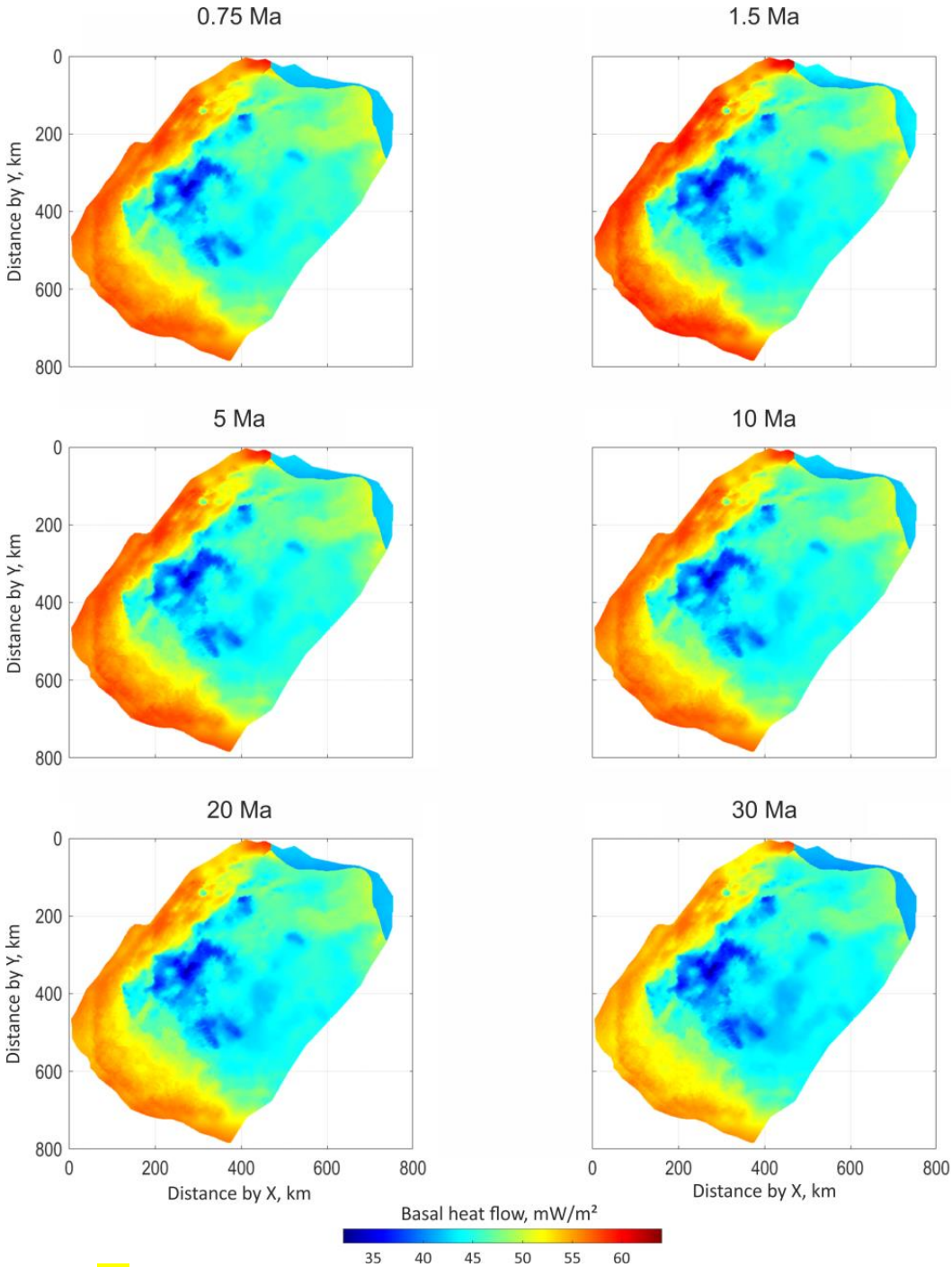

Figure 53. Basal heat flow maps were obtained by regressions for t_i 0.75 Ma, 1.5 Ma, 5 Ma, 10 Ma, 20 Ma, 30 Ma.

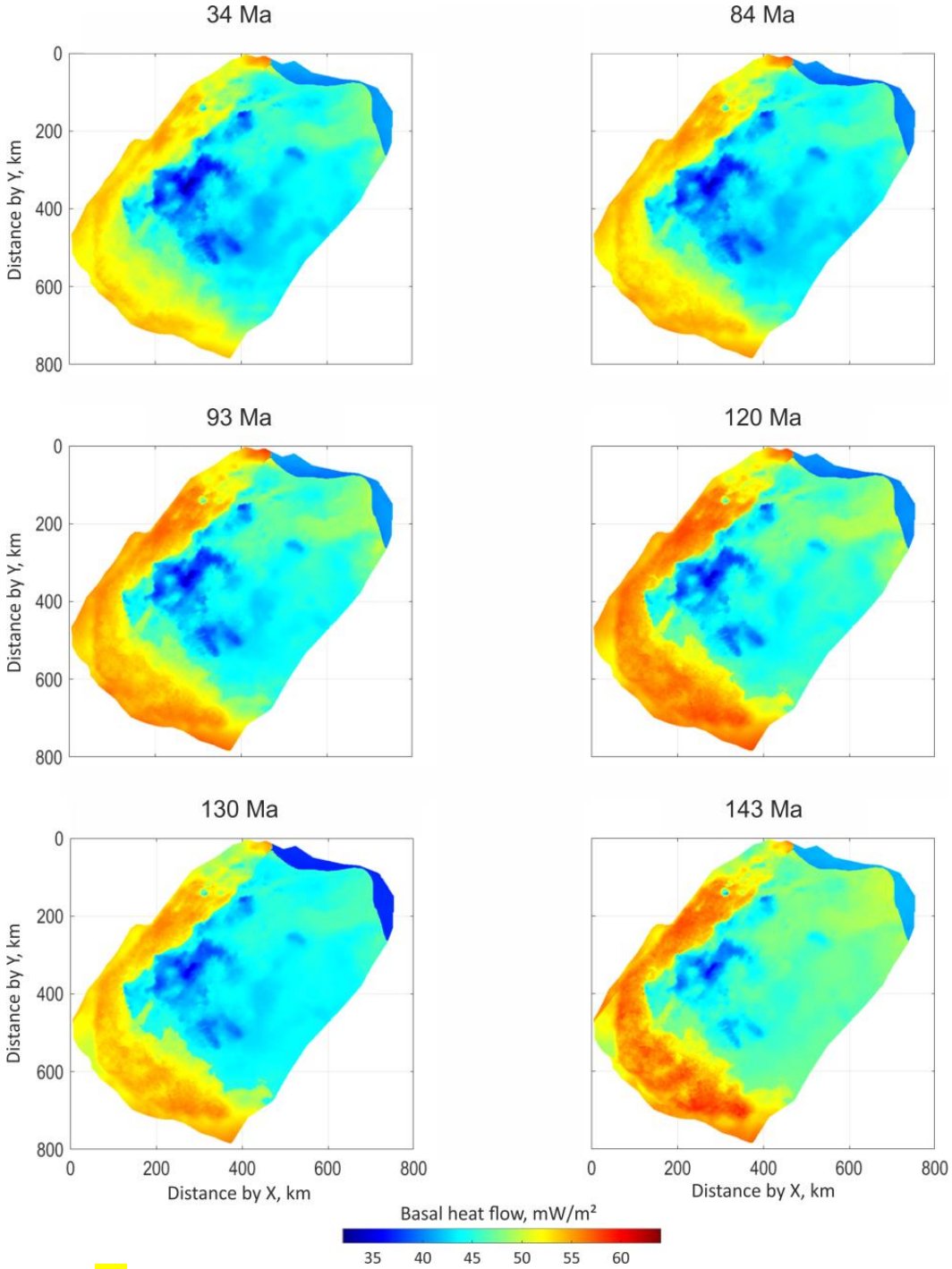

Figure 54. Basal heat flow maps were obtained by regressions for t_i 34 Ma, 84 Ma, 93 Ma, 120 Ma, 130 Ma, 143 Ma.

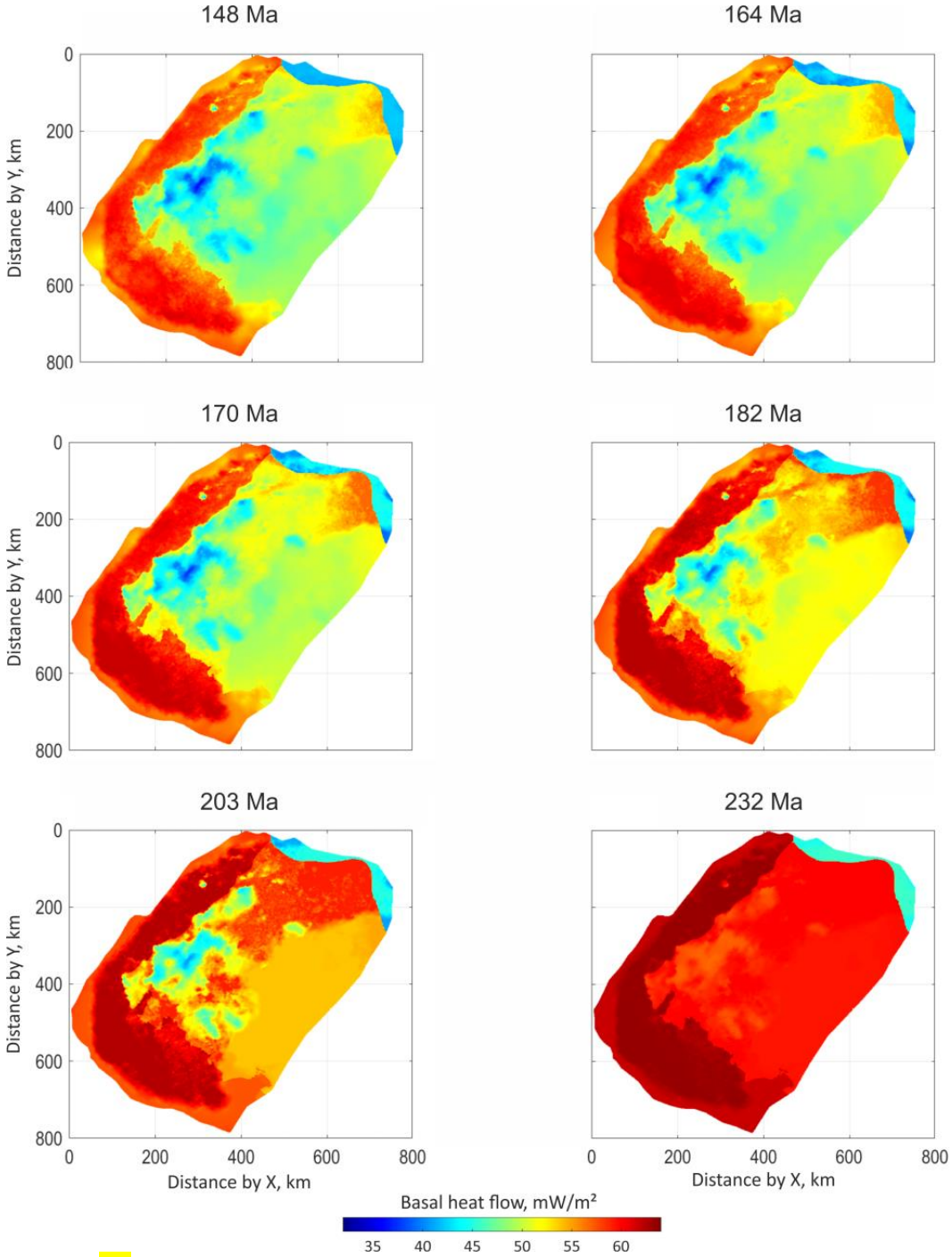

Figure 55. Basal heat flow maps were obtained by regressions for t_i 148 Ma, 164 Ma, 170 Ma, 182 Ma, 203 Ma, 232 Ma.

References

Abrehdary, M., 2016. Recovering Moho parameters using gravimetric and seismic data. Ph.D. Thesis, KTH RoyalInstitute of Technology, Stockholm, Sweden.

Abtout, A., Boukerbout, H., Bouyahiaoui, B., Gibert, D., 2014. Gravimetric evidences of active faults and underground structure of the Cheliff seismogenic basin (Algeria). Journal of African Earth Sciences 99, 363–373.

Airy, G.B., 1855. III. On the computation of the effect of the attraction of mountain-masses, as disturbing the apparent astronomical latitude of stations in geodetic surveys. Philosophical Transactions of the Royal Society of London 101–104.

Aitken, A.R.A., Salmon, M.L., Kennett, B.L.N., 2013. Australia's Moho: a test of the usefulness of gravity modelling for the determination of Moho depth. Tectonophysics 609, 468–479.

Al-Hajeri, M., Saeed, M., Derks, J., Fuchs, T., Hantschel, T., Kauerauf, A., Neumaier, M., Schenk, O., Swientek, O., Tessen, N., 2009. Basin and petroleum system modeling. Oilfield Rev. 21.

Allen, P.A., Allen, J.R., 2013. Basin analysis: Principles and application to petroleum play assessment, 3rd ed. John Wiley & Sons.

Archer, D., Martin, P., Buffett, B., Brovkin, V., Rahmstorf, S., Ganopolski, A., 2004. The importance of ocean temperature to global biogeochemistry. Earth and Planetary Science Letters 222, 333–348.

Artyushkov, Y. V, 1983. Mechanism of formation of geosynclinal belts. International Geology Review 25, 249–258.

Asaad, Y., 1955. A study of the thermal conductivity of fluid-bearing porous rocks. University of California, Berkeley.

ASTM, 2014. Standard Test Method for Microscopical Determination of the Reflectance of Vitrinite Dispersed in Sedimentary Rocks.

ASTM D2798-20, 2020. Standard Test Method for Microscopical Determination of the Vitrinite Reflectance of Coal. https://doi.org/10.1520/D2798-20

Athy, L.F., 1930. Density, porosity, and compaction of sedimentary rocks. AAPG Bulletin 14, 1–24. https://doi.org/10.1306/3D93289E-16B1-11D7-8645000102C1865D

Babushkin, A.E., Devyatov, V.P., Grigoryev, N. V., Gurari, F.G., Kazakov, A.M., Shatskiy, S.B., Surkov, V.S., 1995. West Siberia in late Maastrichtian, in: Surkov, V.S. (Ed.), Atlas of Paleotectonic and Paleogeographical- Landscape Maps of Hydrocarbon Provinces of Siberia. Petroconsultants S.A. IES, Geneva, Switzerland.

Barbier, F., Duvergé, J., Le Pichon, X., 1986. Structure profonde de la marge Nord-Gascogne. Implications sur le mécanisme de rifting et de formation de la marge continentale. Bulletin des centres de recherches exploration-Production Elf-Aquitaine 10, 105–121.

Batalin, O., Vafina, N., 2017. Condensation mechanism of hydrocarbon field formation. Scientific Reports 10253. https://doi.org/https ://doi. org/10.1038/s41598-017-10585-7

Baur, F., Hosford Scheirer, A., Peters, K.E., 2018. Past, present, and future of basin and petroleum system modeling. AAPG Bulletin 102, 549–561.

Blackbourn, G., 2014. The Palaeozoic of Western Siberia.

Blackwell, D.D., Spafford, R.E., 1987. 14. Experimental Methods in Continental Heat Flow, in: Methods in Experimental Physics. Elsevier, pp. 189–226.

Blackwell, D.D., Steele, J.L., 1989. Thermal conductivity of sedimentary rocks: measurement and significance, in: Thermal History of Sedimentary Basins. Springer, pp. 13–36.

Bogoyavlenskiy, V.I., Polyakova, I.D., 2012. Prospects for the oil and gas potential of large depths in the South Kara region. Arctic: Ecology and Economy 3(7), 92–103.

Bott, M.H.P., 1960. The use of rapid digital computing methods for direct gravity interpretation of sedimentary basins. Geophysical Journal International 3, 63–67.

Braitenberg, C., Ebbing, J., 2009. New insights into the basement structure of the West Siberian Basin from forward and inverse modeling of GRACE satellite gravity data. Journal of Geophysical Research: Solid Earth 114. https://doi.org/10.1029/2008JB005799

Braun, J., Beaumont, C., 1989. A physical explanation of the relation between flank uplifts and the breakup unconformity at rifted continental margins. Geology 17, 760–764.

Brune, S., Heine, C., Pérez-Gussinyé, M., Sobolev, S. V, 2014. Rift migration explains continental margin asymmetry and crustal hyper-extension. Nature Communications 5, 1–9.

Brune, S., Williams, S.E., Butterworth, N.P., Müller, R.D., 2016. Abrupt plate accelerations shape rifted continental margins. Nature 536, 201–204.

Chapin, D.A., 1996. The theory of the Bouguer gravity anomaly: A tutorial. The Leading Edge 15, 361–363. https://doi.org/10.1190/1.1437341

Chekhonin, E., Peshkov, G., Myasnikov, A., Rupke, L., Podladchikov, Y., Musikhin, K., Shuvaev, A., Bogdanov, O., Kostenko, O., Maglevannaya, P., 2017. Automated thermal history reconstruction of basin in West Siberia using 2D inverse modeling, in: Geomodel 2017. EAGE, Gelendzhik, Russia, pp. 1–6. https://doi.org/doi.org/10.3997/2214-4609.201702248

Chekhonin, E., Popov, Y., Peshkov, G., Spasennykh, M., Popov, E., Romushkevich, R., 2020. On the importance of rock thermal conductivity and heat flow density in basin and petroleum system modelling. Basin Research 32(5), 1271–1286. https://doi.org/10.1111/bre.12427

Cherepanova, Y., Artemieva, I.M., Chemia, Z., 2013. Crustal structure of the Siberian craton and the West Siberian basin: An appraisal of existing seismic data. Tectonophysics 609, 154–183. https://doi.org/10.1016/J.TECTO.2013.05.004

Christensen, N.I., Mooney, W.D., 1995. Seismic velocity structure and composition of the continental crust: A global view. Journal of Geophysical Research: Solid Earth 100, 9761–9788. https://doi.org/10.1029/95JB00259

Clark, S.A., Glorstad-Clark, E., Faleide, J.I., Schmid, D., Hartz, E.H., Fjeldskaar, W., 2014. Southwest Barents Sea rift basin evolution: comparing results from backstripping and timeforward modelling. Basin Research 26, 550–566. https://doi.org/10.1111/bre.12039

Clauser, C., Giese, P., Huenges, E., Kohl, T., Lehmann, H., Rybach, L., Šafanda, J., Wilhelm, H., Windloff, K., Zoth, G., 1997. The thermal regime of the crystalline continental crust: implications from the KTB. Journal of Geophysical Research: Solid Earth 102, 18417–18441.

Clauser, C., Huenges, E., 1995. Thermal conductivity of rocks and minerals. Rock physics and phase relations: a handbook of physical constants 3, 105–126.

Correia, A., Jones, F.W., 1996. On the importance of measuring thermal conductivities for heat flow density estimates: an example from the Jeanne d'Arc Basin, offshore eastern Canada. Tectonophysics 257, 71–80.

Cunha, T., 2015. When are rift models relevant for the petroleum system? The Petroleum System Blog, Technical discussions on petroluem system modeling [WWW Document]. URL http://petroleumsystem.blogspot.com/2015/02/when-are-rift-models-relevant-for_13.html

De Bremaecker, J.-C., 1983. Temperature, subsidence, and hydrocarbon maturation in extensional basins: a finite element model. AAPG Bulletin 67, 1410–1414.

Dewey, J.F., Bird, J.M., 1970. Mountain belts and the new global tectonics. Journal of Geophysical Research 75, 2625–2647.

Dietz, R.S., 1963. Collapsing continental rises: an actualistic concept of geosynclines and mountain building. The Journal of Geology 71, 314–333.

Dolzhenko, K. V., Safronov, P.I., Fomin, A.N., Melenevsky, V.N., 2017. The study of organic matter of the Bazhenov formation and modeling of hydrocarbon generation based on the Tyumen SG-6 well. Interexpo GEO-Sibir 2(1), 106–110.

Duchkov, A.D., Sokolova, L.S., Ayunov, D.E., 2017. Database of thermal properties of rocks of the Siberian region of the Russian Federation. INGG SB RAS.

Duchkov, A.D., Sokolova, L.S., Ayunov, D.E., Zlobina, O.N., 2013. Thermal conductivity of sediments in high-latitude West Siberia. Russian Geology and Geophysics 54, 1522–1528. https://doi.org/10.1016/j.rgg.2013.10.015

Duran, E., di Primio, R., Anka, Z., Stoddart, D., Horsfield, B., 2013a. 3D-basin modelling of the Hammerfest Basin (southwestern Barents Sea): A quantitative assessment of petroleum generation, migration and leakage. Marine and Petroleum Geology 45, 281–303. https://doi.org/10.1016/j.marpetgeo.2013.04.023

Duran, E., di Primio, R., Anka, Z., Stoddart, D., Horsfield, B., 2013b. Petroleum system analysis of the Hammerfest Basin (southwestern Barents Sea): Comparison of basin modelling and geochemical data. Organic Geochemistry 63, 105–121. https://doi.org/10.1016/j.orggeochem.2013.07.011

Emmermann, R., Lauterjung, J., 1997. The German continental deep drilling program KTB: overview and major results. Journal of Geophysical Research: Solid Earth 102, 18179–18201.

Eshagh, M., Bagherbandi, M., Sjöberg, L., 2011. A combined global Moho model based on seismic and gravimetric data. Acta Geodaetica et Geophysica Hungarica 46. https://doi.org/10.1556/AGeod.46.2011.1.3

Essa, K.S., 2012. A fast interpretation method for inverse modeling of residual gravity anomalies caused by simple geometry. Journal of Geological Research 2012. https://doi.org/10.1155/2012/327037

Faleide, J.I., Tsikalas, F., Breivik, A.J., Mjelde, R., Ritzmann, O., Engen, O., Wilson, J., Eldholm, O., 2008. Structure and evolution of the continental margin off Norway and the Barents Sea. Episodes 31, 82–91.

Fattah, R.A., Meekes, J.A.C., Colella, S., Bouman, J., Schmidt, M., Ebbing, J., 2013. The application of GOCE satellite gravity data for basin and petroleum system modeling: a case-study from the Arabian Peninsula. Search and Discovery Article 120130.

Fischer, K.M., Ford, H.A., Abt, D.L., Rychert, C.A., 2010. The lithosphere-asthenosphere boundary. Annual Review of Earth and Planetary Sciences 38, 551–575. https://doi.org/10.1146/annurev-earth-040809-152438

Fjeldskaar, W., Grunnaleite, I., Zweigel, J., Mjelde, R., Faleide, J.I., Wilson, J., 2009. Modelled palaeo-temperature on Vøring, offshore mid-Norway—The effect of the Lower Crustal Body. Tectonophysics 474, 544–558. https://doi.org/10.1016/j.tecto.2009.04.036

Fjeldskaar, W., Ter Voorde, M., Johansen, H., Christiansson, P., Faleide, J.I., Cloetingh, S., 2004. Numerical simulation of rifting in the northern Viking Graben: the mutual effect of modelling parameters. Tectonophysics 382, 189–212.

Fjellanger, E., Kontorovich, A.E., Barboza, S.A., Burshtein, L.M., Hardy, M.J., Livshits, V.R., 2010. Charging the giant gas fields of the NW Siberia basin, in: Geological Society, London, Petroleum Geology Conference Series. Geological Society of London, pp. 659–668. https://doi.org/10.1144/0070659

Fomin, A.N., Kontorovich, A.E., Krasavchikov, V.O., 2001. Catagenesis of organic matter and petroleum potential of the Jurassic, Triassic, and Paleozoic deposits in the northern areas of the West Siberian megabasin. GEOLOGIYA I GEOFIZIKA 42, 1875–1887.

Fonkin, V.E., 1996. The experience of the mass studies of the core of the Tyumen super deep well, in: Mazur, V. (Ed.), Tyumen Super Deep Well (Interval 0–7502 m). Results of Drilling and Study. KamNIIKIGS, Perm, Russia, pp. 70–79.

Förster, A., 2001. Analysis of borehole temperature data in the Northeast German Basin: continuous logs versus bottom-hole temperatures. Petroleum Geoscience 7, 241–254. https://doi.org/10.1144/petgeo.7.3.241

Franke, D., 2013. Rifting, lithosphere breakup and volcanism: Comparison of magma-poor and volcanic rifted margins. Marine and Petroleum geology 43, 63–87.

Fuchs, S., Balling, N., 2016. Improving the temperature predictions of subsurface thermal models by using high-quality input data. Part 2: A case study from the Danish-German border region. Geothermics 64, 1–14.

Fuchs, S., Balling, N., Förster, A., 2015. Calculation of thermal conductivity, thermal diffusivity and specific heat capacity of sedimentary rocks using petrophysical well logs. Geophysical Journal International 203, 1977–2000.

Funnell, R., Chapman, D., Allis, R., Armstrong, P., 1996. Thermal state of the Taranaki basin, New Zealand. Journal of Geophysical Research: Solid Earth 101, 25197–25215.

Gac, S., Hansford, P.A., Faleide, J.I., 2018. Basin modelling of the SW Barents Sea. Marine and Petroleum Geology 95, 167–187. https://doi.org/10.1016/j.marpetgeo.2018.04.022

Gallagher, K., Morrow, D.W., 1998. A novel approach for constraining heat flow histories in sedimentary basins. Geological Society, London, Special Publications 141, 223–239.

Gallardo, J., Blackwell, D.D., 1999. Thermal structure of the Anadarko Basin. AAPG bulletin 83, 333–361. https://doi.org/10.1306/00AA9A84-1730-11D7-8645000102C1865D

Galushkin, Y., 2016. Non-standard Problems in Basin Modelling. Springer.

Galushkin, Y., 1997. Numerical simulation of permafrost evolution as a part of sedimentary basin modeling: permafrost in the Pliocene–Holocene climate history of the Urengoy field in the West Siberian basin. Canadian Journal of Earth Sciences 34, 935–948.

Galushkin, Y., Simonenkova, O., Lopatin, N., 1999. Thermal and Maturation Modeling of the Urengoy Field, West Siberian Basin: Some Special Considerations in Basin Modeling1. AAPG bulletin 83, 1965–1979.

Galushkin, Y.I., 2007. Sedimentary basin modeling and estimation of its hydrocarbon potential. Nauchnyi mir, Moscow.

Galushkin, Y.I., Lopatin, N. V., Emets, T.P., 1996. Numerical modeling of the evolution of the catagenesis of the Jurassic and Triassic deposits, in: Mazur, V.B. (Ed.),

Tyumen Super Deep Well (Interval 0–7502 m). Results of Drilling and Study. KamNIIKIGS, Perm, Russia, pp. 279–286.
Galushkin, Y.I., Sitar, K.A., Kunitsyna, A. V, 2009. Deep subsidence of the early catagenesis zones of organic matter in the sedimentary rocks of Northeastern Sakhalin shelf at high thermal regime of the basin, in: Doklady Earth Sciences. Springer Nature BV, p. 444.
GOST P 55659-2013, 2015. . (ISO 7404-5:2009) Methods for the petrographic analysis of coals. Part 5: Method of determining the reflectance of vitrinite 2015 microscopically.
Gravimetric map of the Ural federal district [WWW Document], 2019. . Package of operational geological information (GIS Atlas), VSEGEI. URL https://vsegei.ru/ru/info/gisatlas/ufo/okrug/f_22_gravika.jpg (accessed 7.29.21).
Gvirtzman, Z., Faccenna, C., Becker, T.W., 2016. Isostasy, flexure, and dynamic topography. Tectonophysics 683, 255–271.
Hackley, P.C., Araujo, C.V., Borrego, A.G., Bouzinos, A., Cardott, B.J., Cook, A.C., Eble, C., Flores, D., Gentzis, T., Gonçalves, P.A., 2015. Standardization of reflectance measurements in dispersed organic matter: Results of an exercise to improve interlaboratory agreement. Marine and Petroleum Geology 59, 22–34. https://doi.org/10.1016/j.marpetgeo.2014.07.015
Haines, H.H., 1982. Thermal expansion and compressibility of rocks as a function of pressure and temperature. Massachusetts Institute of Technology.
Hansford, P.A., 2014. Basin modelling of the south-west Barents Sea. Master Thesis, Department of Geosciences. University of Oslo.
Hantschel, T., Kauerauf, A.I., 2009. Fundamentals of basin and petroleum systems modeling. Springer Science & Business Media.
Heiland, C.A., 1940. Geophysical exploration, Co., New York. Prentice Hall Inc.
Hellinger, J.S., Sclater, G.J., 1983. Some Comments on Two-Layer Extensional Models for the Evolution of Sedimentary Basins, Journal of Geophysical Research. https://doi.org/10.1029/JB088iB10p08251
Hermanrud, C., Cao, S., Lerche, I., 1990. Estimates of virgin rock temperature derived from BHT measurements: bias and error. Geophysics 55, 924–931. https://doi.org/10.1190/1.1442908
Hicks, P.J.J., Fraticelli, C.M., Shosa, J.D., Hardy, M.J., Townsley, M.B., 2012. Identifying and quantifying significant uncertainties in basin modeling. https://doi.org/10.1306/13311437H41527
Houseknecht, D., Matthews, S., 1985. Thermal maturity of Carboniferous strata, Ouachita Mountains. AAPG Bulletin 69. https://doi.org/10.1306/AD4624E3-16F7-11D7-8645000102C1865D
ICCP, 1971. (International Committee for Coal Petrology ICCP), Supp. 2nd ed. Centre Nat. de la Rech. Sci., Paris.
Isaev, V.I., Gulenok, R.Y., Isaeva, O.S., Lobova, G.A., 2008. Density modeling of the basement of sedimentary sequences and prediction of oil-gas accumulations: Evidence from South Sakhalin and West Siberia. Russian Journal of Pacific Geology 2, 191–204. https://doi.org/10.1134/S1819714008030019
Isaev, V.I., Rylova, T.B., Gumerova, A.A., 2014. Paleoclimate of Western Siberia and Realization of the Generation Potential of Oil Source Deposits. Bulletin of Tomsk Polytechnic University 324.
Ivanov, K.S., Koroteev, V.A., Pecherkin, M.F., Fedorov, Y.N., Erokhin, Y. V, 2009. The western part of the West Siberian petroleum megabasin: geologic history and

structure of the basement. Russian Geology and Geophysics 50, 365–379. https://doi.org/10.1016/j.rgg.2009.03.010
Jacoby, W., Smilde, P.L., 2009. Gravity interpretation: fundamentals and application of gravity inversion and geological interpretation. Springer Science & Business Media.
Jarvie, D.M., Claxton, B.L., Henk, F., Breyer, J.T., 2001. Oil and shale gas from the Barnett Shale, Ft, in: Worth Basin, Texas (Abs.): AAPG Annual Meeting Program. p. A100.
Jarvis, T.G., McKenzie, D., 1980. Sedimentary basin formation with finite extension rate, Earth and Planetary Science Letters. https://doi.org/10.1016/0012-821X(80)90168-5
Jaupart, C., 1986. On the average amount and vertical distribution of radioactivity in the continental crust, in: Thermal Modelling in Sedimentary Basins. Editions Technip Paris, pp. 33–47.
Kanthiya, S., Mangkhemthong, N., Morley, C.K., 2019. Structural interpretation of Mae Suai Basin, Chiang Rai Province, based on gravity data analysis and modelling, in: Asia International Multidisciplinary Conference. Elsevier, pp. 237–246. https://doi.org/10.1016/j.heliyon.2019.e01232
Karaseva, T. V., Gorbachev, V.I., Keller, M.B., Ponamorev, V.A., 1996. The main scientific results of the study of the Tyumen Superdeep Well, in: Mazur, V. (Ed.), Tyumen Super Deep Well (Interval 0–7502 m). Results of Drilling and Study 0–7502 m). Results of Drilling and Study. KamNIIKIGS, Perm, Russia, pp. 49–62.
Kaus, B.J.P., Connolly, J.A.D., Podladchikov, Y.Y., Schmalholz, S.M., 2005. Effect of mineral phase transitions on sedimentary basin subsidence and uplift. Earth and Planetary Science Letters 233, 213–228.
Kazanenkova, A., 2015. Some Aspects of Petroleum System Modeling in the North-Eastern Part of West Siberia Basin, in: Tyumen 2015-Deep Subsoil and Science Horizons. European Association of Geoscientists & Engineers, pp. 1–5.
Keen, C.E., Loncarevic, B.D., Reid, I., Woodside, J., Haworth, R.T., Williams, H., 1990. Tectonic and geophysical overview, in: Keen, M.J., Williams, G.L. (Eds.), Geology of the Continental Margin of Eastern Canada: Geol. Survey Canada. Geology of Canada, pp. 31–85.
Khmelevskoy, V.K., Gorbachev, Y.I., Kalinin, A. V, Popov, M.G., Seliverstov, N.I., Shevnin, V.A., 2004. Geophysical research methods. Textbook for geological specialties of universities. KGPU, Petropavlovsk-Kamchatsky.
Kingston, D.R., Dishroon, C.P., Williams, P.A., 1983. Global basin classification system. AAPG bulletin 67, 2175–2193.
Klitzke, P., Faleide, J.I., Scheck-Wenderoth, M., Sippel, J., 2015. A lithosphere-scale structural model of the Barents Sea and Kara Sea region. Solid Earth 6, 153–172. https://doi.org/10.5194/se-6-153-2015
Klitzke, P., Sippel, J., Faleide, J.I., Scheck-Wenderoth, M., 2016. A 3D gravity and thermal model for the Barents Sea and Kara Sea. Tectonophysics 684, 131–147. https://doi.org/10.1016/j.tecto.2016.04.033
Komorek, J., Morga, R., 2002. Relationship between the maximum and the random reflectance of vitrinite for coal from the Upper Silesian Coal Basin (Poland). Fuel 81, 969–971. https://doi.org/10.1016/S0016-2361(01)00181-8
Konstantinovskaya, E., 2004. Collision and extension at continental margins: Example of the Sea of Okhotsk, in: American Geophysical Union 2004 Fall Meeting, San Francisco, California, USA.

Kontorovich, A.E., Kontorovich, V.A., Ryzhkova, S. V, Shurygin, B.N., Vakulenko, L.G., Gaideburova, E.A., Danilova, V.P., Kazanenkov, V.A., Kim, N.S., Kostyreva, E.A., 2013. Jurassic paleogeography of the West Siberian sedimentary basin. Russian geology and geophysics 54, 747–779.

Kooi, H., Cloetingh, S., Burrus, J., 1992. Lithospheric necking and regional isostasy at extensional basins 1. Subsidence and gravity modeling with an application to the Gulf of Lions margin (SE France). Journal of Geophysical Research: Solid Earth 97, 17553–17571.

Krovushkina, O.A., 2001. Structure and Petroleum Prospectivity of the Magadan Sedimentary Basin. Geologiya Nefti Gaza.

Kukkonen, I.T., Jokinen, J., Seipold, U., 1999. Temperature and pressure dependencies of thermal transport properties of rocks: implications for uncertainties in thermal lithosphere models and new laboratory measurements of high-grade rocks in the central Fennoscandian shield. Surveys in Geophysics 20, 33–59.

Kukkonen, I.T., Rath, V., Kivekäs, L., Šafanda, J., Čermak, V., 2011. Geothermal studies of the Outokumpu Deep Drill Hole, Finland: Vertical variation in heat flow and palaeoclimatic implications. Physics of the Earth and Planetary Interiors 188, 9–25.

Kurchikov, A.R., 2001. The geothermal regime of hydrocarbon pools in West Siberia. Geology and Geophysic 42, 1846–1853.

Kurchikov, A.R., Stavitsky, B., 1987. Geothermy of oil and gas bearing areas of Western Siberia.

Kusznir, N.J., Marsden, G., Egan, S.S., 1991. A flexural-cantilever simple-shear/pure-shear model of continental lithosphere extension: applications to the Jeanne d'Arc Basin, Grand Banks and Viking Graben, North Sea. Geological Society, London, Special Publications 56, 41–60.

Kusznir, N.J., Park, R.G., 1987. The extensional strength of the continental lithosphere: its dependence on geothermal gradient, and crustal composition and thickness. Geological Society, London, Special Publications 28, 35–52.

Kusznir, N.J., Ziegler, P.A., 1992. The mechanics of continental extension and sedimentary basin formation: a simple-shear/pure-shear flexural cantilever model. Tectonophysics 215, 117–131.

Lachenbruch, A.H., 1970. Crustal temperature and heat production: Implications of the linear heat-flow relation. Journal of Geophysical Research 75, 3291–3300.

Lachenbruch, A.H., 1968. Preliminary geothermal model of the Sierra Nevada. Journal of Geophysical Research 73, 6977–6989. https://doi.org/10.1029/JB073i022p06977

LaFehr, T.R., 1991. Standardization in gravity reduction. GEOPHYSICS 56, 1170–1178. https://doi.org/10.1190/1.1443137

Larsen, H.C., Mohn, G., Nirrengarten, M., Sun, Z., Stock, J., Jian, Z., Klaus, A., Alvarez-Zarikian, C.A., Boaga, J., Bowden, S.A., 2018. Rapid transition from continental breakup to igneous oceanic crust in the South China Sea. Nature Geoscience 11, 782–789.

Lee, E.Y., Novotny, J., Wagreich, M., 2018. Subsidence Analysis and Visualization: For Sedimentary Basin Analysis and Modelling. Springer.

Lee, Y., Deming, D., 1998. Evaluation of thermal conductivity temperature corrections applied in terrestrial heat flow studies. Journal of Geophysical Research: Solid Earth 103, 2447–2454.

Lichteneker, K., 1926. The thermal conductivity of granular materials. Physikalische Zc 27, 115–118.

Lomtev, V.L., Patrikeev, V.N., Gurinov, M.G., 2009. New data on the structure of the Sea of Okhotsk bottom. Russian Journal of Pacific Geology 3, 201–209.

Lucazeau, F., Le Douaran, S., 1985. The blanketing effect of sediments in basins formed by extension: a numerical model. Application to the Gulf of Lion and Viking graben. Earth and Planetary Science Letters 74(1), 92–102. https://doi.org/10.1016/0012-821X(85)90169-4

Map of Jurassic formations: P-42 (Khanty-Mansiysk) [WWW Document], 2009. State geological map of the Russian Federation. Third generation. West Siberian Series. Map of Jurassic formations lying on the foundation (bottom view), scale: 1: 1000000, series: West Siberian, compiled by: Geotex LLC, FSGBI "VSEGEI", editor: Kovrigina. URL http://www.geokniga.org/maps/7131 (accessed 7.29.21).

Map of Jurassic formations: P-43 (Surgut) [WWW Document], 2010. State geological map of the Russian Federation. Third generation. Geological map of Jurassic formations lying on the foundation (bottom view). West Siberian series, scale: 1: 1000000, series: West Siberian, compiled by: FSBI "VSEGEI", FSUE ZapSibNIIIGG,. URL http://www.geokniga.org/maps/7936 (accessed 7.29.21).

Martyshko, P.S., Ladovskii, I. V, Byzov, D.D., Tsidaev, A.G., 2018. Gravity data inversion with method of local corrections for finite elements models. Geosciences 8, 373. https://doi.org/10.3390/geosciences8100373

Matava, T., Matt, V., Flannery, J., 2019. New insights on measured and calculated vitrinite reflectance. Basin Research 31, 213–227.

Maystrenko, Y.P., Gernigon, L., Olesen, O., Ottesen, D., Rise, L., 2018. 3-D thermal effect of late Cenozoic erosion and deposition within the Lofoten–Vesterålen segment of the Mid-Norwegian continental margin. Geophysical Journal International 213, 885–918. https://doi.org/10.1093/gji/ggy013

McKenzie, D., 1978. Some remarks on the development of sedimentary basins. Earth and Planetary Science Letters 40, 25–32. https://doi.org/10.1016/0012-821X(78)90071-7

McKenzie, D.P., 1967. Some remarks on heat flow and gravity anomalies. Journal of Geophysical Research 72, 6261–6273.

Merkulov, V.P., Volkova, A.A., Grigoriev, G.S., 2019. The Using of 3D Modeling for Processing Gravimetric Data in the Study of Oil and Gas Deposits of the Pre-Jurassic Complex of Western Siberia, in: Geomodel 2019. European Association of Geoscientists & Engineers, pp. 1–5. https://doi.org/10.3997/2214-4609.201950094

Meshalkin, Y., Shakirov, A., Popov, E., Koroteev, D., Gurbatova, I., 2020. Robust well-log based determination of rock thermal conductivity through machine learning. Geophysical Journal International 222, 978–988. https://doi.org/10.1093/gji/ggaa209

Midttømme, K., Roaldset, E., 1999. Thermal conductivity of sedimentary rocks: uncertainties in measurement and modelling. Geological Society, London, Special Publications 158, 45–60.

Mienert, J., Vanneste, M., Bünz, S., Andreassen, K., Haflidason, H., Sejrup, H.P., 2005. Ocean warming and gas hydrate stability on the mid-Norwegian margin at the Storegga Slide. Marine and Petroleum Geology 22, 233–244.

Minakov, A., Mjelde, R., Faleide, J.I., Flueh, E.R., Dannowski, A., Keers, H., 2012. Mafic intrusions east of Svalbard imaged by active-source seismic tomography. Tectonophysics 518–521, 106–118. https://doi.org/10.1016/j.tecto.2011.11.015

Mohammedyasin, S.M., Lippard, S.J., Omosanya, K.O., Johansen, S.E., Harishidayat, D.,

2016. Deep-seated faults and hydrocarbon leakage in the Snøhvit Gas Field, Hammerfest Basin, Southwestern Barents Sea. Marine and Petroleum Geology 77, 160–178. https://doi.org/10.1016/j.marpetgeo.2016.06.011

Morelli, C., Gantar, C., McConnell, R.K., Szabo, B., Uotila, U., 1972. The international gravity standardization net 1971 (IGSN 71). OSSERVATORIO GEOFISICO SPERIMENTALE TRIESTE (ITALY).

Morozov, N., Belenkaya, I., Kasyanenko, A., Bodryagin, S., 2016. Evaluation of the Resource Potential Based on 3D Basin Modeling of Bagenov Fm. Hydrocarbon System, in: SPE Russian Petroleum Technology Conference and Exhibition. Society of Petroleum Engineers. https://doi.org/10.2118/182073-MS

Myasnikov, A., Podladchikov, Y., Yu. A., P., 2015. Reduction of Thermal Evolution Uncertainties in Modeling of Hydrocarbons Maturation, in: Geomodel 2015 - 17th Scientific-Practical Conference on Oil and Gas Geological Exploration and Development. Gelendzhik.

Nakiboglu, S.M., Lambeck, K., 1985. Comments on thermal isostasy. Journal of geodynamics 2, 51–65.

Newman, R., White, N., 1997. Rheology of the continental lithosphere inferred from sedimentary basins. Nature 385, 621–624.

Nezhdanov, A.A., Ogibenin, V. V, Melnikova, M. V, Smirnov, A.S., 2014. STRUCTURES AND STRATIFICATION OF THE TRIASSIC-JURASSIC FORMATIONS IN THE NORTHERN PART OF WESTERN SIBERIA. ROGTEC 14–23.

Nielsen, S.B., Clausen, O.R., McGregor, E., 2017. Basin%Ro: A vitrinite reflectance model derived from basin and laboratory data. Basin Research 29, 515–536. https://doi.org/10.1111/bre.12160

Nikishin, A.M., Freiman, S.I., Zhukov, N.N., Startseva, K., Petrov, E.I., Morozov, A.F., Cloetingh, S., Malyshev, N.A., Verzhbitsky, V.E., Posamentier, H.W., 2019. Geological structure and history of the Arctic Ocean based on new geophysical data: Implications for paleoenvironment and paleoclimate. Part 2. Mesozoic to Cenozoic geological evolution. Earth-Science Reviews 103034.

Nikishin, A.M., Ziegler, P.A., Abbott, D., Brunet, M.-F., Cloetingh, S., 2002. Permo–Triassic intraplate magmatism and rifting in Eurasia: implications for mantle plumes and mantle dynamics. Tectonophysics 351, 3–39. https://doi.org/10.1016/S0040-1951(02)00123-3

Norden, B., Förster, A., Förster, H.-J., Fuchs, S., 2020. Temperature and pressure corrections applied to rock thermal conductivity: impact on subsurface temperature prognosis and heat-flow determination in geothermal exploration. Geothermal Energy 8, 1–19. https://doi.org/10.1186/s40517-020-0157-0

Norris, S., Kusznir, N.J., 1993. 3-D reverse modelling of post-rift extensional basins. Terra Nova 5, 173–174.

Norwegian Petroleum Directorate [WWW Document], n.d. URL https://www.npd.no

Ognev, A.F., Kupriyanov, M.Y., Ivanchik, A.A., 2019. Wave cyclicity of tectonic and sedimentation processes and its role in the formation of unique gas deposits of the North Yamal and the Yamal shelf of the Kara Sea. Gas industry 780.

Ohm, S.E., Karlsen, D.A., Austin, T.J.F., 2008. Geochemically driven exploration models in uplifted areas: Examples from the Norwegian Barents Sea. AAPG Bulletin 92, 1191–1223. https://doi.org/10.1306/06180808028

Oilfield Glossary, Schlumberger, 2021. . Oilfield Glossary, Schlumberger.

Ostanin, I., Anka, Z., di Primio, R., 2017. Role of Faults in Hydrocarbon Leakage in the

Hammerfest Basin, SW Barents Sea: Insights from Seismic Data and Numerical Modelling. Geosciences 7, 28. https://doi.org/10.3390/geosciences7020028
Pallero, J.L.G., Fernández-Martínez, J.L., Bonvalot, S., Fudym, O., 2017. 3D gravity inversion and uncertainty assessment of basement relief via particle swarm optimization. Journal of Applied Geophysics 139, 338–350.
Parsons, B., Sclater, J.G., 1977. An analysis of the variation of ocean floor bathymetry and heat flow with age. Journal of geophysical research 82, 803–827.
Pasquale, V., Chiozzi, P., Verdoya, M., Gola, G., 2012. Heat flow in the Western Po Basin and the surrounding orogenic belts. Geophysical Journal International 190, 8–22.
Peron-Pinvidic, G., Manatschal, G., Osmundsen, P.T., 2013. Structural comparison of archetypal Atlantic rifted margins: A review of observations and concepts. Marine and Petroleum Geology 43, 21–47.
Peshkov, G., Chekhonin, E., Pissarenko, D., 2019. Thermal History Reconstruction of the Sedimentary Basin by Inverse Modeling on the Example of CDP 1632 of the Okhotsk Sea, in: Far East Hydrocarbons 2019. European Association of Geoscientists & Engineers, pp. 1–4.
Peshkov, G.A., Chekhonin, E.M., Rüpke, L.H., Musikhin, K.A., Bogdanov, O.A., Myasnikov, A. V., 2021a. Impact of differing heat flow solutions on hydrocarbon generation predictions: A case study from West Siberian Basin. Marine and Petroleum Geology 124. https://doi.org/10.1016/j.marpetgeo.2020.104807
Peshkov, G.A., Khakimova, L., Grishko, E., Wangen, M., Yarushina, V., 2021b. Coupled basin and hydro-mechanical modeling of gas chimney formation: the SW Barents Sea. Energies.
Peshkov, Ibragimov, I., Yarushina, V., Myasnikov, A., 2020. Basin modelling as a predictive tool for potential zones of chimney presence, in: EGU General Assembly Conference Abstracts. p. 18689.
Peters, K.E., Nelson, P.H., 2012. Criteria to determine borehole formation temperatures for calibration of basin and petroleum system models. SEPM Special Publication 103, 5–15.
Peters, K.E., Schenk, O., Scheirer, A.H., Wygrala, B., Hantschel, T., 2017. Basin and petroleum system modeling, in: Springer Handbook of Petroleum Technology. Springer, pp. 381–417.
Petrishchevsky, A.M., 2016. Rheological and geothermal features of the Okhotsk Sea Plume. Bulletin of the Tomsk Polytechnic University. Engineering of Georesources 327, 65–76.
Podladchikov, Y.Y., Poliakov, A.N.B., Yuen, D.A., 1994. The effect of lithospheric phase transitions on subsidence of extending continental lithosphere. Earth and Planetary Science Letters 124, 95–103.
Poplavskii, K.N., Podladchikov, Y.Y., Stephenson, R.A., 2001. Two-dimensional inverse modeling of sedimentary basin subsidence. Journal of Geophysical Research: Solid Earth 106, 6657–6671. https://doi.org/10.1029/1999JB900211
Popov, E.Y., Goncharov, A., Popov, Y.A., Spasennykh, M., Chekhonin, E., Shakirov, A., Gabova, A., 2019. Advanced techniques for determining thermal properties on rock samples and cuttings and indirect estimating for atmospheric and formation conditions, in: IOP Conference Series: Earth and Environmental Science. IOP Publishing, p. 12017.
Popov, E.Y., Romushkevich, R.A., Popov, Y.A., 2017. Measurements of the Rock Thermal Properties on the Standard Core Plugs As a Necessary Stage of the

Thermalphysic Investigations of the Hydrocarbon Fields. Proceedings of Higher Educational Establishments. Geology and Exploration 2, 56–70.
Popov, Y.A., Beardsmore, G., Clauser, C., Roy, S., 2016. ISRM suggested methods for determining thermal properties of rocks from laboratory tests at atmospheric pressure. Rock Mechanics and Rock Engineering 49, 4179–4207.
Popov, Y.A., Chekhonin, E., Parshin, A., Popov, E., Miklashevskiy, D., 2013. New hardware and methodological base of thermal petrophysics as a means of increasing the efficiency of heavy oil production. Oil. Gas. Innovations. 52–58.
Popov, Y.A., Parshin, A., Ursegov, S., Taraskin, E., Chekhonin, E., Andrianov, N., Bayuk, I., Pimenov, V., 2012. Thermal reservoir simulation: Thermal property data uncertainties and their influence on simulation results, in: WHOC12-291, World Heavy Oil Congress, Aberdeen, UK, September. pp. 10–13.
Popov, Y.A., Popov, E.Y., Chekhonin, E., Spasennykh, M., Goncharov, A., 2019. Evolution in information on crustal geothermal parameters due to application of advanced experimental basis, in: IOP Conference Series: Earth and Environmental Science. IOP Publishing, p. 12042.
Popov, Y.A., Popov, E.Y., Miklashevskiy, D., Korobkov, D.A., 2014. New thermal data and challenges of heat flow variations evaluation for basin petroleum exploration, in: International Petroleum Technology Conference. International Petroleum Technology Conference.
Popov, Y.A., Romushkevich, R.A., Popov, E.Y., 1996. Thermophysical studies of the rocks in the Tyumen super deep well, in: Mazur, V.B. (Ed.), Tyumen Super Deep Well (Interval 0–7502 m). Results of Drilling and Study. KamNIIKIGS, Perm, Russia.
Popov, Y.A., Spasennykh, M., Valiullin, R., Yarullin, R., Ramazanov, A., Zagranovskaya, D., Zakharova, O., Golovanova, I., 2018. First Experience of Maintenance of Basin Modeling With Up-to-date Complex of Experimental Geothermic Investigations, in: Geomodel 2018. European Association of Geoscientists & Engineers, pp. 1–5.
Pratt, J.H., 1855. I. On the attraction of the Himalaya Mountains, and of the elevated regions beyond them, upon the plumb-line in India. Philosophical Transactions of the Royal Society of London 53–100.
Radziamir, M., Noh, K., Ghani Rafek, A., Rafek, B., Yoong, A., Zakariah, M.N.A., 2019. Gravity Modelling Of The Crystalline Basement At Pekan, Pahang River Delta, in: The European Proceedings of Social & Behavioural Sciences. Future Academy, pp. 237–246. https://doi.org/10.15405/epsbs.2019.05.02.23
Ranero, C.R., Pérez-Gussinyé, M., 2010. Sequential faulting explains the asymmetry and extension discrepancy of conjugate margins. Nature 468, 294–299.
Reemst, P., Cloetingh, S., Fanavoll, S., 1994. Tectonostratigraphic modelling of Cenozoic uplift and erosion in the south-western Barents Sea. Marine and Petroleum Geology 11, 478–490. https://doi.org/10.1016/0264-8172(94)90081-7
Roberts, A.M., Kusznir, N.J., Corfield, R.I., Thompson, M., Woodfine, R., 2013. Integrated tectonic basin modelling as an aid to understanding deep-water rifted continental margin structure and location. Petroleum Geoscience 19, 65–88.
Robertson, E.C., 1988. Thermal properties of rocks. U.S. Geological Survey. https://doi.org/10.3133/ofr88441
Romanov, A.G., Goncharov, I. V, Gagarin, A.N., Carruthers, D.J., Corbett, P.W.M., Ryazanov, A. V, 2005. 3D Modelling of the Hydrocarbon Migration in the Jurassic Petroleum System in Part of the West Siberia Basin, in: Canadian International

Petroleum Conference. Petroleum Society of Canada. https://doi.org/10.2118/2005-086-EA
Royden, L.H., Keen, C.E., 1980. Rifting process and thermal evolution of the continental margin of Eastern Canada determined from subsidence curves, Earth and Planetary Science Letters. https://doi.org/10.1016/0012-821X(80)90216-2
Rüpke, L.H., Schmalholz, S.M., Schmid, D.W., Podladchikov, Y.Y., 2008. Automated thermotectonostratigraphic basin reconstruction: Viking Graben case study. AAPG Bulletin 92, 309–326. https://doi.org/10.1306/11140707009
Rüpke, L.H., Schmid, D.W., Perez-Gussinye, M., Hartz, E., 2013. Interrelation between rifting, faulting, sedimentation, and mantle serpentinization during continental margin formation—including examples from the Norwegian Sea. Geochemistry, Geophysics, Geosystems 14, 4351–4369. https://doi.org/10.1002/ggge.20268
Safronov, P.I., Ershov, S. V, Kim, N.S., Fomin, A.N., 2011. Modeling of processes of generation, migration and accumulation of hydrocarbons in the Jurassic and Cretaceous complexes of the Yenisei-Khatanga Basin. Oil and gas geology 48–55.
Saltus, R., Morin, R., Phillips, J., Webring, M., 1999. Gravity data processing, modeling, and interpretation in support of structural studies in the northern part of the Arctic national wildlife refuge, Alaska, in: The Oil and Gas Resource Potential of the 1002 Area, Arctic National Wildlife Refuge, Alaska. USGS Open-File Report.
Sass, J.H., Lachenbruch, A.H., Moses Jr, T.H., Morgan, P., 1992. Heat flow from a scientific research well at Cajon Pass, California. Journal of Geophysical Research: Solid Earth 97, 5017–5030.
Saunders, A.D., England, R.W., Reichow, M.K., White, R. V, 2005. A mantle plume origin for the Siberian traps: uplift and extension in the West Siberian Basin, Russia. Lithos 79, 407–424.
Scheck-Wenderoth, M., Maystrenko, Y., 2008. How warm are passive continental margins? A 3-D lithosphere-scale study from the Norwegian margin. Geology 36, 419–422. https://doi.org/10.1130/G24545A.1
Scheck-Wenderoth, M., Raum, T., Faleide, J.I., Mjelde, R., Horsfield, B., 2007. The transition from the continent to the ocean: a deeper view on the Norwegian margin. Journal of the Geological Society 164, 855–868. https://doi.org/doi.org/10.1144/0016-76492006-131
Schenk, O., Peters, K., Burnham, A., 2017. Evaluation of alternatives to Easy% Ro for calibration of basin and petroleum system models, in: 79th EAGE Conference and Exhibition 2017. EAGE, pp. 1–5. https://doi.org/10.3997/2214-4609.201700614
Schön, J.H., 2015. Physical properties of rocks: Fundamentals and principles of petrophysics. Elsevier.
Schön, J.H., 2011. Physical properties of rocks-a workbook. Handbook of Petroleum Exploration and Production.
Schumacher, S., Moeck, I., 2020. A new method for correcting temperature log profiles in low-enthalpy plays. Geothermal Energy 8, 27. https://doi.org/10.1186/s40517-020-00181-w
Sclater, G.J., Christie, P., 1980. Continental stretching: An explanation of the Post-Mid-Cretaceous Subsidence of the Central North Sea Basin, Journal of Geophysical Research. https://doi.org/10.1029/JB085iB07p03711
Seipold, U., Schilling, F.R., 2003. Heat transport in serpentinites. Tectonophysics 370, 147–162. https://doi.org/10.1016/S0040-1951(03)00183-5
Sekiguchi, K., 1984. A method for determining terrestrial heat flow in oil basinal areas. Tectonophysics 103, 67–79. https://doi.org/10.1016/0040-1951(84)90075-1

Sheplev, S. V., Reverdatto, V., 1998. A Contribution to the Further Investigation of McKenzie's Rifting Model, Geophysica.
Siegert, M.J., Marsiat, I., 2001. Numerical reconstructions of LGM climate across the Eurasian Arctic. Quaternary Science Reviews 20, 1595–1605.
Skogseid, J., Planke, S., Faleide, J.I., Pedersen, T., Eldholm, O., Neverdal, F., 2000. NE Atlantic continental rifting and volcanic margin formation. Geological Society, London, Special Publications 167, 295–326.
Somerton, W.H., 1992. Thermal properties and temperature-related behavior of rock/fluid systems. Elsevier.
Steckler, M.S., 1985. Uplift and extension at the Gulf of Suez: indications of induced mantle convection. Nature 317, 135–139. https://doi.org/10.1038/317135a0
Steckler, M.S., Watts, A.B., 1978. Subsidence of the Atlantic-type continental margin of New York. Earth and planetary science letters 41, 1–13.
Stein, C.A., Cloetingh, S., Wortel, R., 1989. Seasat-derived gravity constraints on stress and deformation in the northeastern Indian Ocean. Geophysical Research Letters 16, 823–826. https://doi.org/10.1029/GL016i008p00823
Stoupakova, A., Sokolov, A., Soboleva, E., Kiryukhina, T.A., Kurasov, I.A., Bordyug, E., 2015. Geological survey and petroleum potential of Paleozoic deposits in the Western Siberia. GEORESURSY 61, 63–76. https://doi.org/10.18599/grs.61.2.6
Sweeney, J.J., Burnham, A.K., 1990. Evaluation of a simple model of vitrinite reflectance based on chemical kinetics. AAPG bulletin 74, 1559–1570. https://doi.org/10.1306/0C9B251F-1710-11D7-8645000102C1865D
Talwani, M., 1998. Errors in the total Bouguer reduction. GEOPHYSICS 63, 1125–1130. https://doi.org/10.1190/1.1444412
Theissen, S., Iyer, K., Rüpke, L.H., Phipps Morgan, J., 2010. Coupled mechanical and hydrothermal modelling of crustal accretion at fast spreading ridges, in: EGU General Assembly Conference Abstracts. p. 10890.
Theissen, S., Rüpke, L.H., 2010. Feedbacks of sedimentation on crustal heat flow: New insights from the Voring Basin, Norwegian Sea. Basin Research 22, 976–990. https://doi.org/10.1111/j.1365-2117.2009.00437.x
Thomsen, R.O., 1998. Aspects of applied basin modelling: sensitivity analysis and scientific risk. Geological Society, London, Special Publications 141, 209–221.
Tikhonov, I.N., Lomtev, V.L., 2015. Shallow seismicity of the Sea of Okhotsk and its probable tectonic nature. Seismic Instruments 51, 111–128.
Tissot, B.P., Welte, D.H., 1984. Petroleum formation and occurrence, Second Rev. ed. Springer-Verlag Berlin Heidelber.
Ulmishek, G.F., 2003. Petroleum geology and resources of the West Siberian Basin, Russia. US Department of the Interior, US Geological Survey Reston, Virginia.
Vadakkepuliyambatta, S., Bünz, S., Mienert, J., Chand, S., 2013. Distribution of subsurface fluid-flow systems in the SW Barents Sea. Marine and Petroleum Geology 43, 208–221. https://doi.org/10.1016/j.marpetgeo.2013.02.007
Veeken, P.C.H., Titov, K. V, 1996. Gravity modelling along a seismic line across the Mandawa basin, southeastern Tanzania. Journal of African Earth Sciences 22, 207–217.
Veevers, J.J., 1981. Morphotectonics of rifted continental margins in embryo (East Africa), youth (Africa-Arabia), and maturity (Australia). The Journal of Geology 89, 57–82.
Vening Meinesz, F., 1941. Gravity over the Hawaiian archipelago and over the Madiera area: conclusions about the Earth's crust. Proc, Kort. Ned. Akad. Wetensch.

Verzhbitsky, E. V, Berlin, Y.M., Kononov, M. V, Marina, M.M., 2006. Estimates of the Temperatures of Hydrocarbon Generation in the Region of the Sea of Okhotsk. Oceanology 46, 534–544.
Vierbuchen, R., George, R., Vail, P., 1982. A thermo-mechanical model of rifting with implications for outer high on passive continental margins, Am. Assoc. Pet. Geol. Bull.
Vladimirov, A., 2020. Improving the reliability of basin and petroleum system modelling by reducing uncertainties in geothermal characteristics. Master Thesis, Skoltech, Moscow, Russia.
Vogt, C., Mottaghy, D., Wolf, A., Rath, V., Pechnig, R., Clauser, C., 2010. Reducing temperature uncertainties by stochastic geothermal reservoir modelling. Geophysical Journal International 181, 321–333.
von Terzaghi, K., 1923. Die Berechnug der Durchlassigkeit des Tones aus dem Verlauf der hydromechanischen Spannungserscheinungen. Sitzungsber. Akad. Wiss.(Wien). Math.-Naturwiss. Kl., Abt. Iia 132, 125–138.
Vtorushina, E.A., Bulatov, T.D., Kozlov, I.V., Vtorushin, M.N., 2018. The advanced technique for determination of pyrolysis parameters of rocks. Oil and gas geology 2, 71–77. https://doi.org/10.31087/0016-7894-2018-2-71-77
Vyssotski, A. V, Vyssotski, V.N., Nezhdanov, A.A., 2006. Evolution of the West Siberian basin. Marine and Petroleum Geology 23, 93–126. https://doi.org/10.1016/j.marpetgeo.2005.03.002
Wangen, M., 2010. Physical principles of sedimentary basin analysis. Cambridge University Press.
Wangen, M., 1995. The blanketing effect in sedimentary basins. Basin Research 7, 283–298. https://doi.org/10.1111/j.1365-2117.1995.tb00118.x
Waples, D.W., 2001. A New Model for Heat Flow in Extensional Basins: Radiogenic Heat, Asthenospheric Heat, and the McKenzie Model. Natural Resources Research 10(3), 227–238. https://doi.org/10.1023/A:1012521309181
Waples, D.W., 1998. Basin modelling: how well have we done? Geological Society, London, Special Publications 141, 1–14. https://doi.org/10.1144/GSL.SP.1998.141.01.01
Waples, D.W., Ramly, M., 2001. A statistical method for correcting log-derived temperatures. Petroleum Geoscience 7, 231–240. https://doi.org/10.1144/petgeo.7.3.231
Watts, A.B., 2011. Isostasy, in: Gupta, H.K. (Ed.), Encyclopedia of Solid Earth Geophysics. Springer Netherlands, Dordrecht, pp. 647–662. https://doi.org/10.1007/978-90-481-8702-7_81
Watts, A.B., 2001. Isostasy and Flexure of the Lithosphere. Cambridge University Press.
Watts, A.B., Karner, G., Steckler, M.S., 1982. Lithospheric flexure and the evolution of sedimentary basins. Philosophical Transactions of the Royal Society of London. Series A, Mathematical and Physical Sciences 305, 249–281.
Watts, A.B., Ryan, W.B.F., 1976. Flexure of the lithosphere and continental margin basins, in: Developments in Geotectonics. Elsevier, pp. 25–44.
Watts, A.B., Torné, M., 1992. Crustal structure and the mechanical properties of extended continental lithosphere in the Valencia trough (western Mediterranean). Journal of the Geological Society 149, 813–827.
Webb, S.J., Nguuri, T.K., Gore, J., James, D.E., 2001. Gravity modeling of the Moho discontinuity and velocity perturbations of the upper most mantle., in: 7th SAGA Biennial Technical Meeting and Exhibition. EAGE, p. cp-143-00075.

https://doi.org/10.3997/2214-4609-pdb.143.19.1
Wernicke, B., 1985. Uniform-sense normal simple shear of the continental lithosphere. Canadian Journal of Earth Sciences 22, 108–125.
White, N., 1993. Recovery of strain rate variation from inversion of subsidence data. Nature 366, 449.
White, N., McKenzie, D., 1988. Formation of the 'Steer's Head' Geometry of Sedimentary Basins by Differential Stretching of the Crust and Mantle, Geology. https://doi.org/10.1130/0091-7613(1988)016<0250:FOTSSH>2.3.CO;2
Wilson, J.T., 1965. A new class of faults and their bearing on continental drift. Nature 207, 343–347.
Wust, R.A.J., Nassichuk, B.R., Brezovski, R., Hackley, P.C., Willment, N., 2013. Vitrinite reflectance versus pyrolysis Tmax data: Assessing thermal maturity in shale plays with special reference to the Duvernay shale play of the Western Canadian Sedimentary Basin, Alberta, Canada, in: SPE Unconventional Resources Conference and Exhibition-Asia Pacific. Society of Petroleum Engineers. https://doi.org/10.2118/167031-MS
Wygrala, B., 1989. Integrated study of an oil field in the southern Po basin, northern Italy. Publikationen vor 2000.
Yang, S., Horsfield, B., 2020. Critical review of the uncertainty of Tmax in revealing the thermal maturity of organic matter in sedimentary rocks. International Journal of Coal Geology 1–12. https://doi.org/10.1016/j.coal.2020.103500
Ziegler, P.A., 1994a. Geodynamic Processes Governing Development of Reifted Basins. Verlag nicht ermittelbar.
Ziegler, P.A., 1994b. Hydrocarbon habitat in rifted basins. Verlag nicht ermittelbar.
Ziegler, P.A., Cloetingh, S., 2004. Dynamic processes controlling evolution of rifted basins. Earth-Science Reviews 64, 1–50.